NASA Technical Memorandum 89426

Boundary-Layer and Wake Measurements on a Swept, Circulation-Control Wing

Frank W. Spaid and Earl R. Keener

December 1987

National Aeronautics and
Space Administration

NASA Technical Memorandum 89426

Boundary-Layer and Wake Measurements on a Swept, Circulation-Control Wing

Frank W. Spaid, McDonnell Douglas Research Laboratories, St. Louis, Missouri
Earl R. Keener, Ames Research Center, Moffett Field, California

December 1987

National Aeronautics and
Space Administration

Ames Research Center
Moffett Field, California 94035

BOUNDARY-LAYER AND WAKE MEASUREMENTS ON A SWEPT, CIRCULATION-CONTROL WING*

Frank W. Spaid
McDonnell Douglas Research Laboratories
FTS 8-314-233-2509

Earl R. Keener
NASA Ames Research Center

SUMMARY

Wind-tunnel measurements of boundary-layer and wake velocity profiles, surface static-pressure distributions, and oil-flow photographs are presented for a swept, circulation-control wing. The model is an aspect-ratio-four semispan wing mounted on the tunnel side wall at a sweep angle of 45°. The 25.4-cm constant-chord airfoil is a 20% ellipse, modified with circular leading and trailing edges of 4% radius. This configuration does not represent a specific shape obtained from current vehicle design concepts, which are being developed. A full-span, tangential, rearward-blowing, circulation-control slot is located ahead of the trailing edge on the upper surface. Flow surveys were obtained at mid-semispan at free-stream Mach numbers of 0.425 and 0.70, Reynolds numbers of 2.3×10^6 and 3.2×10^6, based on streamwise chord, angles of attack of 0° and 5°, and jet stagnation to free-stream static-pressure ratios of 1.0 to 2.2.

*This research was conducted under the McDonnell Douglas Independent Research and Development Program in cooperation with the NASA Ames Research Center.

Boundary-layer velocity profiles measured on the forward portions of the wing's upper and lower surfaces are approximately streamwise. The flow in the vicinity of the jet exit and in the near wake is highly three-dimensional. The jet flow near the slot on the Coanda surface is directed normal to the slot, or 45° inboard. All near-wake surveys show large outboard flows at the center of the wake. At Mach 0.425 and a 5° angle of attack, a range of jet blowing rates was found for which an abrupt transition from incipient separation to attached flow occurs in the boundary layer upstream of the slot. The variation in the lower-surface separation location with blowing rate was determined from boundary-layer, Preston-tube, and obstacle-block measurements. The influence of blowing on the size of the lower-surface separated region was shown to be much more pronounced at $M_\infty = 0.425$ than at $M_\infty = 0.70$.

NOMENCLATURE

$b/2$ semispan

c streamwise wing chord

c_ℓ section lift coefficient

C_f local skin-friction coefficient, τ_w/q_e

C_p pressure coefficient, $(p-p_\infty)/q_\infty$

C_μ jet momentum coefficient, $m_j V_j/q_\infty S$

d static-pressure orifice diameter

h obstacle block height

m_j jet mass-flow rate

M Mach number

p pressure

q dynamic pressure, $(1/2)\rho u^2$

Re_c Reynolds number based on chord

S wing area, defined as the product of the slot length and the wing chord measured normal to the section generators

u velocity magnitude

u_s component of velocity parallel to flow direction at edge of boundary layer

u_τ shear velocity, $\sqrt{\tau_w/\rho_w}$

V_j computed jet velocity assuming isentropic expansion from jet stagnation pressure to p_∞

x coordinate measured parallel to free-stream direction

y spanwise coordinate

z coordinate normal to wing plane

z^+ law-of-the-wall coordinate, $(zu_\tau)/\nu_w$

α wing angle of attack

β yaw-plane flow direction angle, positive outboard

δ_1^* streamwise displacement thickness, $\int_0^\delta \left(1 - \frac{\rho u_s}{\rho_e u_e}\right) dz$

ν kinematic viscosity

ρ density

σ pitch-plane flow direction angle, positive upward

τ_w wall shear stress

Subscripts

e	conditions at edge of boundary layer
j	jet parameter
w	conditions at surface
∞	free-stream conditions

INTRODUCTION

There are several ways to control the aerodynamic circulation of wings and thus, the amount of lift. One type of circulation control that is currently under investigation is tangential blowing from a slot located ahead of a rounded trailing edge. The tendency of the flow to adhere to the trailing-edge surface is known as the Coanda effect. The deflected flow can increase the lift of a wing section to several times that obtained by the conventional method of increasing the angle of attack. Wood and Nielsen (ref. 1) present a summary of circulation-control research.

A cooperative investigation of the boundary layer and wake of a swept, circulation-control wing was recently conducted by NASA Ames Research Center and McDonnell Douglas Research Laboratories in the Ames Six- by Six-Foot Transonic Wind Tunnel. The test was conducted in support of the NASA X-Wing stopped-rotor research vehicle, which is designed to cruise at high speed with the rotor stopped in the X-wing configuration (ref. 1). The model is an aspect-ratio-four semispan wing mounted on the side wall. The 25.4-cm constant-chord airfoil is a 20% ellipse, modified with circular leading and trailing edges. This generic configuration does not represent a specific shape from current vehicle design concepts which are being developed. A full-span, tangential, rearward-blowing circulation-control slot is located ahead of the trailing edge on the upper surface. The wing was tested at Mach numbers from 0.3 to 0.75 at sweep angles of 0° and 45° with internal-to-external pressure ratios of 1.0 to 3.0. Lift and pitching-moment coefficients were obtained from measured pressure distributions. Surface-flow patterns were photographed by use of the oil-streak flow-visualization method.

This report presents the results of the boundary-layer and wake measurements at Mach numbers of 0.425 and 0.70 at 45° sweep angle. The pressure measurements and oil-flow photographs are presented by Keener et al. (ref. 2).

TEST FACILITY

The Ames Six- by Six-Foot Transonic/Supersonic Wind Tunnel was chosen because the allowable model size and the tunnel operational characteristics

are suitable for boundary-layer research. The tunnel is a variable-pressure, continuous-flow facility. The nozzle leading to the test section is of the asymmetric sliding-block type that permits a continuous variation of Mach number from 0.25 to 2.3. The test section has a slotted floor and ceiling with 6% porosity and provisions for boundary-layer removal. The turbulence level is measured to be about 1.5% rms of the free-stream velocity.

MODEL

Details of the model design are given by Keener et al. (ref. 2). The model is a semispan wing incorporating circulation control by tangential blowing from a spanwise slot located ahead of a rounded trailing edge. The model was mounted on the side wall of the tunnel on a turntable that could be manually rotated through a ±5° range in angle of attack. The wing-root mounting structure is covered by a fairing. Figure 1 shows the model installation in the tunnel showing the zero- and 45° sweep positions; the resulting aspect ratios are 4.0 and 1.85, respectively, based on the normal component of the exposed span. Figure 1 also shows the position of the boundary-layer traversing unit, which was mounted on a bracket attached to the tunnel center-body support. Figure 2 shows views of the model in the 45° sweep position and the boundary-layer traversing unit.

The wing has a 20% elliptical section and a 25.4-cm constant chord, modified with circular leading and trailing edges of 4% radius (fig. 3). A full-span, tangential, rearward-blowing, circulation-control slot, with a nominal slot height of 0.0020 chord and a trailing-edge thickness of 0.0008 chord, was incorporated ahead of the trailing edge on the upper surface.

Design suggestions based on experience with previous circulation-control tests were contributed by N. Wood, Stanford Institute for Aeronautics and Aeroacoustics, and by E. Rogers and J. Abramson, David W. Taylor Naval Ship Research and Development Center. Publications from their research are discussed in the review paper by Wood and Nielsen (ref. 1). The model design closely follows the design concepts of Wood and Conlon (ref. 3), and Wood and Sanderfer (ref. 4).

The model was designed in four parts (fig. 3), split along the plane of symmetry. The center of the model contains an internal plenum, which was connected to the external air supply at the wing root through the side wall of the tunnel. A separate compartment is located forward of the plenum to pass the pressure tubes from the model through the wing root. This compartment is sealed from the plenum by an O-ring seal. O-ring seals are also used between the forward parts and the slot and trailing-edge pieces, installed in a horizontal step so that a positive seal occurs when the top and bottom halves are bolted together. Several vertical posts, spaced every 7.11 cm spanwise, separate the split halves. A means for adjusting the slot height is provided by adjusting screws and set screws at several span stations. The design of the trailing-edge Coanda surface and slot is described by Keener et al. (ref. 2). The model was constructed from stainless steel and designed to withstand an internal pressure of 410 kPa.

The air supply was provided from the tunnel 550-kPa dry-air sphere. The air flow was controlled by a regulator to set the total pressure in the wing plenum.

INSTRUMENTATION AND DATA REDUCTION

Wing Surface Data, Jet Properties, and Test-Section Conditions

Details of the pressure instrumentation are given by Keener et al. (ref. 2). The pressure instrumentation consisted of 252 orifices on the wing, installed at five spanwise stations (rows 1 to 5: $2y/b$ = 0.1, 0.3, 0.5, 0.7, and 0.9, based on the exposed span at zero sweep) and one row of orifices at the midspan of the wing-root fairing (fig. 4a). More orifices were placed at row 4, $2y/b$ = 0.7, especially over the trailing edge, to obtain more detail at one row. Additional orifices were placed at row 6 at a 45° angle between rows 3 and 4 ($2y/b$ = 0.5 and 0.7) to assist in the analysis of the pressures at a sweep angle of 45° and to provide a row of orifices near the location of the upper-surface boundary-layer measurements.

The surface static pressures were measured with electronically actuated pressure-scanning valves containing pressure transducers that were connected

to an automatic data-recording system. The self-calibrating feature of the scanning valves provided an accuracy of about 0.25% of full scale of the ±86.2-kPa transducers, providing an accuracy in pressure coefficient of approximately ±0.01. Tunnel test conditions were measured with precision pressure transducers, resulting in a Mach number accuracy of about ±0.002. Tunnel static pressure was measured on the tunnel wall 10 wing-chord lengths ahead of the wing-root leading edge. Angle of attack was set manually by rotating the wall turntable and setting the angle with an inclinometer with an accuracy of ±0.03°.

Static-pressure measurements were reduced to standard pressure coefficients by use of the tunnel conditions which were measured at the beginning of each data set. The data were recorded, processed, and plotted by the tunnel data-acquisition system. Pressure coefficients for each spanwise station were numerically integrated by the trapezoidal rule to determine wing-section normal-force and pitching-moment coefficients. Wing-panel normal-force, pitching-moment, and bending-moment coefficients were determined by Simpson's-rule numerical integration of the span-load distributions. Jet total mass flow was determined from a calibrated orifice plate mounted in the air supply line. The jet velocity was calculated using the free-stream static pressure as the jet-exhaust pressure.

Figures 4b and c show obstacle blocks and Preston tubes, respectively, which were cemented to the wing during four runs at pressure orifice rows 3 and 4 on both upper and lower surfaces. These devices were installed such that the end of the Preston tube or the face of the obstacle block having the cylindrical cut-out was normal to the streamwise direction. The difference between the undisturbed static pressure and the pressure measured by the Preston tube or the pressure measured in the presence of the obstacle block is related to the local skin friction through a calibration. The Preston-tube data were reduced by use of the calibration of Patel (ref. 5) in the tabulated form presented by Head and Vasanta Ram (ref. 6). The obstacle-block data were reduced by use of the calibration of Nituch (ref. 7).

Boundary-Layer and Wake Measurements

The following discussion of the boundary-layer and wake measurements includes a description of the experimental apparatus, estimates of uncertainty related both to individual probe pressure measurements and to probe calibration data, and estimates of the resulting uncertainties in velocity and flow angle data.

Traversing Unit and Probes

The traversing unit shown in figures 1 and 2 contains stepper motors that allow remote movement of the probe tip in the streamwise and vertical directions; the probe location is determined with the aid of encoders. Streamwise position resolution is 0.087 mm per encoder pulse, and vertical resolution is 0.0052 mm per encoder pulse. A microcomputer-based probe control system allows manual operation of the unit and also provides an automatic mode in which data are obtained in a preprogrammed sequence of probe movements and data-acquisition cycles. The wing surface was located by electrical contact between the wing and the probe tip at the beginning of a boundary-layer survey. It was necessary to locate the wing surface with the probe while the tunnel was running to minimize errors caused by aerodynamically induced deflections of the model and the traversing unit. The measurement of distance from a survey point to the wing surface was limited in accuracy by tunnel-induced vibration. The uncertainty in the distance of a probe tip from the wing surface is estimated to be 0.15 mm, based on both the vertical travel noted between the first indication by the fouling circuit and the point at which continuous contact was established, and on apparent vertical shifts between repeated surveys of the same boundary-layer profile.

The probe tips used for most boundary-layer surveys are small, flattened, three-hole probes; the wake surveys and some wall-jet surveys (flow-field surveys above the Coanda surface) were made with a small five-hole probe. The probes are shown in figure 5. Two types of three-hole probes were used. Most of the three-hole probe surveys were obtained with probes which were straight when viewed from above; a limited number of surveys above the Coanda surface were obtained with a probe having a yawed tip. The tip of the latter

probe was inclined outboard 30° to more nearly align the tip of this probe with the flow in the jet. The tip of the five-hole probe was inclined upward 15° to reduce its flow interference in the wake downwash. To reduce flow interference and minimize errors in measurement of flow angle and stagnation pressure, the three-hole probes were adjusted in pitch angle so that the tips were nearly parallel to the wing surface. The probes are similar to those described by Dudzinski and Krause (ref. 8).

Probe-Pressure-Measurement Uncertainty

A pressure transducer was connected to each probe orifice through a fluid switch. Data for a two-point calibration of each transducer were obtained by cycling the switch at the beginning and end of each boundary-layer survey. The uncertainty in measurement of pressure at individual probe ports was estimated in the following manner: An individual probe-port pressure measurement, p_m, is determined from the relation

$$p_m = p_r + (e_m - e_0)\left(\frac{p_c - p_r}{e_c - e_0}\right) \tag{1}$$

where p_r is the reference pressure, p_c is the calibration pressure applied to the transducer at the beginning and end of each survey, e_m is the transducer output signal corresponding to p_m, e_0 is the transducer output signal corresponding to zero pressure differential, and e_c is the transducer output signal corresponding to the pressure differential $p_c - p_r$. An estimate of the contributions of uncertainties in each of the right-side quantities to p_m can be obtained by first determining the differential dp_m,

$$dp_m = \sum_i \frac{\partial p_m}{\partial x_i}\, dx_i \tag{2}$$

where the x_i's represent the quantities on the right side of the previous expression, approximating the partial derivatives by their maximum values, and replacing the differentials by finite increments. These manipulations lead to the conclusion that perturbations in p_c and p_r produce equal perturbations in p_m, and perturbations in e_m, e_c, and e_0 do the same, except that the voltage

perturbations must be converted to pressure by multiplying by the transducer sensitivity.

The final procedure used to estimate uncertainty in the probe pressure measurements employed the previous analysis as a guide, but the individual uncertainty estimates were combined in a root-sum-square (RSS) fashion, and additional sources of uncertainty were included. This procedure is summarized in table 1. Values of p_c and p_r were determined by precision absolute-pressure transducers which were maintained in a temperature-controlled environment. The uncertainties in these measurements were determined from the transducer specifications. The resolution of the microcomputer in recording the amplified transducer output signal is 2.5 mV. The uncertainties assigned to e_0 and e_c correspond to twice this minimum resolution, converted to pressure by use of the transducer sensitivity. The uncertainty assigned to e_m corresponds to a combination of this minimum resolution, plus a typical observed variation in e_m during a run, resulting from flow unsteadiness. The entry labeled "transducer cal." is the nonlinearity and hysteresis error of the transducers, obtained from the transducer calibrations, when the transducers are operated over the pressure differential range of the present experiments, approximately 35 kPa. The RSS combination of these first six entries in table 1 is 0.17 kPa, approximately 1.5% and 0.7% of free-stream dynamic pressure at Mach 0.425 and 0.70, respectively.

Probe Calibration

Probe calibrations were performed in a free-jet calibration facility, following the procedures outlined by Dudzinski and Krause (ref. 8). Probe-angle-measurement accuracy was ±0.1°. Calibrations were performed at six Mach numbers, ranging from 0.25 to 1.0. Three-hole-probe calibrations were performed over an angle range of ±40° in the yaw plane, and five-hole-probe calibrations were performed over a range of ±40° in the pitch plane and +60° to -40° in the yaw plane, relative to the probe tip. The probe pressures were combined into the calibration parameters listed in table 2. For the three-hole probe data, the angle in the yaw plane and the normalized stagnation pressure correction were tabulated as functions of the the normalized yaw-plane pressure difference. These functions were observed to be independent of

calibration Mach number, within the limits of accuracy of the calibration measurements. In the case of the five-hole probe data, the yaw- and pitch-plane angles and the normalized static- and stagnation-pressure corrections were tabulated as functions of the yaw- and pitch-plane pressure differences for each of the calibration Mach numbers. The pitch- and yaw-plane angles, σ and β, are linear functions of the corresponding pressure differences and are nearly independent of the out-of-plane pressure difference and the Mach number, in the central portion of the calibration angle range ($\pm 20°$ in the pitch and yaw planes). The stagnation-pressure correction, a dome-shaped surface in these coordinates, is also nearly independent of Mach number in the central portion of the calibration map. The static-pressure correction is also a dome-shaped surface in these coordinates, but it has a systematic variation with Mach number. At the larger values of σ and β, all of the calibration characteristics become increasingly nonlinear and Mach-number dependent. These features of the five-hole-probe calibration data were treated in the data-reduction program by a three-dimensional, linear interpolation procedure in which the local Mach number was included as an independent variable.

Modified forms of the three- and five-hole-probe calibration parameters were used for those runs in which data from one of the probe ports were found to be unreliable (see column 3 in table 2). Use of these modified parameters resulted in only a modest decrease in the accuracy of the five-hole-probe data. In the case of the three-hole-probe data, it was necessary to use the local static pressure determined from the wing surface-pressure distribution, in addition to the remaining two probe-port measurements, to determine β and the stagnation-pressure correction. The additional uncertainty in these latter quantities results primarily from the disturbance to the local static-pressure distribution caused by the presence of the probe. The effect of this additional uncertainty on the measured value of β is substantially greater than the corresponding effect on the determination of local Mach number or velocity, since the stagnation pressure can be regarded as a zero-order quantity, and β and the stagnation-pressure correction are first-order quantities with comparable uncertainties.

Errors in determining quantities from the probe calibration data arise from both the wind tunnel measurement errors and the errors associated with

the calibration data. The probe-pressure measurement errors associated with the calibration data were estimated by including an equivalent additional source of error in the wind tunnel measurements.

Uncertainty estimates for the calibration data were obtained by first estimating the uncertainties in measurements of pressure at the individual probe ports in the previously described manner. Atmospheric pressure was measured by a precision absolute-pressure transducer with a quoted uncertainty of 0.02 kPa. Probe pressures and calibrator stagnation pressure were measured with differential pressure transducers referenced to atmospheric pressure. Zeros were recorded for these transducers at the beginning and end of each series of probe calibration measurements, and the average zeros were used in reducing the data. The maximum error from this source is thus one-half the zero shift. The zero shift used in the uncertainty estimate was the maximum observed in all of the calibration runs, 0.103 and 0.059 kPa, corresponding to the probe transducers and the stagnation-pressure transducer, respectively. Nonlinearity and hysteresis errors for the probe transducers were determined as a function of pressure range corresponding to each calibration Mach number. The maximum error for the particular range of differential pressure observed in the calibration records of any of the nine transducers used in this study (probe transducers and spares) was used as the estimate of the nonlinearity/ hysteresis error. Estimated errors from this source ranged from 0.021 to 0.084 kPa for calibration Mach numbers of 0.25 to 1.0. Corresponding data were not available for the stagnation-pressure transducer, so the nonlinearity and hysteresis estimates corresponding to the probe transducers were used to represent the stagnation-pressure transducer. Since the stagnation-pressure transducer is a more accurate instrument, this approximation should be conservative. The overall pressure-measurement error influencing the calibration data was computed as an RSS combination of the errors arising from the stagnation-, static-, and probe-pressure measurements.

Since the calibrator was operated at constant static pressure, and the tunnel conditions correspond approximately to constant free-stream stagnation pressure, it was necessary to correct the estimates for probe-calibration pressure-measurement errors for variations in local dynamic pressure. This was done by noting that the low-Mach-number measurements in the tunnel,

$M \leq 0.4$, were made primarily in viscous regions where the local static pressure is approximately equal the free-stream value, and that the higher local-Mach-number measurements in the tunnel, $M > 0.4$, were made primarily in inviscid regions where the local stagnation pressure is equal to the free-stream value. The corrected uncertainties corresponding to the probe calibration data are shown in table 1; the largest uncertainties are associated with the lowest calibration Mach number, and are slightly less than the uncertainties in the wind tunnel probe-pressure measurements.

Probe readings corresponding to the free-stream flow direction were determined in the wind tunnel by taking probe data at a position approximately 0.7 m above the wing, with the wing at 0° angle of attack, and a low jet-blowing rate, to stabilize the wing wake.

Velocity and Flow Angle Uncertainty Estimates

Uncertainties in σ, β, and local velocity or Mach number determined from the probe data are strongly influenced by the values of σ and β and the local dynamic pressure. As a result, it is not possible to quote meaningful single numerical values for the uncertainties in the measured values of these quantities. Instead, reduced data were first computed from the measured probe pressures. Each probe pressure was, in turn, incremented by the value of the estimated uncertainty, and the resulting perturbed dependent quantities were determined from the calibration data. Perturbations in the dependent quantities were obtained by subtracting the perturbed dependent quantities from the nominal values, and an estimate of uncertainty in the nominal quantity was obtained by RSS combination of the computed perturbations. A value of 0.24 kPa was used as the estimated overall uncertainty for the probe-pressure measurements, including the contribution of the calibration uncertainty. This value lies between the sum and the RSS combination of the contributions of the wind tunnel pressure-measurement uncertainty and the uncertainty attributed to the calibration data, and is believed to be slightly conservative. The uncertainty in local static pressure used in the analysis of the three-hole-probe data was assumed to be $\Delta C_p = 0.1$ on the upper surface of the wing and $\Delta C_p = 0.05$ on the lower surface, based on examination of data from the present study

and on data reported by Spaid et al. (ref. 9) for airfoil boundary-layer measurements. These increments in C_p are actually estimates of C_p variations associated with probe interference. Values of uncertainty estimates for β and Mach number for the three-hole-probe data and uncertainty estimates for σ, β, Mach number, and C_p for the five-hole-probe data are included in the tabulated data (see Appendix).

The tabulated data show that under favorable conditions, i.e., relatively high local dynamic pressure and moderate flow angularity relative to the probe tip, the uncertainties in flow angles determined by the five-hole probe are approximately 0.5°, and the Mach number uncertainty is of the order of 1%. At larger flow-deflection angles and low dynamic pressures characteristic of the inner region of a boundary layer near separation, or at the center of a near wake, the uncertainty is considerably greater. Flow-angle data for which the uncertainty estimate exceeds 10° have been discarded. The estimates of uncertainty in local Mach number for the three-hole-probe data are dominated by the estimated uncertainty in C_p, which is also primarily responsible for the increased values of uncertainty in both β and Mach number for those surveys with the three-hole probe in which the data from one port could not be used. These surveys include the majority of the boundary-layer profiles obtained at the forward chordwise stations on the wing; fortunately, the flow at these forward stations is predominantly streamwise, and the associated measurement uncertainties are moderate.

Another source of error in the the three-hole probe data is flow misalignment in the pitch plane. This error is believed to arise partly from misalignment of the probe tip with the local surface, since the probe tip was not realigned with the surface of the wing at each chordwise station, but was aligned at one station and then traversed streamwise in the vicinity of that station. However, the major contribution to this source of error appears to have been streamline deflection associated with entrainment by the jet at high blowing rates. Surveys for which the stagnation pressure indicated by the probe at the edge of the viscous region differed from the free-stream value by more than 1.5% were discarded, as were several of the yaw-plane angle profiles for which significant pitch-plane misalignment effects were indicated.

TEST CONDITIONS AND PROCEDURES

The wing pressures were first measured without boundary-layer trips at $M_\infty = 0.70$ at zero sweep. Next, boundary-layer trips were installed on the wing by use of sifted glass spherules at 9% chord. Sublimation flow-visualization tests were made at a Mach number of 0.70 to verify that the estimated trip size of 0.23-mm diam was adequate to cause transition. When the wing was swept to 45°, a sublimation test verified that the trips were also effective at this angle.

Flow surveys were obtained at free-stream Mach numbers, M_∞, of 0.425 and 0.70, Reynolds numbers based on streamwise chord, Re_c, of 2.3×10^6 and 3.2×10^6, angles of attack, α, of 0° and 5°, and ratios of jet stagnation to free-stream static pressure, p_j/p_∞, of 1.0 to 2.2. The Mach numbers 0.425 and 0.70 correspond to the Mach numbers 0.30 and 0.50 at zero sweep, determined from simple sweep theory, $M_\infty/\cos 45°$. Performance data corresponding to both the swept and unswept conditions are presented by Keener et al. (ref. 2). Boundary-layer surveys were made at one span station, starting at about 20% chord at static-pressure orifice row 3, back to near the trailing edge outboard of row 4, on both upper and lower surfaces (fig. 4). Wake surveys were obtained in a region 1% to 30% chord downstream of the trailing edge.

Oil-flow-visualization tests were made at both sweep angles at several Mach numbers to assist the analysis of the pressure and boundary-layer measurements (ref. 2).

RESULTS AND DISCUSSION

Plotted data from this investigation are divided into three major categories: static-pressure data related to the boundary-layer and wake surveys, vector and scalar boundary-layer and wake plots accompanied by selected oil-flow photographs, and displacement-thickness and skin-friction data. Tabulated data are presented on microfiche, located in a pocket inside the back cover of this report. A guide to the tabulated data is presented in the Appendix.

Static-Pressure Data

The static-pressure data pertaining to the flow surveys include chordwise surface static-pressure distributions obtained near mid-semispan, local static-pressure distributions illustrating probe-tip interference effects, detailed surface static-pressure distributions in the vicinity of the slot, and static-pressure profiles obtained from five-hole-probe surveys above the Coanda surface.

Static-Pressure Distributions Near Mid-Semispan

Static-pressure distributions corresponding to test conditions for which probe data were obtained are shown in figure 6. The upper-surface data were obtained from the diagonal row of orifices located at the spanwise survey station, and the lower-surface data were interpolated to that station from the adjacent chordwise orifices. Blowing rates are indicated both by p_j/p_∞ , and by the momentum coefficient, C_μ, the jet momentum flux normalized by the free-stream dynamic pressure and the wing area. The corresponding section lift coefficient, c_ℓ, is also shown. The pressure distributions shown in figure 6a correspond to $M_\infty = 0.425$ and $\alpha = 0°$. The pressure distributions associated with the two values of blowing are characterized by weak suction peaks at the leading edge, near-zero pressure gradients at mid-chord, and large suction peaks on the upper surface downstream of the jet. The flow is locally supersonic in this region at the higher blowing rate; the minimum value of C_p is -4.75 (not shown).

Upper-surface pressure distributions corresponding to $M_\infty = 0.425$ and $\alpha = 5°$ are shown in figure 6b. The increased angle of attack increases the leading-edge suction peaks and suppresses the suction peaks on the Coanda surface.

Static pressure distributions corresponding to no blowing and three blowing rates at $M_\infty = 0.70$ and $\alpha = 0°$ are presented in figure 6c. The data correspond to approximately the same pressure-ratio range as those of figure 6a, but the values of C_μ and c_ℓ are smaller. Upper-surface data for $M_\infty = 0.70$ and $\alpha = 5°$ are shown in figure 6d.

The data presented in figures 6a and 6c corresponding to $\alpha = 0°$ were obtained prior to the installation of the probe traversing unit. Static-pressure data obtained at the same conditions with the traversing unit installed but with the probe fully retracted were found to agree with the data of figures 6a and 6c, essentially within the repeatability of the data. Increments in C_p ranged from 0 to 0.024 at $M_\infty = 0.425$ and from 0 to 0.01 at $M_\infty = 0.70$.

Probe Tip Interference

Representative examples of the disturbance to the surface static-pressure distributions caused by the presence of the probe tip in position for a survey are shown in figure 7, for $M_\infty = 0.425$ and $p_j/p_\infty = 1.4$(figs. 7a-c) and 1.8(figs. 7d-e). Several scans of the wing static-pressures were obtained during a boundary-layer survey, beginning with the probe tip in contact with the wing surface, and concluding with the probe slightly beyond the edge of the boundary layer. Multiple static-pressure distributions corresponding to the same probe chordwise location shown in figure 7 were obtained with the probe at various distances from the surface. The maximum disturbance to the local static-pressure associated with probe interference occurred with the probe in contact with the surface. Only the upper-surface static-pressure orifices were located sufficiently close to the probe survey stations to allow an evaluation of this effect. Nineteen cases were examined in detail, including the full range of test conditions and chordwise probe positions. In thirteen cases, the maximum increment in C_p at a surface orifice location caused by the probe at the survey station was less than 0.05, in five cases $0.05 \leq \Delta C_p \leq 0.08$, and in one case, the data shown in figure 7d, $\Delta C_p \approx 0.25$.

Static-Pressure Distributions Near the Slot

Figures 8 and 9 pertain to the static-pressure distributions in the vicinity of the slot ($x/c = 0.9665$). Figure 8 presents upper-surface static-pressure data for $0.9 \leq x/c \leq 1.0$ and $2y/b = 0.5$, 0.7, and 0.9. Regular spanwise variation is apparent in the surface static-pressure data at a fixed test condition, but the variations are less consistent on the Coanda surface, particularly at higher blowing rates. The filled symbols are data from the

five-hole probe, extrapolated to the surface, and the error bars associated with the filled symbols correspond to the uncertainties in the probe static-pressure data obtained from the previously described analysis. The computed uncertainty in C_p for these data ranges from 0.02 to 0.1. The computed uncertainty is assumed to be plus or minus, so the ranges of the error bars are shown as twice the magnitude of the uncertainty. No error bars are included where the computed uncertainty is of the same order as the plotting-symbol size. The partly filled symbols are C_p values used in reducing the three-hole-probe data obtained at that station. The large gradients near the slot at the higher blowing rates make the values of C_p at the slot somewhat uncertain. As indicated on the plots, the static pressure immediately upstream of the slot was extrapolated from the upstream data.

Static-Pressure Profiles from Five-Hole-Probe Surveys

Static-pressure distributions obtained from the five-hole-probe data above the Coanda surface are presented in figure 9. Data obtained with the probe immersed in the wall jet or in the shear layer above the jet have been omitted. Estimates of ΔC_p across the jet, based on a simple momentum balance, range from $\Delta C_p \approx 0.17$ at $M_\infty = 0.425$, $\alpha = 0°$, $p_j/p_\infty = 1.4$, to 0.06 at $M_\infty = 0.70$, $\alpha = 0°$, $p_j/p_\infty = 2.2$, and are consistent with extrapolations of the static-pressure profiles to the surface. The data corresponding to $M_\infty = 0.425$ and the higher blowing rates show vortex-like behavior, i.e., the C_p distributions seem consistent with a $1/z^2$ variation, but the profiles obtained at $M_\infty = 0.70$ show nearly constant static pressure above the Coanda surface. The profile obtained for $M_\infty = 0.425$, $\alpha = 0°$, and $p_j/p_\infty = 1.8$ was supersonic for $0 < z/c < 0.02$; the pressure coefficient in the supersonic region was assumed to vary linearly from the last subsonic point to a value of -3.97, estimated from the surface measurements.

Returning to figure 8, it can be seen that the five-hole-probe data at $\alpha = 0°$ at both Mach numbers are consistent with the surface static-pressure measurements. The surface static-pressure data and the probe data obtained at $\alpha = 5°$ at both Mach numbers show the same qualitative trend of increasingly negative pressure coefficients with increasing blowing rate; but there are increasing discrepancies between the two sources of data with increasing

blowing rate. The data obtained at $M_\infty = 0.70$ show less variation in C_p with blowing rate than the corresponding data for $M_\infty = 0.425$. Since the various uncertainty estimates are too small to explain these discrepancies, their cause is not known.

Boundary-Layer and Wake Surveys

Vector Plots at $M_\infty = 0.425$, $\alpha = 0°$

Figures 10 and 11 are composite views in the streamwise section plane of the aft portion of the model, including the slot inlet, and of the surrounding flow fields. This style of presentation is used in several of the subsequent figures to help clarify the qualitative features of these complex three-dimensional flows. The velocity vectors are projections in the streamwise plane, and the vector labeled u_∞ in the upper-left corner of both figures corresponds to the free-stream velocity. The boundary-layer profiles were obtained with a three-hole probe, and the vectors are drawn parallel to the local surface. The wake profiles and the wall-jet profile (the flow survey above the Coanda surface downstream of the jet exit station in figure 11) were obtained with a five-hole probe, and are drawn at the measured inclination angle.

The data of figure 10 correspond to $M_\infty = 0.425$, $\alpha = 0°$, and no blowing. No wake data were obtained at this test condition. The boundary-layer profiles show approximately symmetrical flow, as expected, with separation apparently occurring slightly downstream of the last measuring station ($x/c = 0.976$) on both the upper and lower surfaces.

Figure 11 is a composite view corresponding to $M_\infty = 0.425$, $\alpha = 0°$, and $p_j/p_\infty = 1.4$, the baseline test condition selected for flow-field surveys in this investigation. The characteristics of this flow field are in sharp contrast to the data corresponding to no blowing presented in the preceding figure. The boundary-layer profiles on the upper surface upstream of the slot and at the slot lip ($x/c = 0.967$) are full, showing the effect of entrainment by the jet. The jet is evident in the profile obtained at $x/c = 0.985$. A separated region is indicated by the lower-surface boundary-layer profiles.

Significant variations in pitch-plane inclination angles are present in the wake profiles; the gradients decrease with increasing x/c. The gap in the wake profile at x/c = 1.01 is a region where the flow direction exceeded the probe calibration range. The upper portion of the wake nearest the trailing edge is characterized by large negative values of the pitch-plane angle. Below the trailing edge, the pitch-plane angles are still negative, but are smaller in magnitude. Large cross-stream velocity components are present in this flow field; the cross-stream flow is shown in subsequent figures.

Close-ups of wall-jet and wake profiles corresponding to the baseline test condition are presented in figures 12-14. These data were obtained with the five-hole probe and are presented in the form of streamwise velocity components, cross-stream velocity components (velocity components lying in a plane normal to the free-stream velocity vector) and static-pressure distributions. The profiles of figures 12-14 correspond to x/c = 0.984, 1.02, and 1.10. The origin of the z-coordinate for the wake profiles is the upper lip of the slot. The streamwise profiles at x/c = 0.984 and 1.10 are also shown in figure 11. The velocity vectors are plotted to the same scale in figures 12-14, but differences in the mean value and range of variation in static pressure among the profiles required significant changes in the C_p scale.

The five-hole probe is too large to resolve the flow-field features accurately near the Coanda surface. In reducing the data shown in figure 12 corresponding to $0 \leq z/c \leq 0.0035$, the static pressure was extrapolated from the region above the jet to the surface, the stagnation pressure was assumed to be the maximum of the values measured by the probe orifices, and the pitch-plane flow direction was assumed to be parallel to the local surface.

The contrast between the inboard inclination of the entire profile at x/c = 0.984 and the outboard flow in the centers of the wake profiles is evident in these figures, as are the substantial variations in static pressure. The inboard inclination of the flow above the jet at x/c = 0.984 implies strong entrainment by the jet. As expected, the gradients decrease with increasing distance downstream.

The upper and lower portions of each wake profile include regions of constant stagnation pressure, indicating that the flow nonuniformities result from both inviscid and viscous effects. The upper edge of the wake near the trailing edge is characterized by high velocity, large downwash, and nearly streamwise flow in the yaw plane; the lower edge has lower velocity magnitudes and is more nearly streamwise in both planes. The flow in the central portion of the wake is predominantly outboard, despite the fact that the jet, which is strong enough to control the wing circulation, is directed 45° inboard. At $x/c = 1.02$, the flow at the center of the wake is approximately parallel to the trailing edge. The qualitative behavior of the flow in the gap at $x/c = 1.01$ is consistent with these trends; the signs of the flow angles can be determined from the signs of the appropriate probe-pressure differences even when the probe calibration range is exceeded. Apparently the flow in the viscous central wake is dominated by the outboard flow in the separated region on the lower surface.

The influence of an increase in blowing rate may be seen by comparing figures 11 and 15. The upper-surface boundary layer and wake velocities in the vicinity of the trailing edge are significantly greater at the higher blowing rate. The wall-jet profile at $x/c = 0.985$ is a composite of data from a five-hole-probe survey of the outer region and a three-hole-probe survey made near the surface. The three-hole-probe data are used in the supersonic region. The static-pressure distribution used in reducing the three-hole-probe data is the previously mentioned linear interpolation from the last subsonic point determined by the five-hole probe to the value measured at the surface. The pitch-plane inclination angles in the wakes are more negative than they are at the same locations at the lower blowing rate, resulting in a substantial region of flow at the margin of or outside the probe-calibration range for the innermost wake profile. The wake profiles also show substantial outboard flow, but the momentum added by the jet is sufficiently large that the deficits in velocity magnitude in the wakes are small. The two lower-surface boundary-layer profiles shown in figure 15 indicate that the increased blowing rate has also resulted in a forward movement of the lower-surface separation point.

Figures 16-18 present close-ups of wall-jet and wake profiles for the test conditions of figure 15 in the manner of figures 12-14.

Scalar Plots at $M_\infty = 0.425$, $\alpha = 0°$

The next group of plots, figures 19-22, present conventional velocity-magnitude and flow-angularity profiles for each of the locations surveyed at the three test conditions described previously. The boundary-layer and a portion of the wall-jet data were obtained with a three-hole probe, and the remaining wall-jet data and the wake data of figures 19-22 were obtained with a five-hole probe.

Figures 19a and 19c present u/u_∞, the velocity magnitude normalized by the free-stream velocity, plotted against z/c, the distance from the surface normalized by the streamwise chord, for the no-blowing case at each of the survey stations, $0.2 \leq x/c \leq 0.976$. The distance from the surface, z, is measured normal to the tunnel axis, which is also normal to the mean plane of the wing at $\alpha = 0°$. Corresponding profiles of yaw-plane flow angle, β, are shown in figure 19b (outboard flow is defined as positive β). Because of the small scale of some of the plots in figure 19 and in subsequent figures, individual plotting symbols are not always used. Approximately 40 points were obtained for each of the profiles of figure 19. The boundary-layer thickness increases substantially with increasing downstream distance, and the profiles become less full. The yaw-plane flow-direction profiles show slightly inboard flow at the forward chordwise stations. The aft station β-profiles are approximately streamwise at the outer edge of the boundary layer, and rotate outboard with decreasing distance from the surface. The flow velocities were too small near the surface at $x/c \geq 0.967$ to allow measurement of β.

Velocity-magnitude and flow-angularity profiles corresponding to the baseline test condition of figure 11 are presented in figure 20. The upper-surface data are presented in figures 20a-d. The boundary-layer thickness does not increase appreciably from mid-chord to the slot station. The profiles of β upstream of the slot indicate that the flow was approximately colinear, with a mean inboard inclination which increases with increasing downstream distance. Both the thin, full character of the velocity magnitude

profiles near the slot station and the inboard values of β imply strong entrainment by the jet. Wall-jet profiles obtained with both the straight and yawed three-hole probes and the five-hole probe are shown for $x/c = 0.977$ and 0.985. The wall-jet data obtained with the three-hole probes were reduced by employing the static-pressure distributions measured with the five-hole probe. Although the data obtained within the jet near the Coanda surface with the five-hole probe are included in figure 20 and in subsequent figures, this probe is too large to resolve the features of the flow near the surface with reasonable accuracy. The three-hole-probe data are clearly more reliable in this region. Agreement among the profiles at $x/c = 0.977$ with the three-hole probes is good for both u/u_∞ and β; agreement is also good between the three- and five-hole-probe data at $x/c = 0.977$ and 0.985 in the region above the jet. The two wall-jet profiles show that the jet is directed normal to the slot ($\beta \approx -45°$).

The corresponding lower-surface profiles are shown in figures 20e and f, beginning at $x/c = 0.5$. The profiles for $0.5 \leq x/c \leq 0.7$ are full, and the flow is approximately streamwise. Downstream of $x/c = 0.7$, the boundary-layer growth is rapid; at $x/c = 0.9$ the flow is near separation. In the inner region of the profile at $x/c = 0.967$, the probe pressures are approximately equal to the local static pressure, indicating reverse flow, and no data are plotted. Measured values of β become increasingly outboard with decreasing distance from the surface in the two downstream profiles. Near the surface at $x/c = 0.9$, the probe pressure differences are too small to allow accurate determination of β.

Velocity magnitude, β, and pitch-plane flow-angle (σ) profiles are presented in figures 20g-i for four wake survey stations (upward flow is defined as positive σ). The primary features of the wake profiles have been described in the preceeding discussion of the velocity vector plots.

Scalar profiles corresponding to the higher-blowing-rate test condition of figure 15 are presented in figure 21, for both the upper- and lower-surface boundary layers and wakes. The qualitative features of these profiles are similar to those of figure 20. An approximate data-reduction procedure was used for the five-hole-probe data in the supersonic regions near the surface

at x/c = 0.977 and 0.985, resulting in relatively poor agreement between the three- and five-hole-probe, velocity-magnitude data at these locations; however, the agreement for the corresponding β-profiles is surprisingly good.

Data from the central portion of the wake at x/c = 1.02, shown in figure 21g-i, lie at the edge of the calibration range for both β and α, and the resulting accuracy is marginal. The computed values of u/u_∞ and β appear plausible, but the values of σ show considerable scatter.

A sequence of lower-surface boundary-layer profiles corresponding to a range of blowing rates is presented in figure 22. These profiles show similar features, except that the lower-surface separation location varies with blowing rate. This point will be discussed in more detail subsequently. The discontinuity in the velocity-magnitude profile in figure 22c at x/c = 0.9 is a consequence of logic in the data-reduction program which simply sets the local stagnation pressure equal to the highest value measured by the ports of the three-hole probe when the local velocity is too low to use the calibration data.

Vector Plots and Oil-Flow Photographs at $M_\infty = 0.425$, $\alpha = 5°$

Composite views similar to those of figures 10, 11, and 15 are presented in figures 23 - 26 corresponding to $M_\infty = 0.425$, $\alpha = 5°$, and a range of blowing rates, from no blowing to $p_j/p_\infty = 1.6$. The upper-surface static-pressure distributions are presented in figure 6b. The data of figures 23 and 24 show relatively thick upper-surface boundary layers near the slot, relative to the data obtained at $\alpha = 0°$. The single wall-jet profile shown in figure 25 is significantly thinner than the comparable profiles at the lower blowing rate shown in figure 24. The substantial qualitative change in the flow field near the slot as the blowing rate is increased is illustrated in more detail by the velocity vector plots at x/c = 0.977 shown in figure 27 and the fluorescent oil-flow photographs of figure 28. The data of figure 27a show a low-velocity region between the boundary layer and the jet, significant outboard flow in the boundary layer above the jet, and nearly constant static pressure within the boundary layer. These features suggest that the boundary layer is in a state of incipient separation, and is not influenced significantly by the

presence of the jet. Figure 27b, corresponding to $p_j/p_\infty = 1.4$ shows a thinner, fuller boundary-layer profile with no low-velocity region between the boundary layer and the jet, negligible outboard flow in the boundary layer, and a static-pressure distribution which decreases with decreasing distance from the surface. These characteristics suggest significant entrainment of the boundary-layer flow by the jet, in contrast to the data of figure 27a. Figure 27c ($p_j/p_\infty = 1.6$) shows a fuller profile than the previous case, the cross-stream projection shows inboard flow above the jet, and the static-pressure variation through the boundary layer and the jet flow is more pronounced. Note that the scale of the static-pressure plot is different in figure 27c from the scale used in figures 27a and b.

Fluorescent oil-flow photographs obtained in this range of test conditions corroborate the results of the flow-field surveys. Figure 28 shows two upper-surface photographs corresponding to $M_\infty = 0.425$, $\alpha = 5°$, and $p_j/p_\infty = 1.2$ and 1.3, obtained from Keener et al., (ref. 2). The oil was injected from the surface orifices and photographed during a run. At the lower blowing rate, the oil streaks turn toward the spanwise direction near the slot, indicating separation at the slot, except in the immediate vicinity of the tip. The pattern obtained for $p_j/p_\infty = 1.3$ is significantly different, showing streamwise flow along the span up to the slot, indicating attached flow at the slot.

Scalar Plots at $M_\infty = 0.425$, $\alpha = 5°$

Scalar plots of the boundary-layer and wake profiles corresponding to $M_\infty = 0.425$ and $\alpha = 5°$ are presented in figures 29 - 33. The repeatability of the three-hole-probe data for the wall-jet profile of figure 32 is good, as is the agreement between the three- and five-hole-probe data in the region above the jet shown in figures 30 and 32. The contrast between the wall-jet plots of β in figures 30d and 31b, corresponding to $p_j/p_\infty = 1.2$ and 1.4, respectively, illustrate the point previously discussed concerning the qualitative differences between these flows.

The profiles presented in figure 33 at $x/c = 1.3$ illustrate the downward displacement of the wake with increasing blowing rate. The velocity magnitude profiles, figure 33a, indicate the vertical extent of each wake as determined

by viscous and jet flow effects. The yaw-plane flow-direction profiles show a shift in the value of β across each wake, and the pitch-plane profiles show linear variations of σ across the entire region included in each survey; no features distinguishing the viscous and inviscid regions are apparent in the σ-profiles.

Vector Plots at $M_\infty = 0.425$, $\alpha = 0°$

Figures 34-40 correspond to $M_\infty = 0.70$, $\alpha = 0°$. The surface static-pressure distributions for which boundary-layer and wake data were obtained at this Mach number and angle of attack are presented in figure 6c. Figures 34 and 35 are composite views similar to those shown in figures 10 and 11 at the lower Mach number. The data of figure 34 correspond to no blowing, and are qualitatively quite similar to the no-blowing case at the lower Mach number shown in figure 10. The data of figure 35 and the detailed profile data of figures 36-38 correspond to the same jet pressure ratio as in figure 11, $p_j/p_\infty = 1.4$, but a lower jet-momentum coefficient, $C_\mu = 0.0041$. The influence of the jet on the surrounding flow is clearly much less pronounced at this test condition. The upper-surface boundary-layer profiles in the vicinity of the jet are less full and show positive values of β near the surface upstream of the jet and at the location of minimum velocity in the profile downstream of the jet. The lower-surface separation line is apparently near the last measuring station on the lower surface. The reduced circulation is indicated by the reduced downward displacement of the wake centerline, relative to the data of figure 11.

Composite views corresponding to $M_\infty = 0.70$, $\alpha = 0°$, and $p_j/p_\infty = 1.8$ and 2.2 are presented in figures 39 and 40.

Vector Plots and Oil-Flow Photographs at $M_\infty = 0.70$, $\alpha = 5°$

A series of wall-jet profiles with the five-hole probe were obtained at $M_\infty = 0.70$, $\alpha = 5°$, and $x/c = 0.977$. Data obtained at the minimum and maximum blowing rates, $p_j/p_\infty = 1.2$ and 2.2 are presented in figures 41a and b. The corresponding upper-surface static-pressure distributions are shown in figure 6d. The boundary-layer flow above the jet appears to be separated, or

possibly in a state of incipient separation at this range of blowing rates, in contrast to the results obtained at $M_\infty = 0.425$. Note that both the profiles of figures 41a and b show low-velocity regions between the jet and the boundary-layer flow above the jet, and both cross-stream profiles show significant outboard flow above the jet. The oil-flow photograph of figure 42, obtained at $M_\infty = 0.70$, $\alpha = 5°$, and $p_j/p_\infty = 2.0$, indicates flow separation at the slot.

Scalar Plots at $M_\infty = 0.70$

Scalar profiles corresponding to all of the data obtained at $M_\infty = 0.70$ are presented in figures 43-47. The general features of these profiles are similar to those observed at $M_\infty = 0.425$. Of particular note are the irregular pitch-plane wake profiles, figures 44i and 45e, and the large excursions in the yaw-plane flow-direction profiles at $\alpha = 5°$ and $x/c = 0.977$, figure 47b.

Integral Properties and Skin Friction

Upper-Surface Displacement-Thickness Distributions

Upper-surface, streamwise displacement-thickness distributions, normalized by the streamwise chord, δ_1^*/c, are presented in figure 48. The boundary-layer thickness distributions are apparently unaffected by blowing for $x/c \leq 0.5$. Data corresponding to $M_\infty = 0.425$, $\alpha = 0°$, and jet conditions of no blowing, $p_j/p_\infty = 1.4$, and 1.8 are presented in figure 48a. The displacement thickness shown in figure 48a at $x/c = 0.5$ is approximately the same as that corresponding to flow over a flat plate at the free-stream conditions. In the vicinity of the slot, the displacement-thickness distribution for no blowing grows rapidly as the flow approaches separation. Data for the two blowing rates show values of displacement thickness immediately upstream of the slot which are essentially the same as those measured at mid-chord. Values of displacement thickness immediately upstream of the slot are greater at the test conditions of figure 48b, $M_\infty = 0.425$, $\alpha = 5°$, or the test conditions of figure 48c, $M_\infty = 0.70$, $\alpha = 0°$, than in figure 48a. In addition, the values of displace-

ment thickness near the slot remain significantly greater than the corresponding mid-chord values for the range of blowing rates included in figures 48b and c.

Skin Friction Determined From Velocity Profiles

Values of skin-friction coefficient, C_f, were determined from the attached boundary-layer profiles by fitting the inner region of the velocity magnitude profiles to the following generally accepted similarity law:

$$\frac{u}{u_\tau} = \frac{1}{0.41} \ln\left(\frac{zu_\tau}{\nu}\right) + 5.0 \qquad (3)$$

where u_τ is the shear velocity, $\sqrt{\tau_w/\rho}$; τ_w is the wall shear stress, ρ is the density, and ν is the kinematic viscosity. A range of values has been proposed for the constants in this equation; this situation is reviewed by Pierce et al. (ref. 10). Extension of the incompressible law-of-the-wall to flows with moderate compressibility effects is usually accomplished by evaluating the density and viscosity at the wall temperature. Prahlad (ref. 11) proposed that this similarity law be extended to three-dimensional flows by replacing the two-dimensional velocity in equation (1) with the velocity magnitude. Pierce et al. (ref. 12) concluded that the magnitude of the wall shear stress could be determined by the Clauser-chart technique (ref. 13) to within 5-10% if data in the range $10 \leq z^+ \leq 100$ ($z^+ = zu_\tau/\nu_w$) were used. This conclusion was limited to monotonically skewed boundary layers with an approximate maximum of 15-20° of skew.

Figure 49 illustrates the method by which this technique was applied to the present data. Lower-surface velocity-magnitude profiles corresponding to the baseline test conditions are plotted in semi-logarithmic coordinates. In these coordinates, equation (1) represents a family of straight lines with C_f as a parameter. Since the straight lines in figure 49 represent the range $10 \leq zu_\tau/\nu \leq 1000$, it is apparent that the sublayer and the inner portion of the logarithmic region are not resolved in these data. The data show a monotonically decreasing trend of C_f with x/c.

Lower-Surface Separation

The influence of blowing rate on the position of the lower-surface separation line at $\alpha = 0°$ is shown in figure 50, in which C_f is plotted as a function of x/c. A relatively extensive set of data is presented in figure 50a for $M_\infty = 0.425$, and limited data are presented in figure 50b for $M_\infty = 0.70$. It is assumed that extrapolation of values of C_f to zero provides a reasonable estimate of the separation-line location. (Actually, the velocity magnitudes become small and the local flow direction becomes parallel to the wing generators near separation.) In figure 50a it is shown that the separation line moves upstream with increasing blowing rate, up to $p_j/p_\infty = 1.8$, but an additional increase of p_j/p_∞ to 2.2 does not produce an additional forward movement of the separation line. It is in this range of blowing rates that the performance data (c_ℓ versus C_μ) show no additional increase of lift with increasing blowing rate. Blowing has a smaller effect on the position of the lower-surface separation line at $M_\infty = 0.70$, as shown in figure 50b.

Streamwise displacement-thickness data corresponding to the skin-friction data of figure 50 are presented in figure 51, where the approach to separation is indicated by a rapid growth in displacement thickness with increasing downstream distance. Vertical dashed lines in figure 51a indicate the separation locations inferred from the skin-friction data.

Skin-Friction Measurements With Obstacle Blocks and Preston Tubes

Upper- and lower-surface skin friction distributions at $\alpha = 0°$, obtained by the obstacle-block, Preston-tube, and Clauser-chart techniques, are presented in figures 52 - 54 for both test Mach numbers and a range of blowing rates. Boundary-layer data were examined to determine the range of validity of the Preston tube and the obstacle-block data. Determination of skin friction by Preston tubes is generally limited to situations in which the Preston-tube diameter is less than the thickness of the semi-logarithmic region. This criterion was satisfied in the present experiments.

The obstacle-block calibration data of Nituch (ref. 7) can be represented by the following equation:

$$\frac{\Delta p}{\tau_w} = 20.3 \left(\frac{\Delta p h^2}{\rho \nu^2}\right)^{0.117} \quad \text{, for } h/d = 3.0 \text{ ,} \tag{4}$$

where h is the obstacle-block height, d is the static-pressure orifice diameter, and Δp is the difference between the undisturbed static pressure and the pressure measured in the presence of the obstacle block. The calibration data were obtained in incompressible flow; values of ρ and ν for the present data were evaluated at the wall temperature. The data of reference 7 indicate that skin-friction errors no greater than 3% will be incurred if the height of the obstacle block is less than twice the thickness of the semi-logarithmic region of the local undisturbed boundary layer. (For this purpose, the thickness of the semi-logarithmic region is defined as the height above the wall at which the mean velocity profile deviates from the semi-logarithmic law of the wall profile by 5%.) This criterion is satisfied in the present range of test conditions aft of approximately mid-chord. The height of the obstacle blocks is comparable to the thickness of the semi-logarithmic region of the undisturbed boundary layer for $x/c \approx 0.9$ on the upper surface and $x/c \approx 0.7$ on the lower surface at most test conditions.

An error in the Δp value that was used to determine skin friction from the Preston-tube and obstacle-block data resulted from imperfect repeatability in test conditions. The magnitude of this error was estimated by comparing leading-edge static-pressure distributions, $0 \leq x/c \leq 0.15$, obtained from runs with the clean wing, to data from runs with the Preston tubes or obstacle blocks installed. These comparisons showed the error in C_p to be approximately 0.02. This error in C_p leads to errors in C_f of 0.0002 and 0.00016 at free-stream Mach numbers of 0.425 and 0.70, respectively.

Results presented in figures 52 and 53 show reasonable agreement among the three methods of determining skin friction at $M_\infty = 0.425$, for $x/c < 0.85$ on the upper surface, and upstream of separation on the lower surface. In the immediate vicinity of the jet on the upper surface, the data are more scattered and the trends are less consistent; it is possible that the three-dimensionality of the boundary-layer profiles immediately upstream of the jet has resulted in significant errors. The lower-surface data taken downstream of the minima in C_f indicated by the obstacle-block data are not meaningful

because the flow was separated at those locations. Some of the same trends are present in the data of figure 54, obtained at $M_\infty = 0.70$. These data show greater discrepancies between the Preston-tube data and the average of the obstacle-block results on the upper surface for $x/c < 0.85$ than the corresponding data obtained at $M_\infty = 0.425$, shown previously. The lower-surface skin-friction data of figure 54b show the reduced influence of blowing on the location of the lower-surface separation at $M_\infty = 0.70$, relative to $M_\infty = 0.425$.

CONCLUDING REMARKS

Boundary-layer and wake-survey data were obtained at mid-semispan in the flow about a 45°-swept, circulation-control wing at free-stream Mach numbers of 0.425 and 0.70. Boundary-layer profiles forward on the wing on both upper and lower surfaces are approximately streamwise and two-dimensional. The flow in the vicinity of the jet exit and in the near wake is highly three-dimensional. Qualitative variations in flow-field features with free-stream Mach number and jet blowing rate are illustrated by velocity vector plots. The jet flow near the slot on the Coanda surface is directed normal to the slot, or 45° inboard. All near-wake surveys, including surveys obtained 1% chord downstream of the trailing edge, show large outboard flows at the center of the wake. At Mach 0.425 and 5° angle of attack, a range of jet-blowing rates was found for which an abrupt transition from incipient separation to attached flow occurs in the boundary layer upstream of the slot. The variation in the lower-surface separation location with blowing rate was determined from boundary-layer, Preston-tube, and obstacle-block measurements. The influence of blowing on the size of the lower-surface separated region is shown to be much more pronounced at $M_\infty = 0.425$ than at $M_\infty = 0.70$.

APPENDIX

Tabulated data from this investigation are contained on microfiche pages located in an envelope in the back cover of this report. The following is a listing of these tables, together with brief descriptions of the contents of each table.

Table A1. Nomenclature. This table contains definitions of the terminology used in the remaining tables.

Table A2. Run summary - runs containing static-pressure distributions corresponding to boundary-layer and wake survey data. This table contains the NASA run and sequence numbers, M_∞, α, p_j/p_∞, C_μ, c_ℓ, tunnel stagnation conditions, and test-section static pressure.

Table A3. Static-pressure distributions at mid-semispan corresponding to test conditions for which boundary-layer and wake survey data were obtained. This table contains values of C_p and x/c for the runs listed in Table A2. The upper-surface data are from the diagonal row of pressure orifices, and the lower-surface data are from row 4, 2y/b = 0.7.

Table A4. Summary data from boundary-layer and wake surveys - two-orifice data. This table contains run numbers, edge conditions, integral properties, and skin friction coefficients from those runs made with the three-hole probes for which only two orifices were functioning. Data from these surveys were reduced by use of a constant value of static pressure.

Table A5. Detailed profiles - two-orifice data. Each page of this table corresponds to one of the profiles listed in Table A4. The lines at the top of each page include the summary information of Table A4. The remaining tabulation contains values of z/c, probe pressure, Mach number, velocity, and yaw-plane inclination angle.

Table A6. Summary data from boundary-layer and wake surveys - three-orifice data. This table contains the same type of information as Table A4, except that these data are from runs made with the three-hole probes for which

all three orifices were functioning. Data from these surveys were reduced using a constant value of static pressure.

Table A7. Detailed profiles - three-orifice data. This table contains the same type of information as Table A5, with the exceptions noted in the preceding paragraph.

Table A8. Summary data from wall-jet surveys - two- and three-orifice data with variable static pressure. This table is a run summary similar to Table A4, and includes only surveys obtained above the Coanda surface. Static-pressure distributions obtained from corresponding five-hole-probe surveys were used in reducing the data.

Table A9. Detailed profiles - two- and three-orifice data with variable static pressure. This table contains the detailed profile data for the runs listed in Table A8.

Table A10. Summary data from wall-jet and wake surveys - five-orifice data. This table is a summary of surveys obtained with the five-hole probe.

Table A11. Detailed profiles - five-orifice data. This table contains the detailed profile data from the runs listed in Table A10.

Table A12. Run summary - obstacle-block and Preston-tube data. This table contains run numbers, test-section conditions, and values of p_j/p_∞ for the runs in which the obstacle blocks and Preston tubes were used, plus similar data for corresponding runs with the clean wing.

Table A13. Obstacle-block and Preston-tube data. For the runs listed in Table A12, this table contains pressure orifice locations, C_p values obtained with both the clean wing and with the obstacle blocks or Preston tubes installed, and values of C_f.

REFERENCES

1. Wood, Norman J.; and Nielsen, Jack N.: Circulation Control Airfoils Past, Present, Future. AIAA Paper No. 85-0204, Jan. 1985.
2. Keener, Earl R.; Sanderfer, Dwight T.; and Wood, Norman J.: Pressure Distributions and Oil-Flow Patterns for a Swept Circulation-Control Wing. Proceedings of the 1986 Circulation Control Workshop, Session No. 3. NASA CP-2432, Aug. 1986.
3. Wood, Norman, J.; and Conlon, John A.: The Performance of a Circulation Control Airfoil at Transonic Speeds. AIAA Paper No. 83-0083, Jan. 1983.
4. Wood, Norman J.; and Sanderfer, Dwight T.: Transonic Performance of Two Circulation Control Airfoils. NASA TM X-86767, 1987.
5. Patel, V. C.: Calibration of the Preston Tube and Limitations on its Use in Pressure Gradients. J. Fluid Mech., vol. 23, part 1, Sept. 1965, pp. 185-208
6. Head, M. R.; Vasanta Ram, V.: Simplified Presentation of Preston Tube Calibration. The Aeronautical Quarterly of the Royal Aeronautical Society, vol. 22, part 3, Aug. 1971, pp. 295-300.
7. Nituch, M. J.: The Use of Congruent Obstacle Blocks for the Indirect Measurement of Turbulent Skin Friction on Smooth Surfaces. M. E. Thesis, Carleton U., Ottawa, Ontario, Aug. 1972.
8. Dudzinski, Thomas J.; and Krause, Lloyd N.: Flow-Direction Measurement with Fixed-Position Probes. NASA TM X-1904, 1969.
9. Spaid, Frank W.; Dahlin, John A.; Bachalo, William D.; and Stivers, Louis, S., Jr.: An Experimental Study of Transonic Flow About a Supercritical Airfoil. NASA TM 81336, 1983.
10. Pierce, F. J.; McAllister, J. E.; and Tennant, M. H.: Near-Wall Similarity in Three-Dimensional Turbulent Boundary Layers, Part I: Model Review. **Three-Dimensional Turbulent Shear Flows**, The American Society of Mechanical Engineers, New York, 1982, pp. 85-95.
11. Prahlad, T. S.: Wall Similarity in Three-Dimensional Turbulent Boundary Layers. AIAA J., vol. 6. no. 9, Sept. 1968, pp. 1772-1774.
12. Pierce, F. J.; McAllister, J. E.; and Tennant, M. H.: Near-Wall Similarity in Three-Dimensional Turbulent Boundary Layers, Part II: Pressure-Driven Flow Results. **Three-Dimensional Turbulent Shear Flows**, The American Society of Mechanical Engineers, New York, 1982, pp. 96-103.

13. Clauser, F. H.: Turbulent Boundary Layers in Adverse Pressure Gradients, J. Aeronaut. Sci., vol. 21, no. 2, Feb. 1954, pp. 91-108.

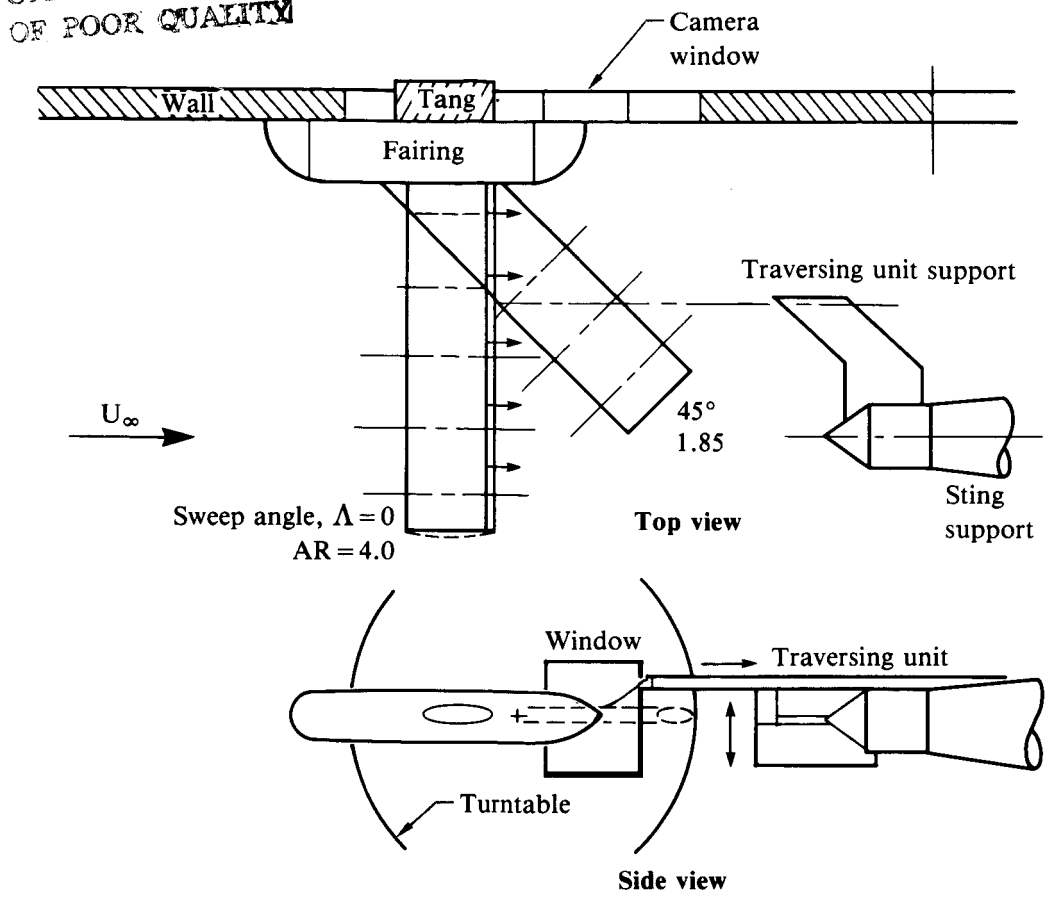

Figure 1. Sketch of model and traversing unit installation.

(a) **(b)**

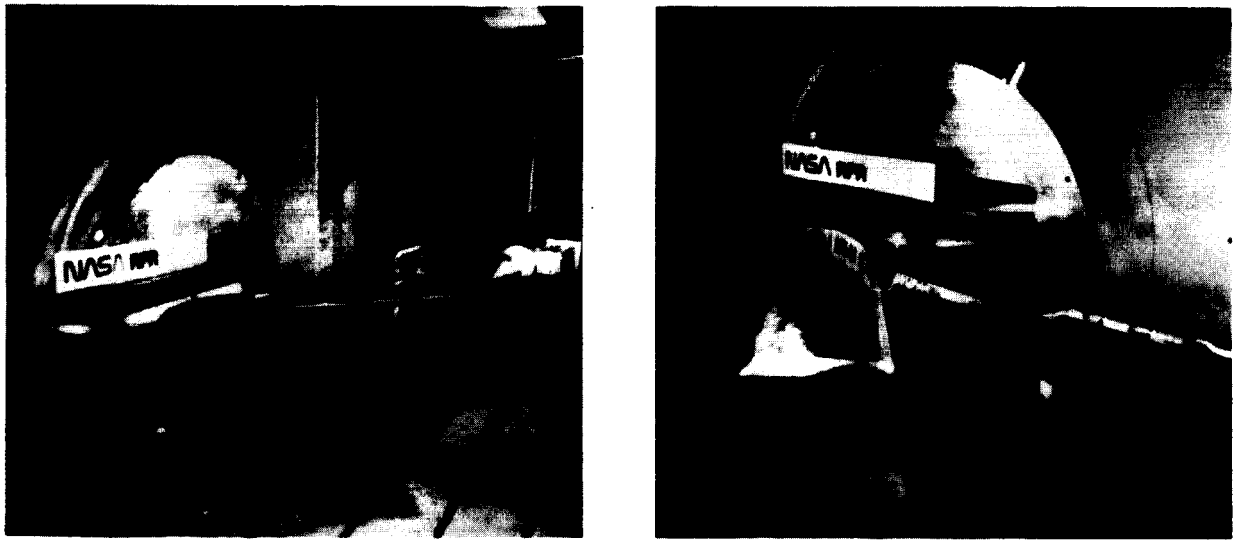

Figure 2. Wing model at a sweep angle of 45° and probe traversing unit.

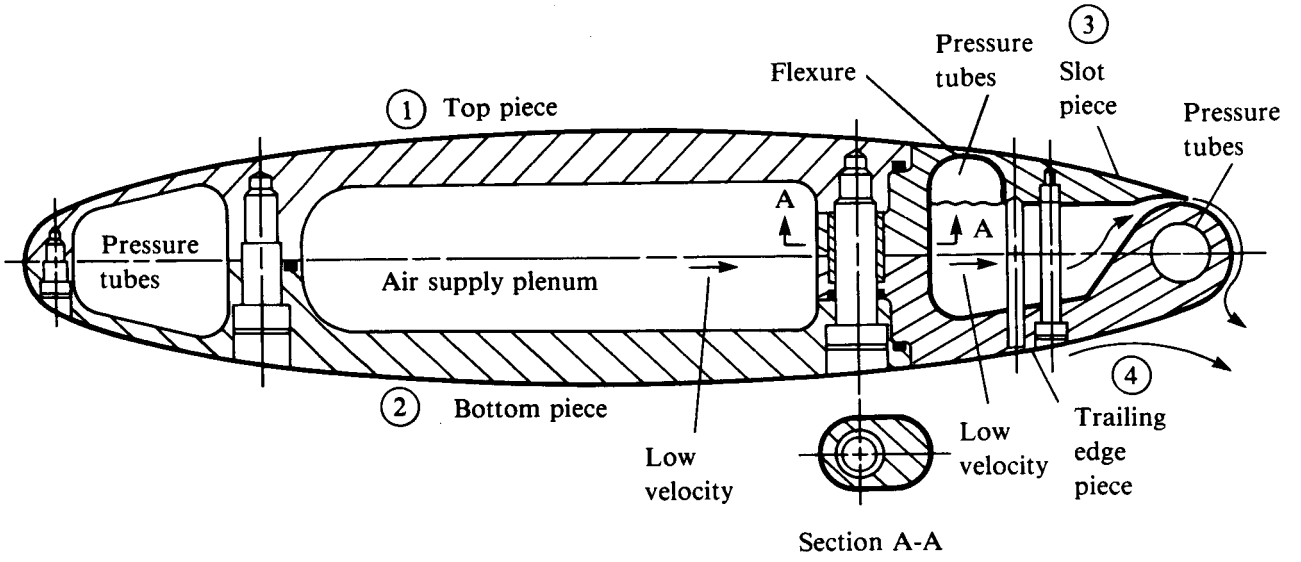

Figure 3. Sketch of wing section showing four-piece construction, bolts, set screw, and adjusting screw for slot height.

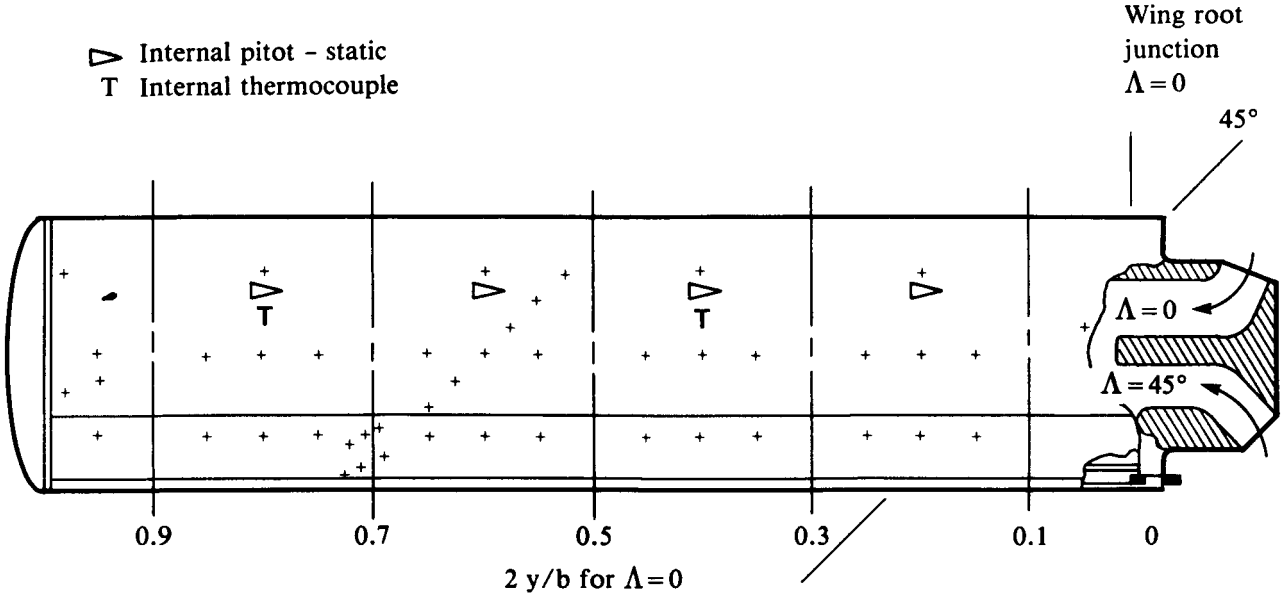

(a) Layout of static-pressure orifices.

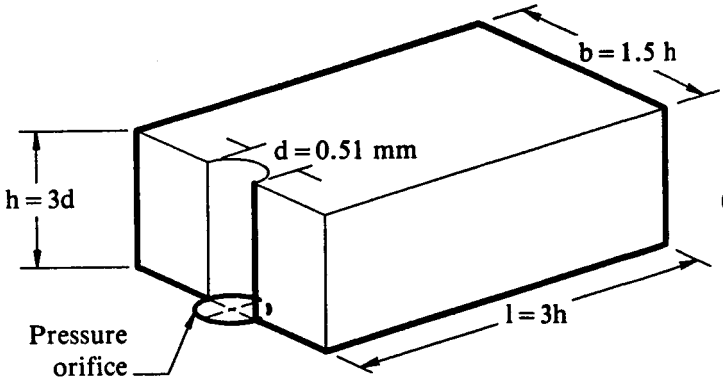

(b) Obstacle block

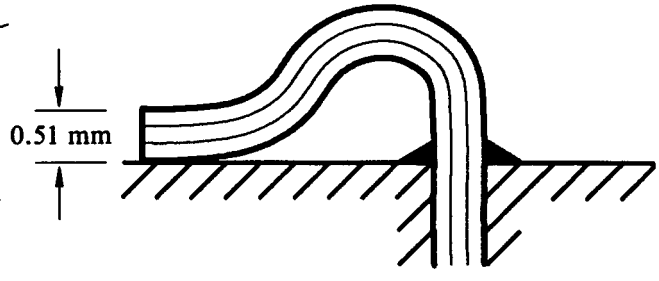

(c) Preston tube cemented into wing pressure orifice

Figure 4. Wing instrumentation.

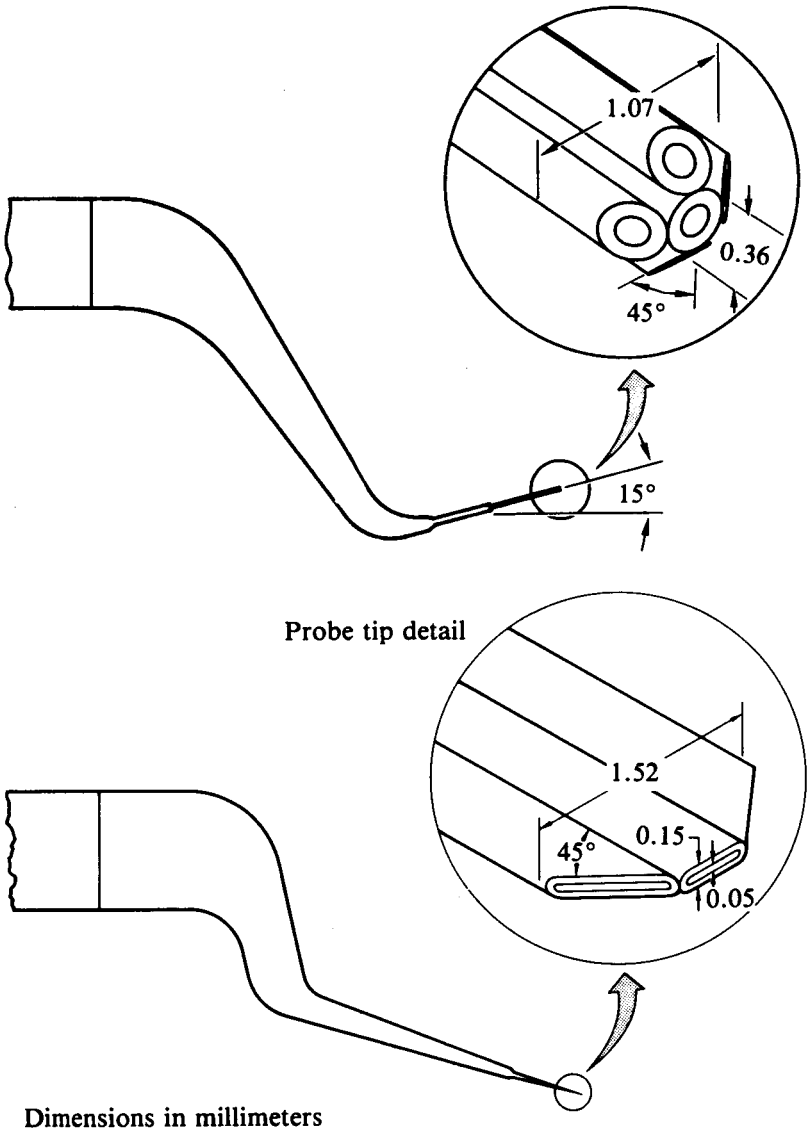

Figure 5. Three- and five-hole probes.

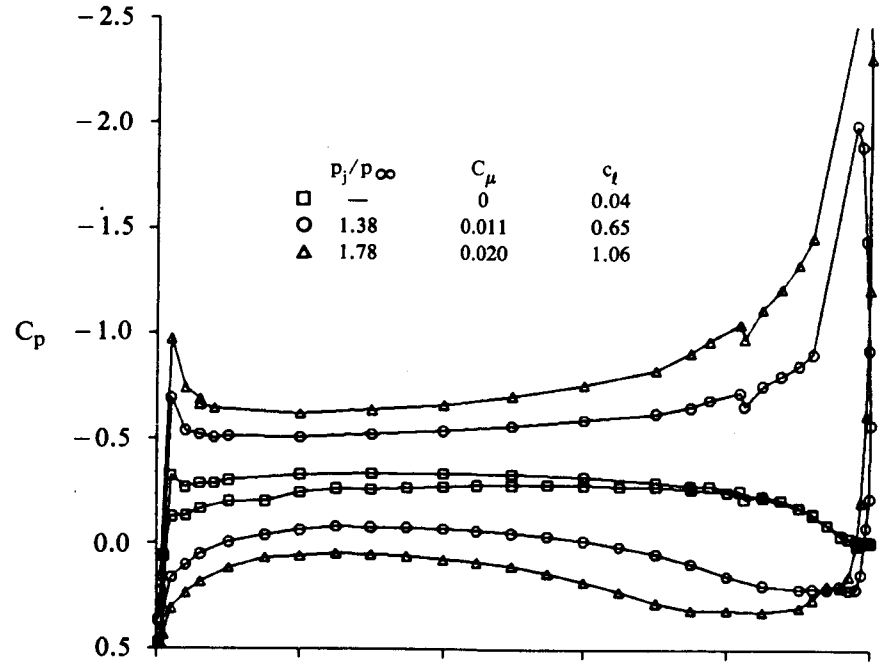

(a) $M_\infty = 0.425$, $Re_c = 2.27 \times 10^6$, $\alpha = 0°$

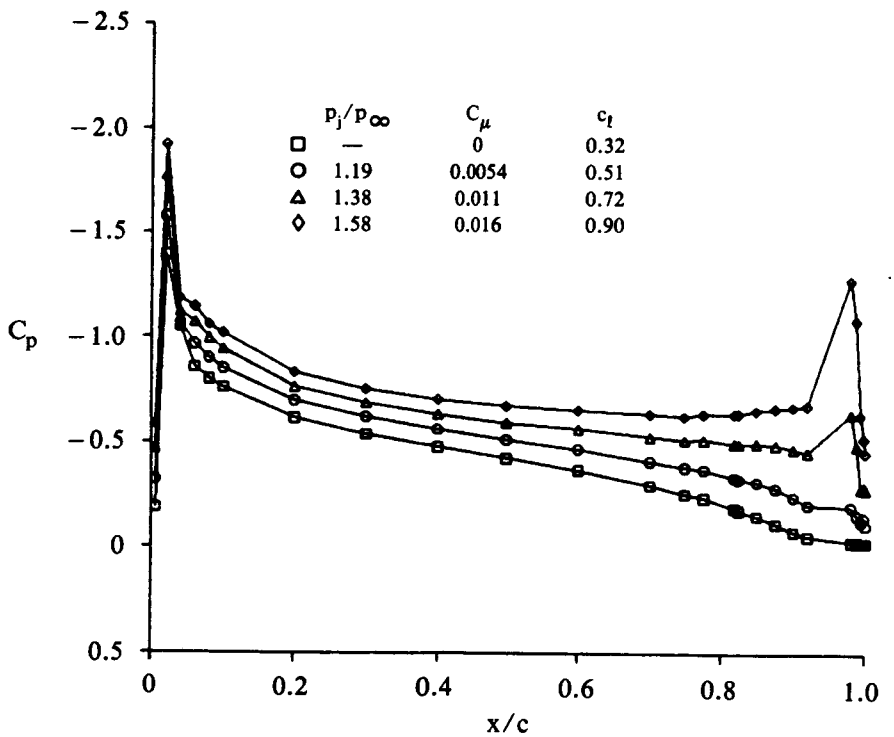

(b) Upper-surface data, $M_\infty = 0.425$, $Re_c = 2.24 \times 10^6$, $\alpha = 5.0°$

Figure 6. Wing static-pressure distributions at mid-semispan.

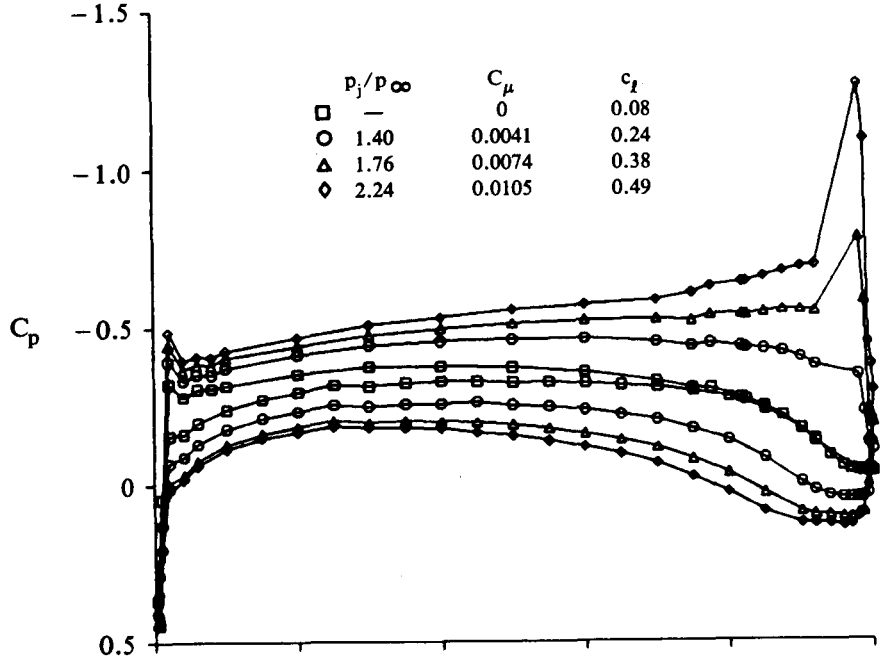

(c) $M_\infty = 0.70$, $Re_c = 3.15 \times 10^6$, $\alpha = 0°$

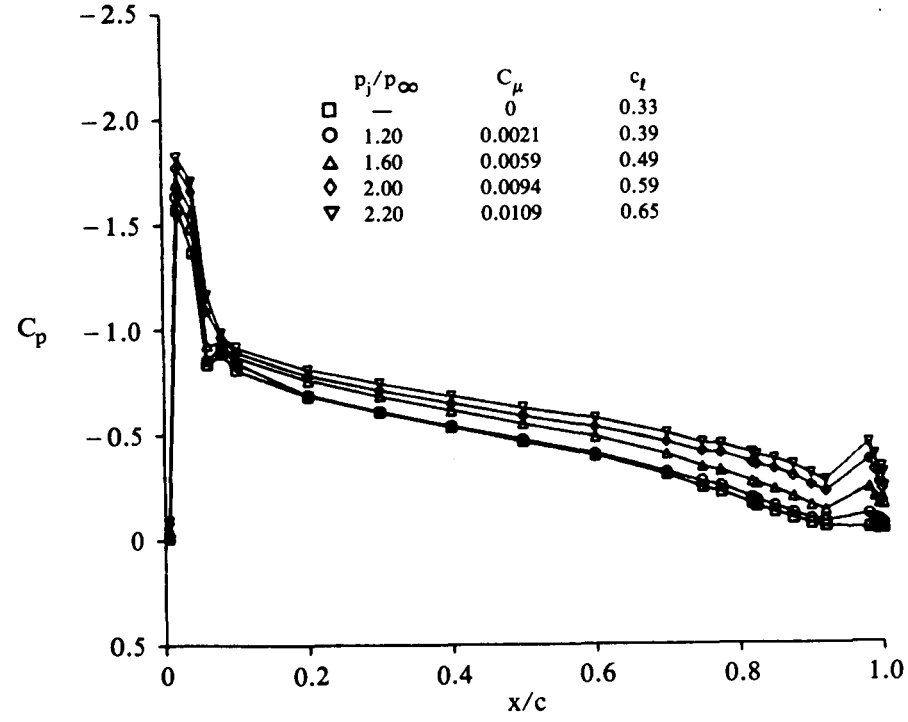

(d) Upper-surface data, $M_\infty = 0.70$, $Re_c = 3.15 \times 10^6$, $\alpha = 5°$

Figure 6. (Cont.) Wing static-pressure distributions at mid-semispan.

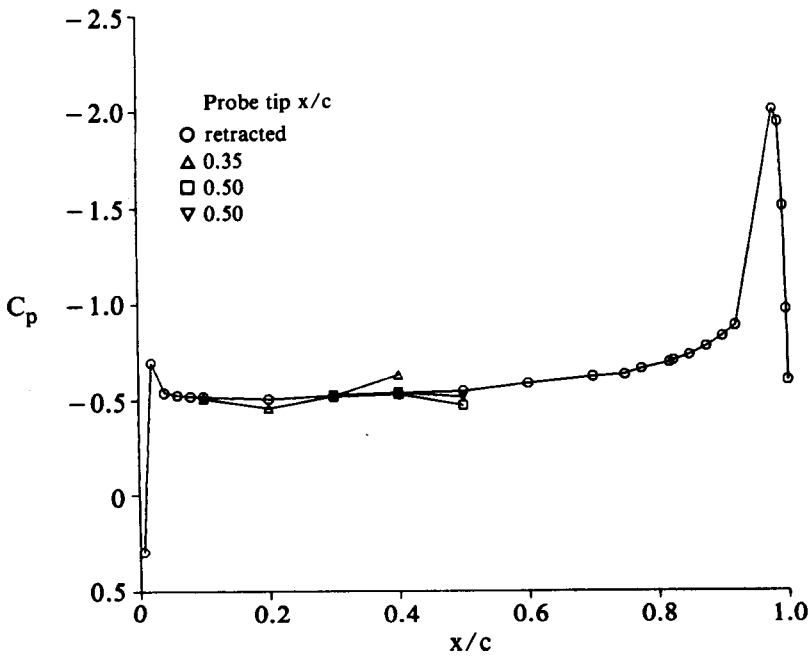

(a) $p_j/p_\infty = 1.4$, forward probe locations

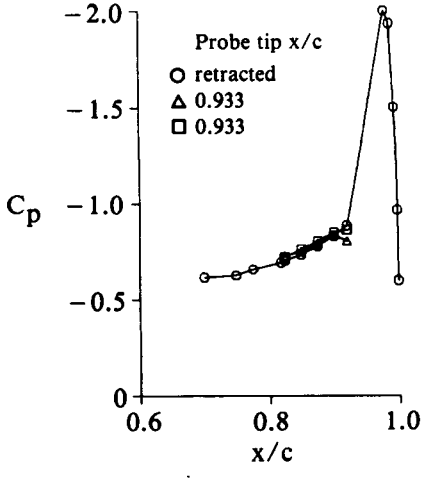

(b) $p_j/p_\infty = 1.4$, probe $x/c = 0.933$

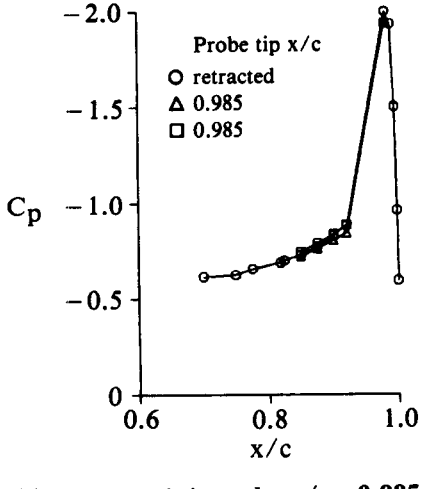

(c) $p_j/p_\infty = 1.4$, probe $x/c = 0.985$

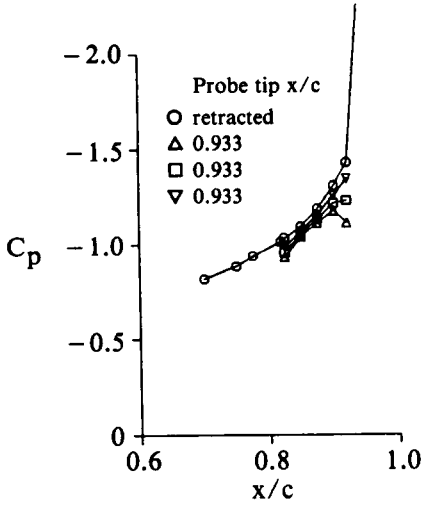

(d) $p_j/p_\infty = 1.8$, probe $x/c = 0.933$

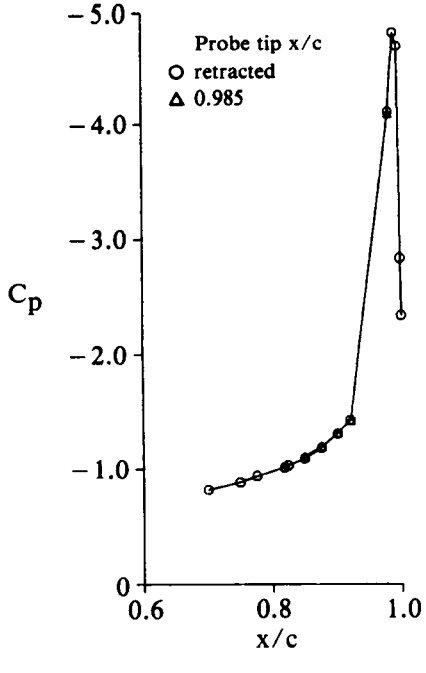

(e) $p_j/p_\infty = 1.8$, probe $x/c = 0.985$

Figure 7. Influence of probe on surface static-pressure distributions, $M_\infty = 0.425$, $\alpha = 0°$.

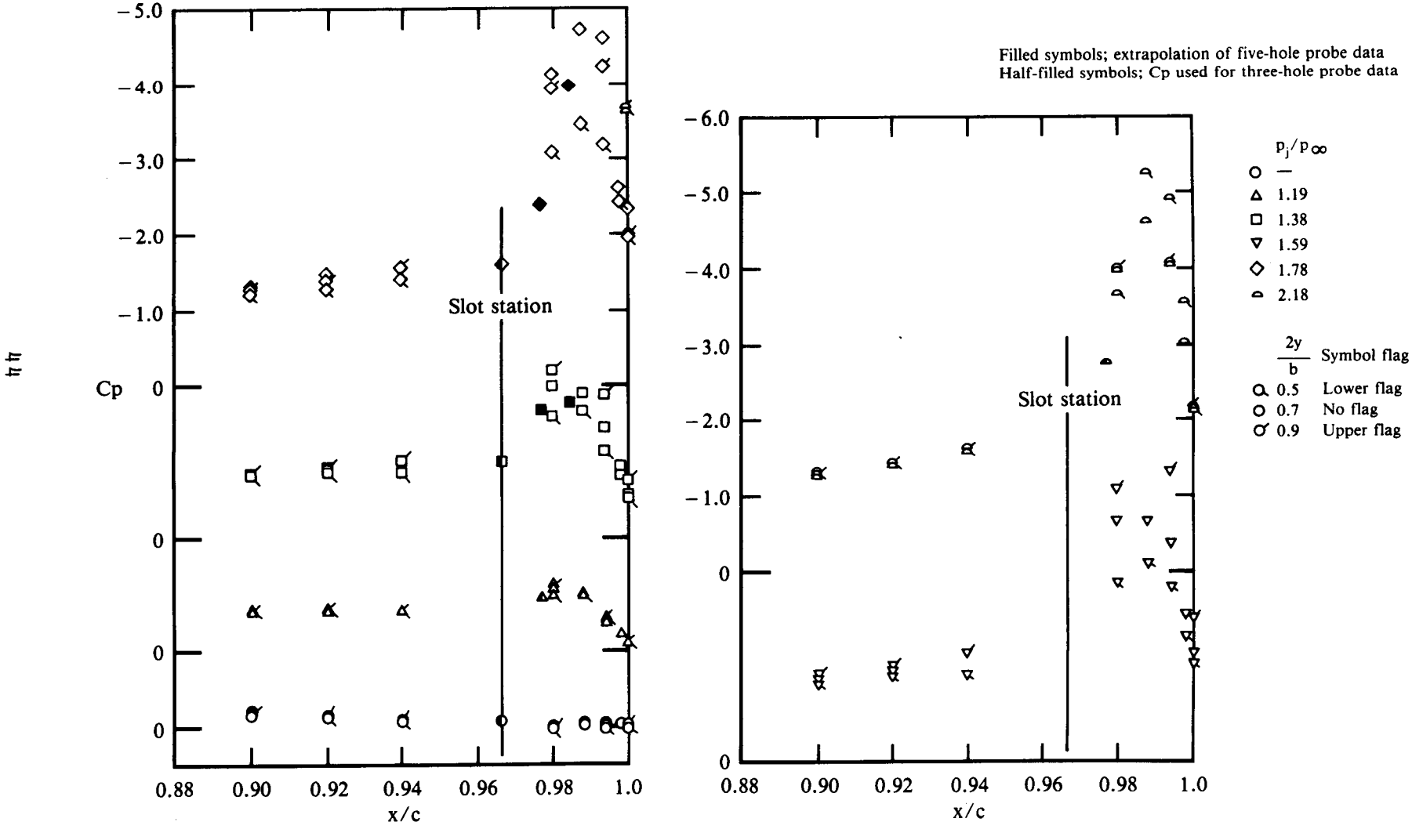

(a) $M_\infty = 0.425$, $\alpha = 0°$

Figure 8. Upper-surface static-pressure distributions in vicinity of slot.

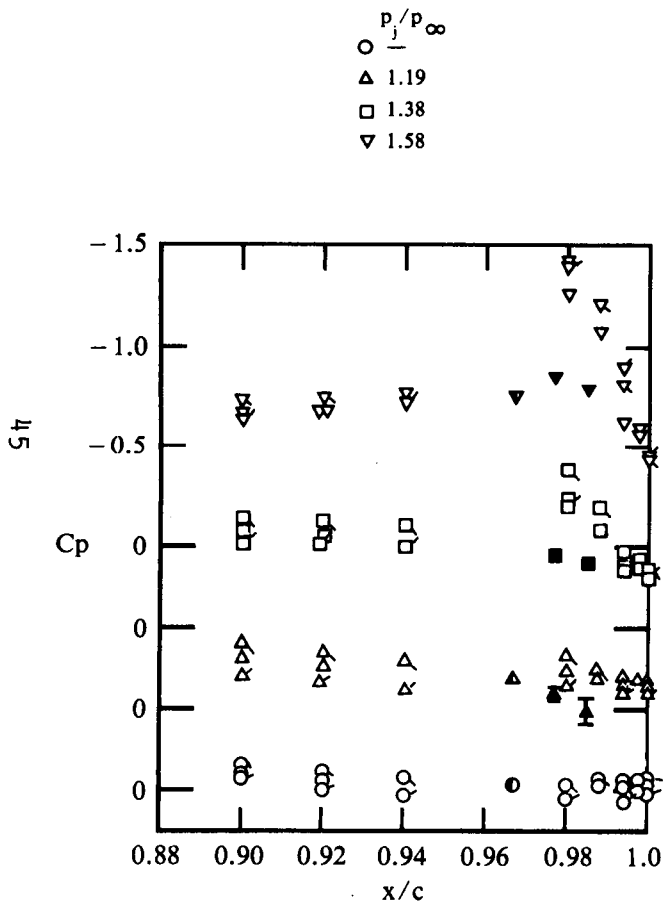

Figure 8. (b) $M_\infty = 0.425$, $\alpha = 5°$

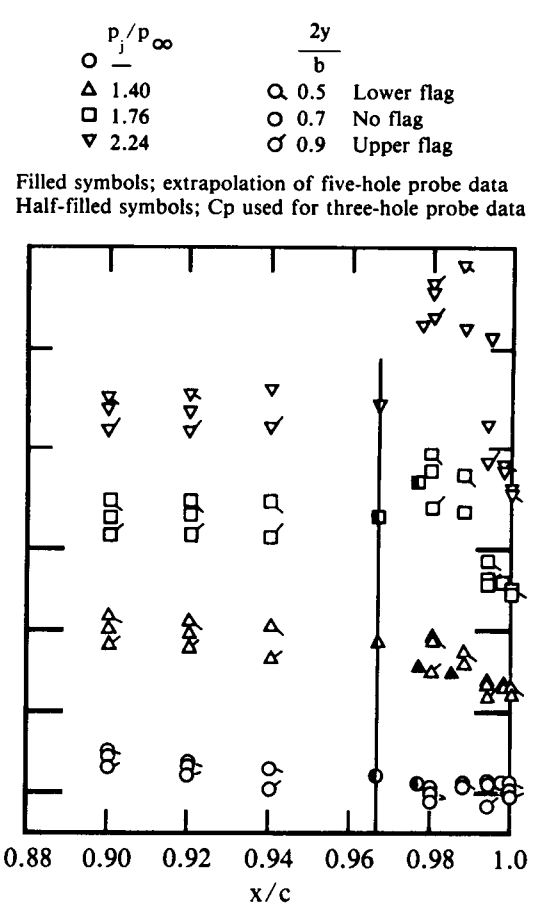

Figure 8. (c) $M_\infty = 0.7$, $\alpha = 0°$

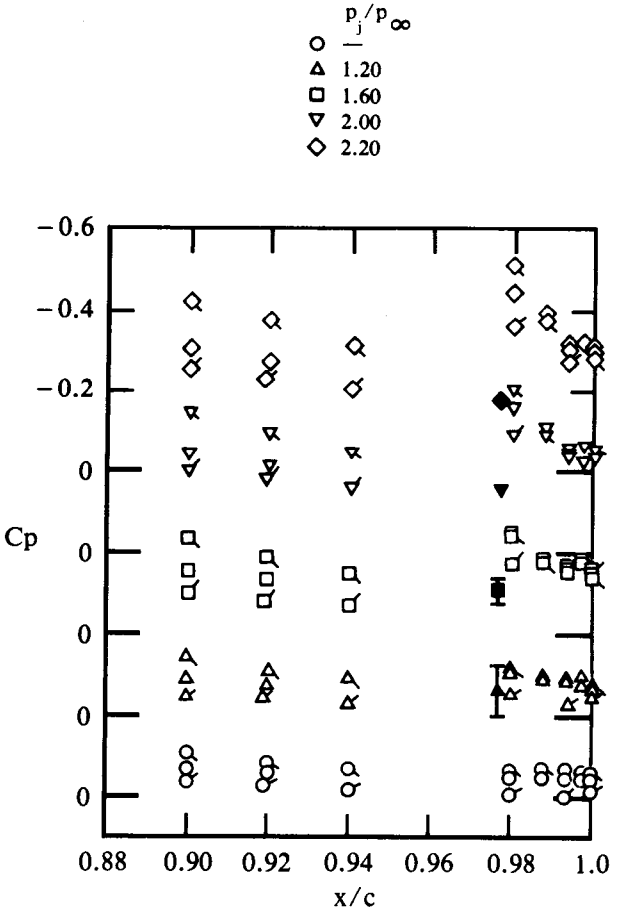

Figure 8. (d) $M_\infty = 0.7$, $\alpha = 5°$

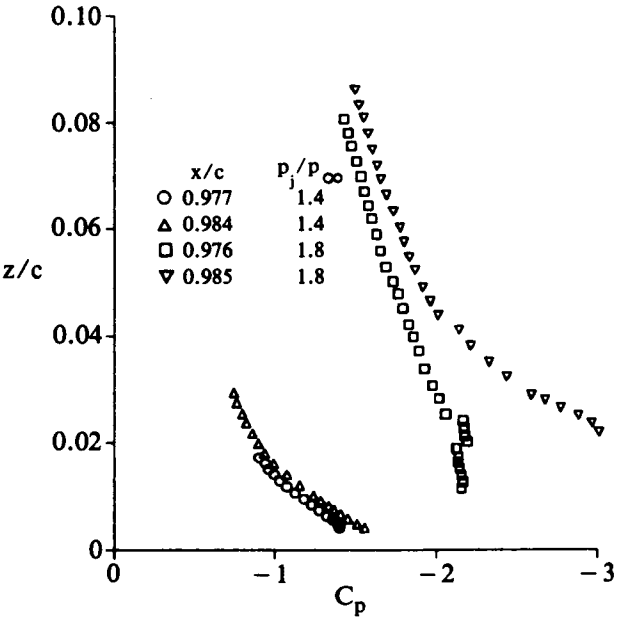

(a) $M_\infty = 0.425$, $\alpha = 0°$

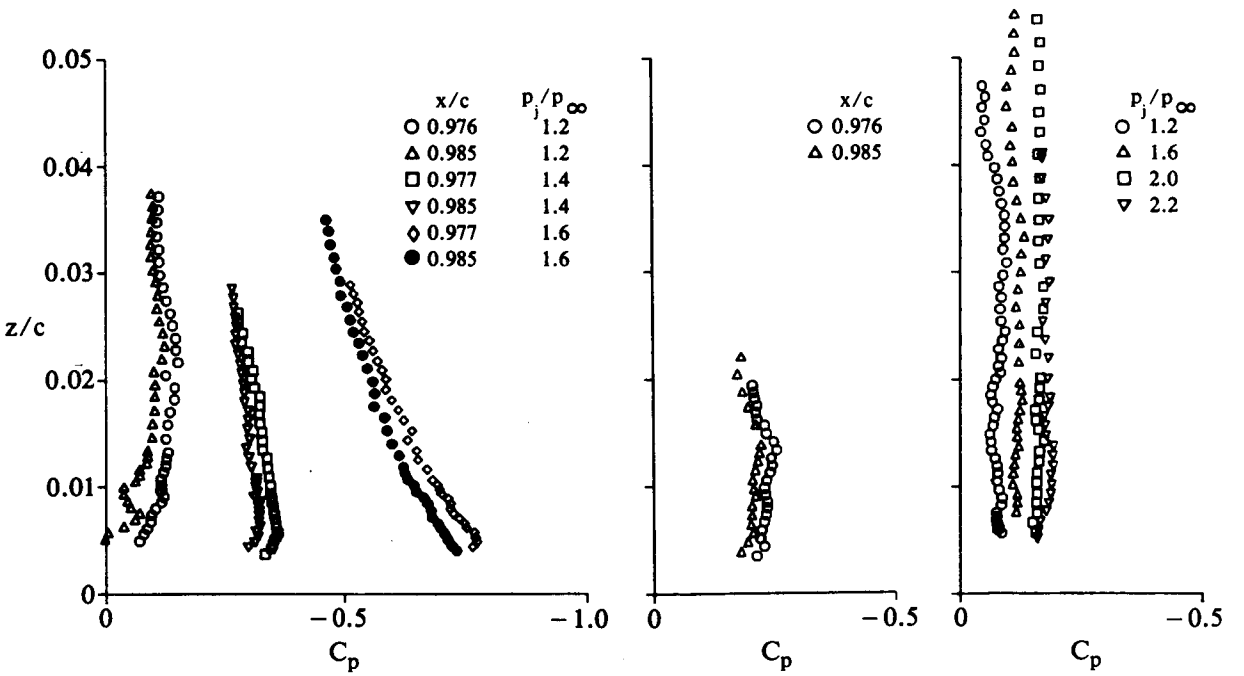

(b) $M_\infty = 0.425$, $\alpha = 5°$

(c) $M_\infty = 0.7$, $\alpha = 0°$, $p_j/p_\infty = 1.4$

(d) $M_\infty = 0.70$, $\alpha = 5°$, $x/c = 0.977$

Figure 9. Static-pressure profiles above wall jet.

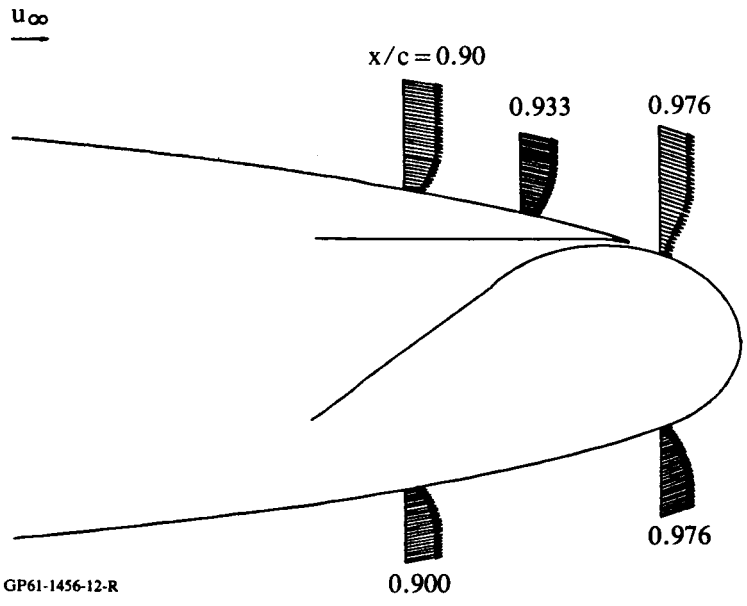

Figure 10. Velocity components in streamwise section plane; $M_\infty = 0.425$, $\alpha = 0°$, no blowing.

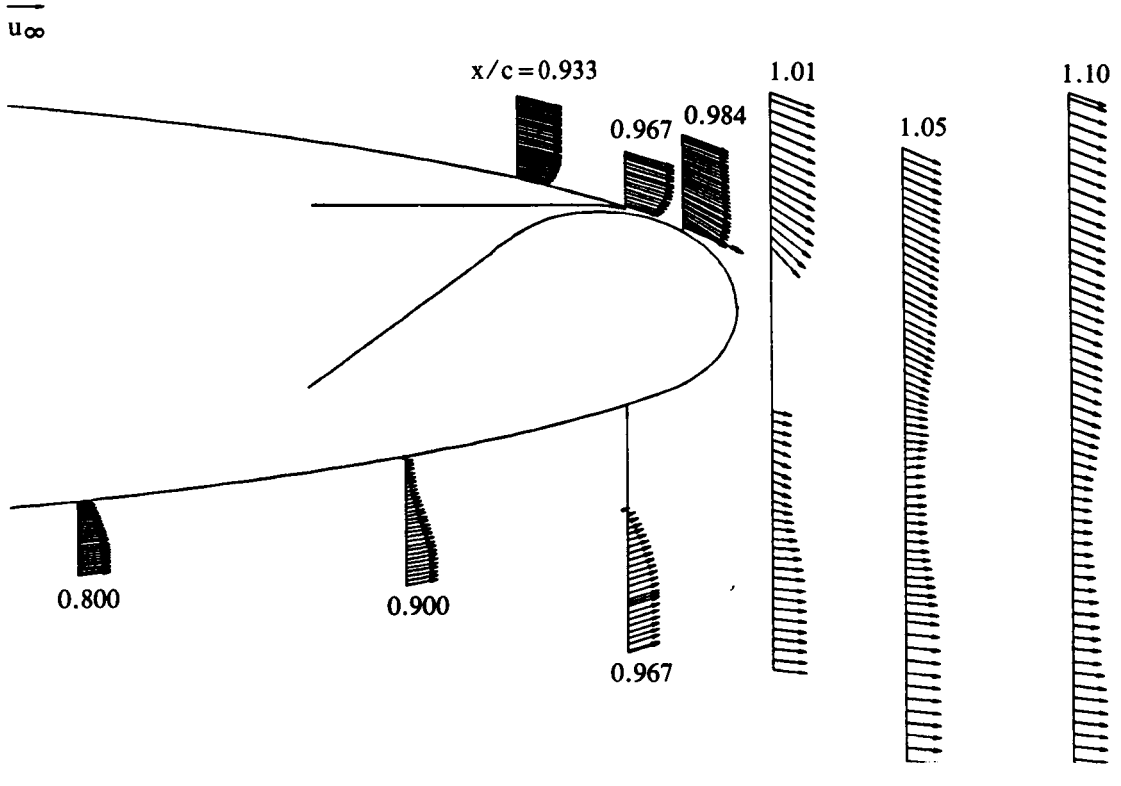

Figure 11. Velocity components in streamwise section plane; $M_\infty = 0.425$, $\alpha = 0°$, $p_j/p_\infty = 1.4$.

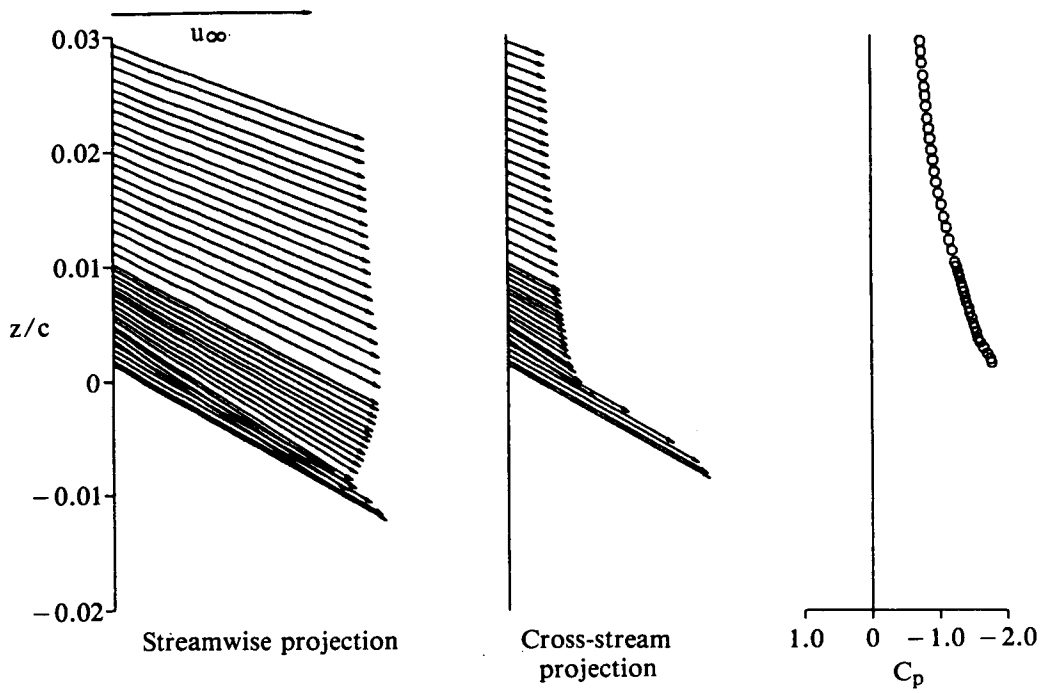

Figure 12. Wall-jet velocity and static-pressure profiles; $M_\infty = 0.425$, $\alpha = 0°$, $p_j / p_\infty = 1.4$, $x/c = 0.984$.

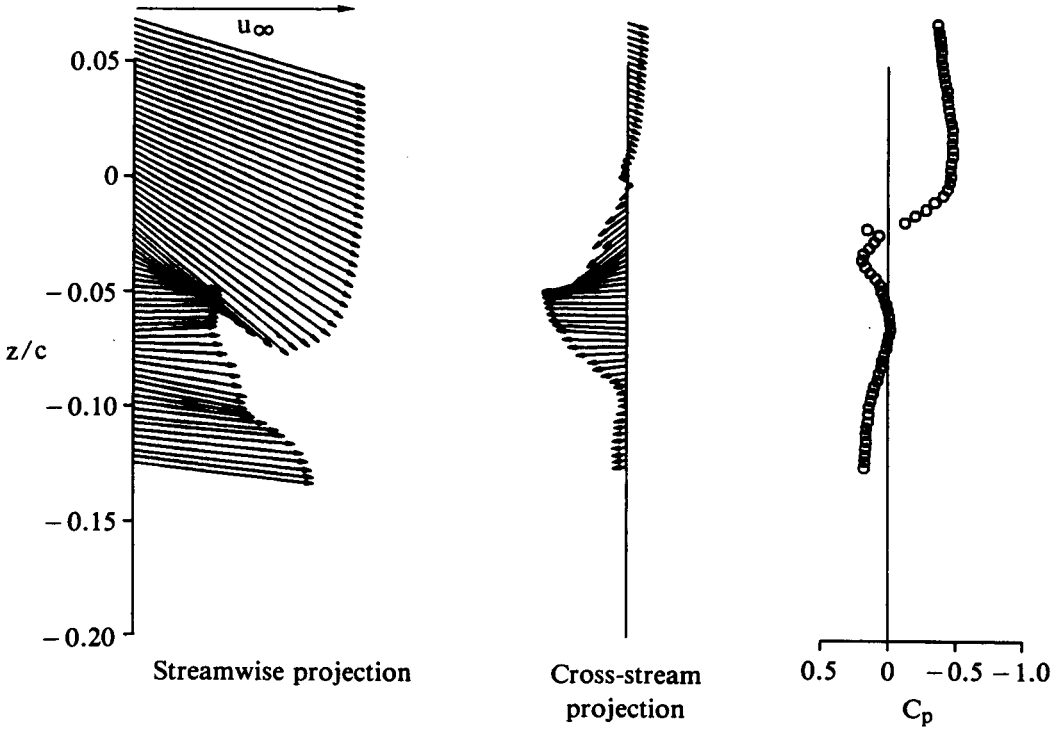

Figure 13. Wake velocity and static-pressure profiles; $M_\infty = 0.425$, $\alpha = 0°$, $p_j/p_\infty = 1.4$, $x/c = 1.02$.

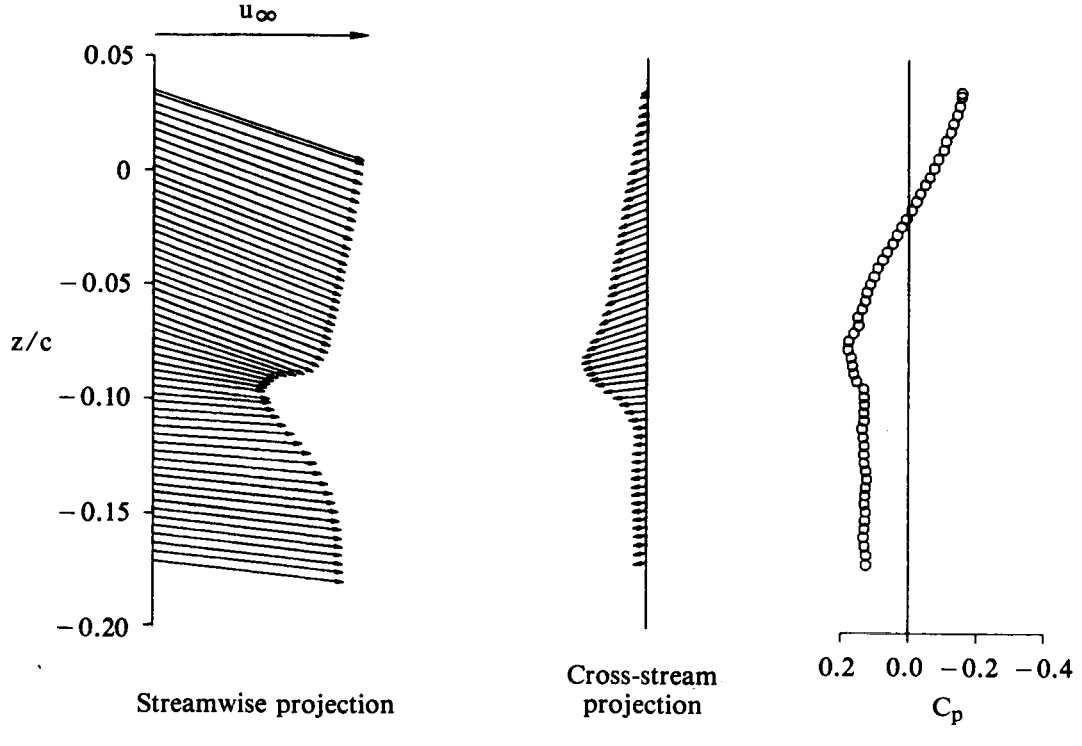

Figure 14. Wake velocity and static-pressure profiles; $M_\infty = 0.425$, $\alpha = 0°$, $p_j/p_\infty = 1.4$, $x/c = 1.10$.

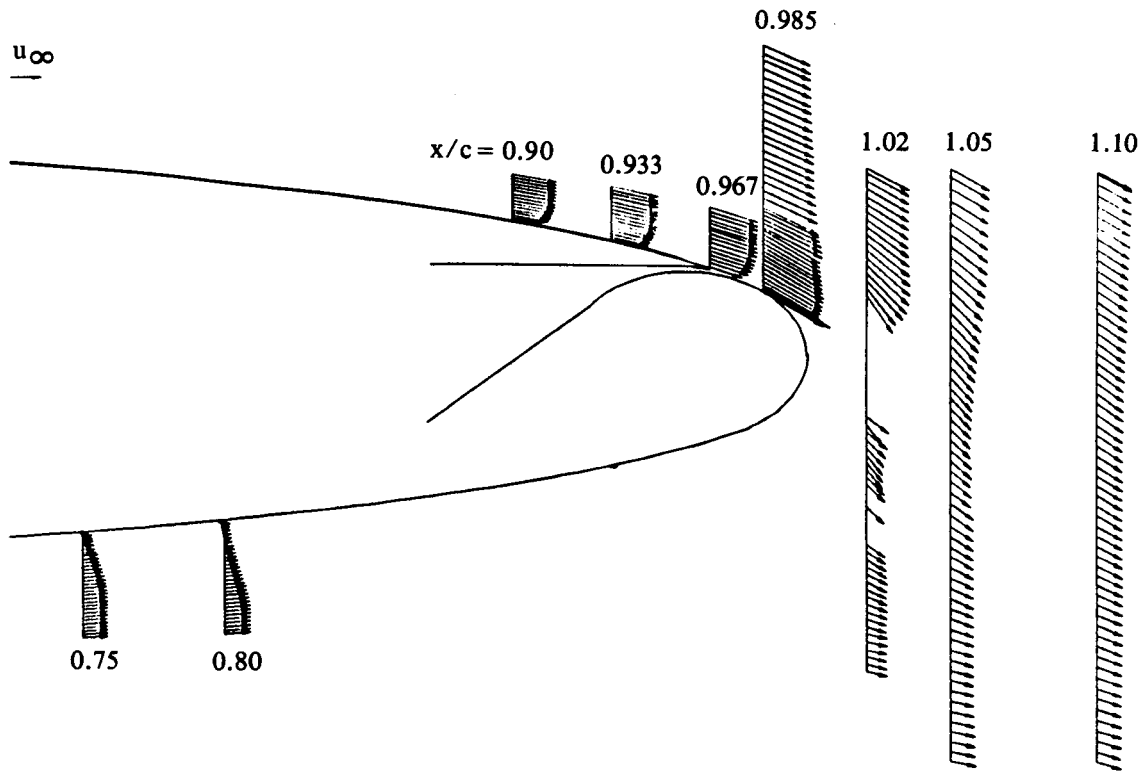

Figure 15. Velocity components in streamwise section plane; $M_\infty = 0.425$, $\alpha = 0°$, $p_j/p_\infty = 1.8$.

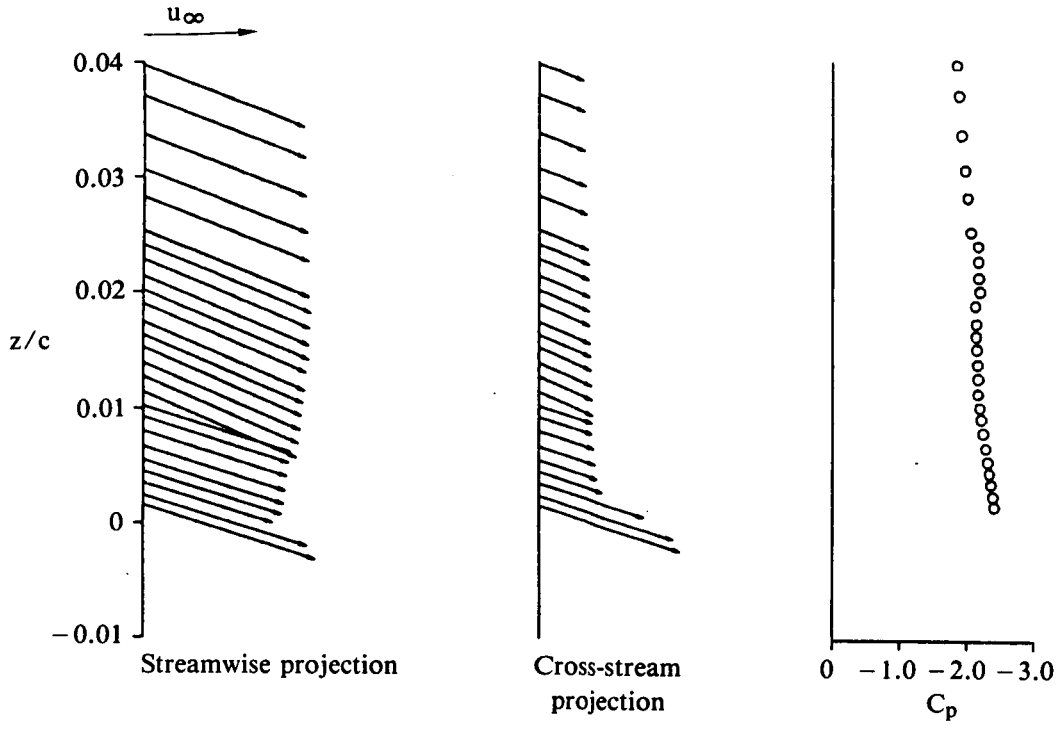

Figure 16. Wall-jet velocity and static-pressure profiles; $M_\infty = 0.425$, $\alpha = 0°$, $p_j/p_\infty = 1.8$, $x/c = 0.976$.

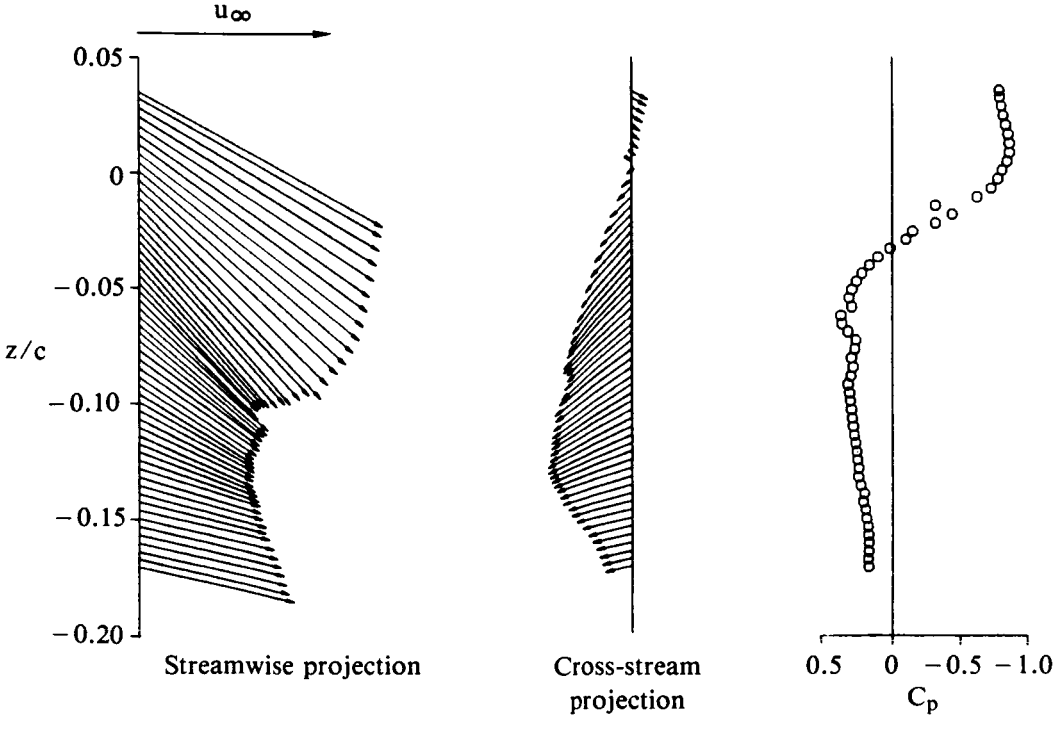

Figure 17. Wake velocity and static-pressure profiles; $M_\infty = 0.425$, $\alpha = 0°$, $p_j/p_\infty = 1.8$, $x/c = 1.05$.

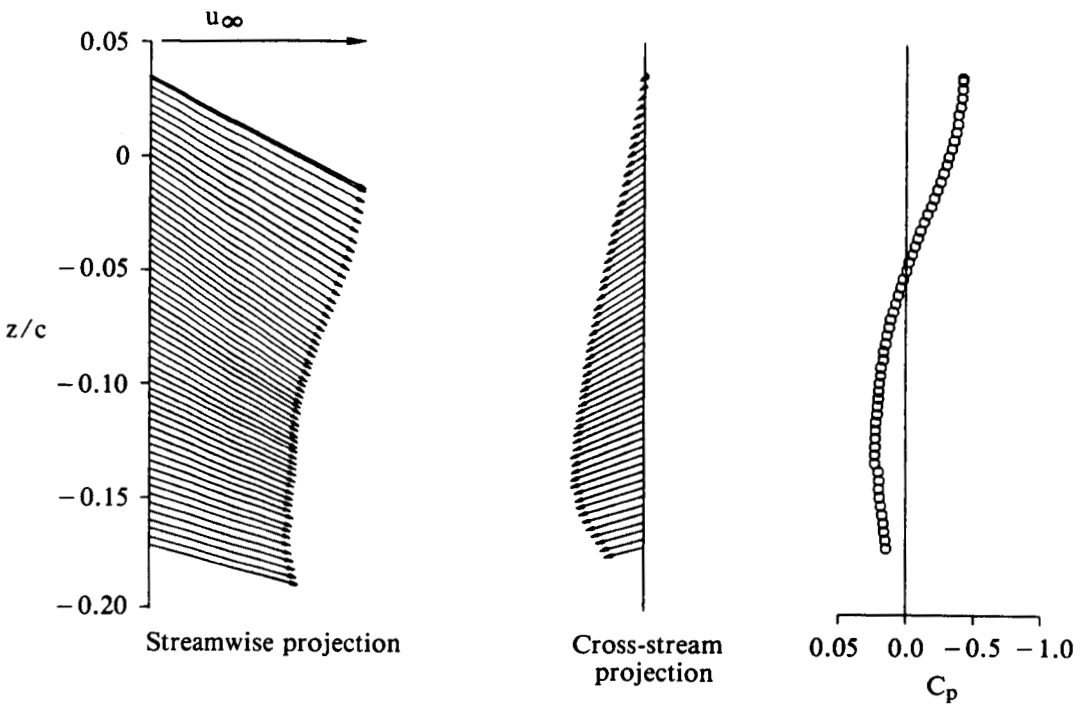

Figure 18. Wake velocity and static-pressure profiles; $M_\infty = 0.425$, $\alpha = 0°$, $p_j/p_\infty = 1.8$, $x/c = 1.10$.

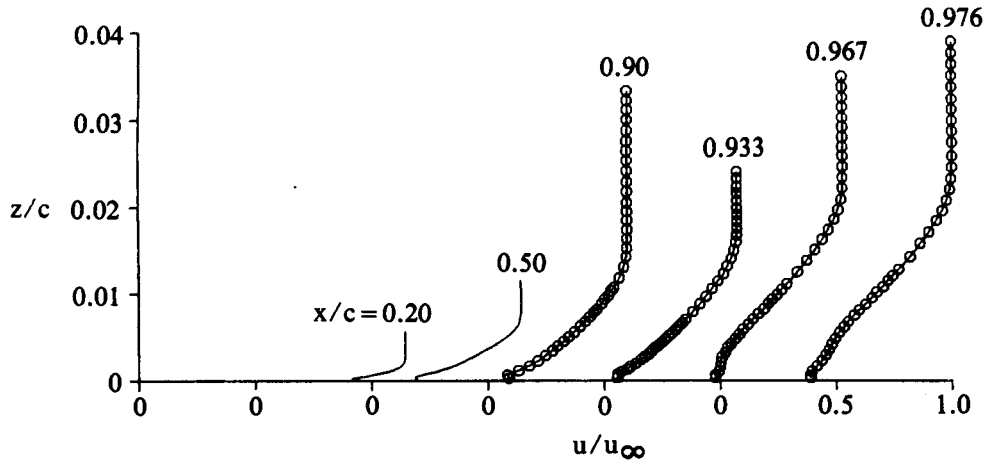

(a) Upper-surface velocity-magnitude profiles.

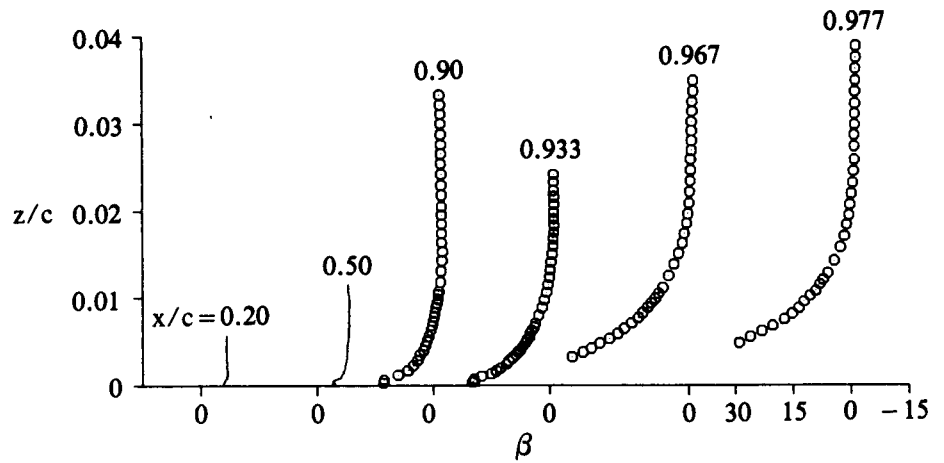

(b) Upper-surface yaw-plane flow-direction profiles.

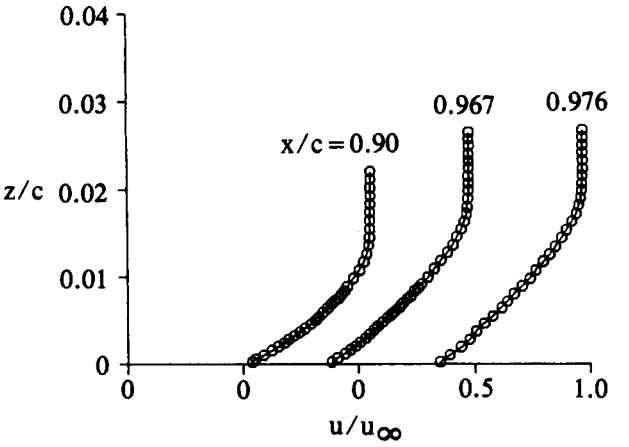

(c) Lower-surface velocity-magnitude profiles.

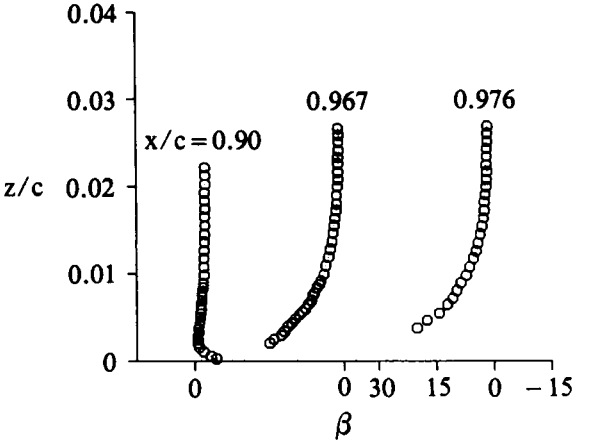

(d) Lower-surface yaw-plane flow-direction profiles.

Figure 19. Boundary-layer profiles; $M_\infty = 0.425$, $\alpha = 0°$, no blowing.

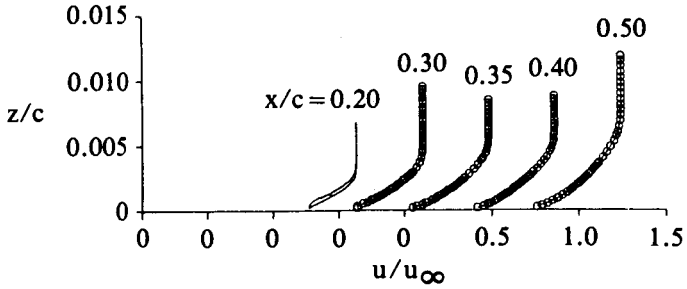

(a) Velocity magnitude profiles, forward locations

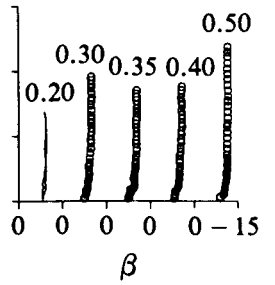

(b) Yaw-plane flow-direction profiles, forward locations

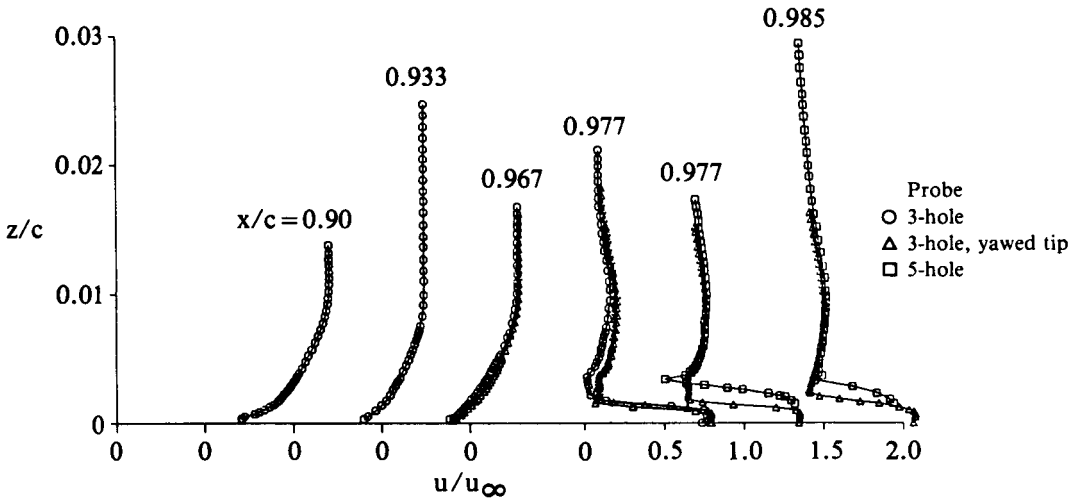

(c) Velocity magnitude profiles, aft locations

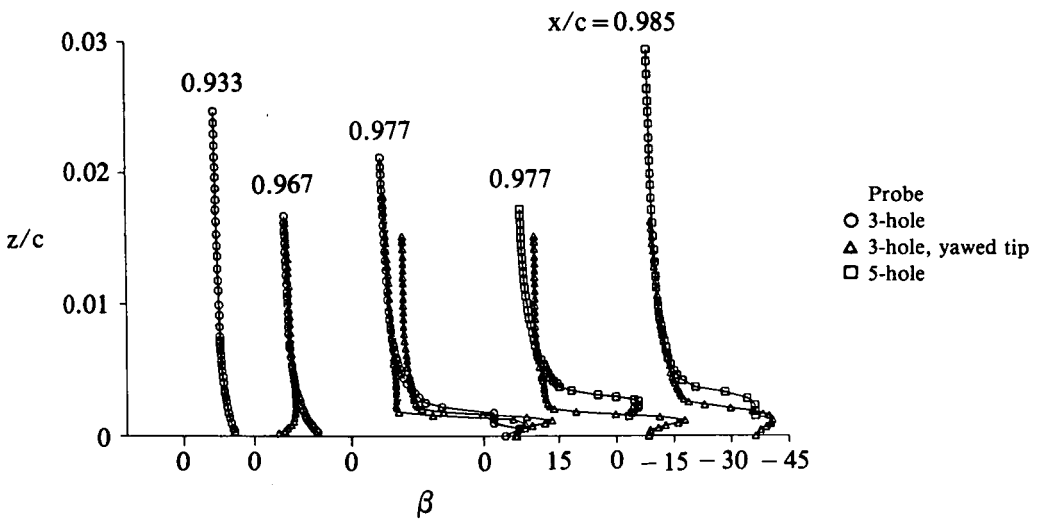

(d) Yaw-plane flow-direction profiles, aft locations

Figure 20. Boundary-layer and wake profiles; $M_\infty = 0.425$, $\alpha = 0°$, $p_j/p_\infty = 1.4$.

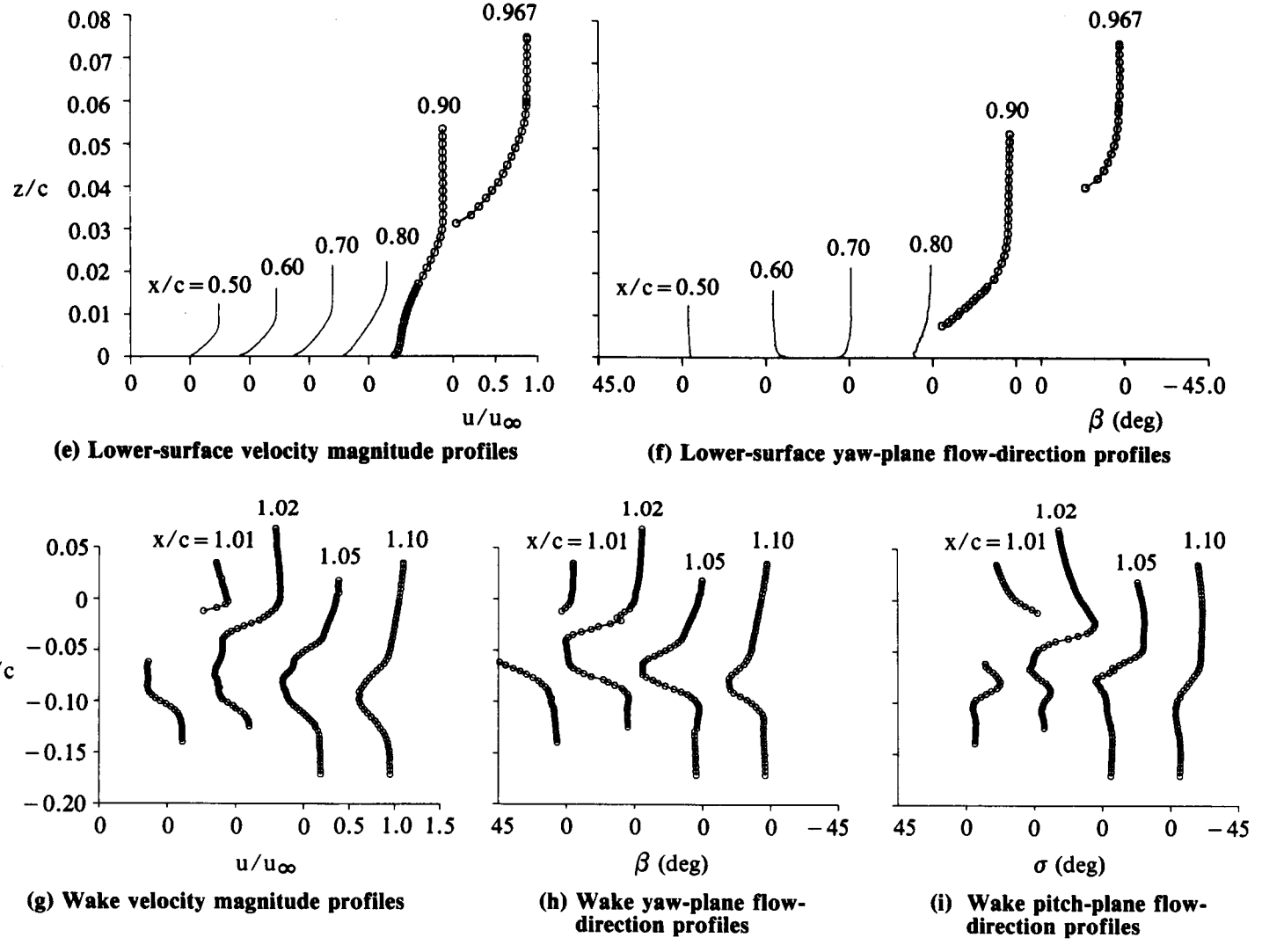

(e) Lower-surface velocity magnitude profiles

(f) Lower-surface yaw-plane flow-direction profiles

(g) Wake velocity magnitude profiles

(h) Wake yaw-plane flow-direction profiles

(i) Wake pitch-plane flow-direction profiles

Figure 20. (Cont.) Boundary-layer and wake profiles; $M_\infty = 0.425$, $\alpha = 0°$, $p_j/p_\infty = 1.4$.

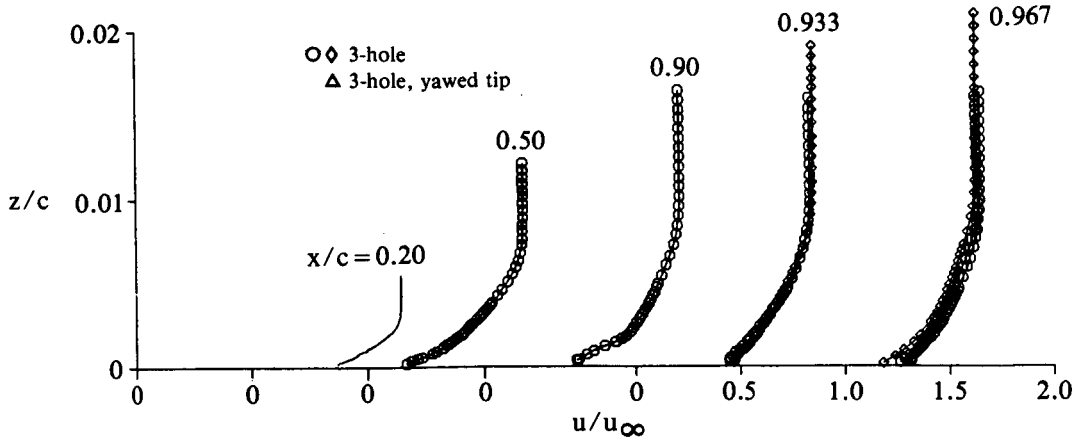

(a) Upper-surface velocity-magnitude profiles, forward locations

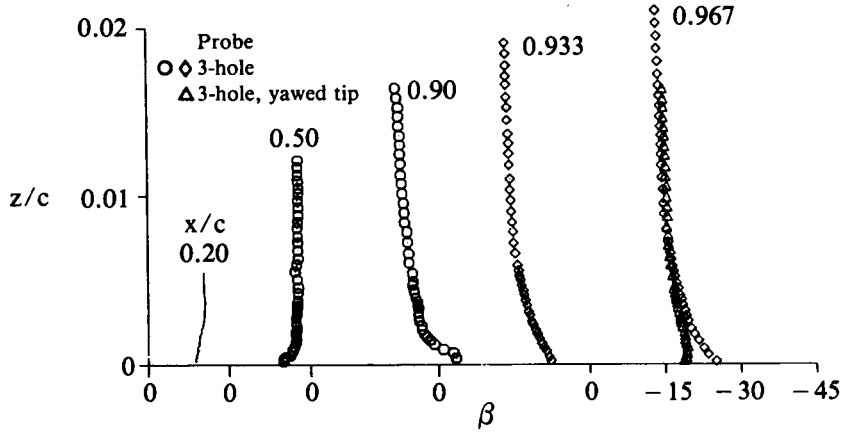

(b) Upper-surface yaw-plane flow-direction profiles, forward locations

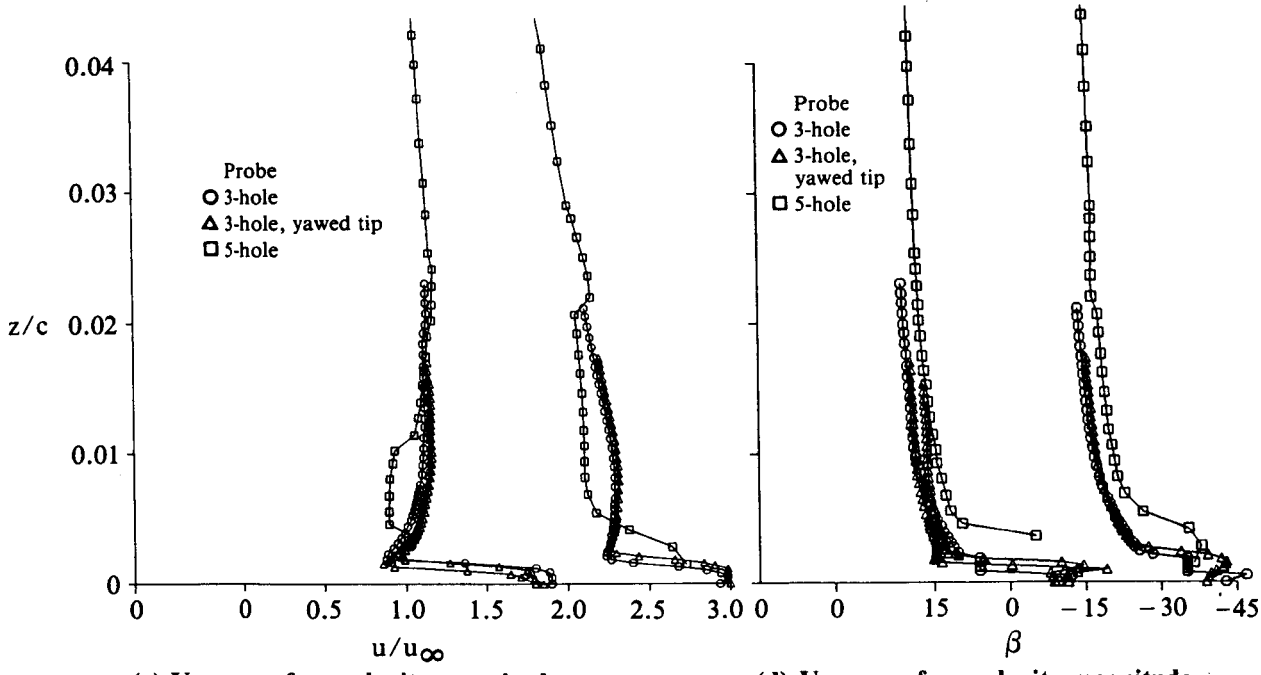

(c) Upper-surface velocity-magnitude profiles, wall jet

(d) Upper-surface velocity-magnitude profiles, wall jet

Figure 21. Boundary-layer and wake profiles; $M_\infty = 0.425$, $\alpha = 0°$, $p_j/p_\infty = 1.8$.

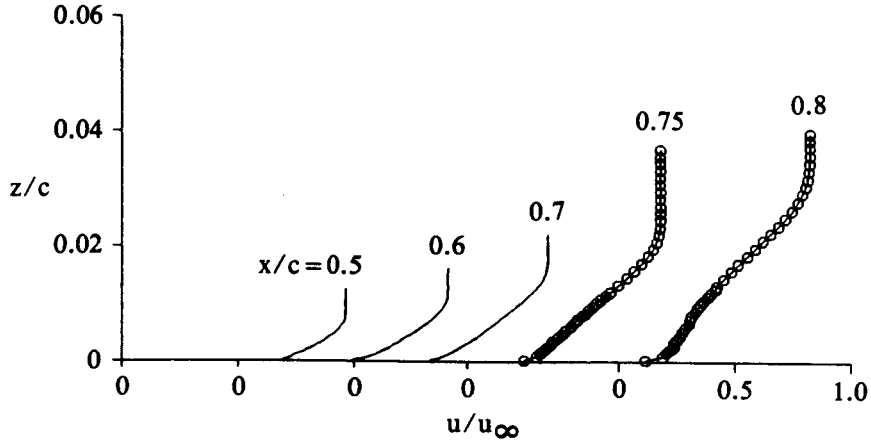

(e) Lower-surface velocity-magnitude profiles

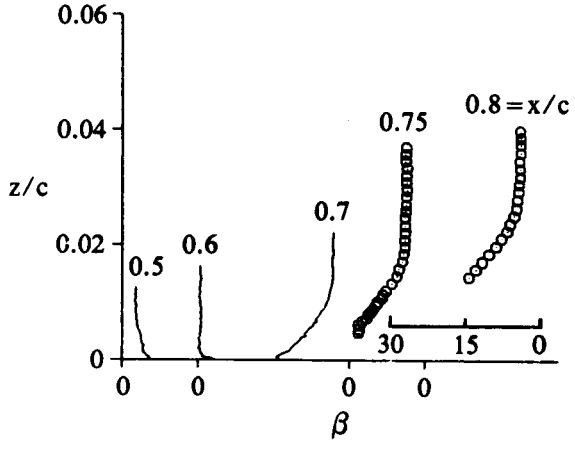

(f) Lower-surface yaw-plane flow-direction profiles

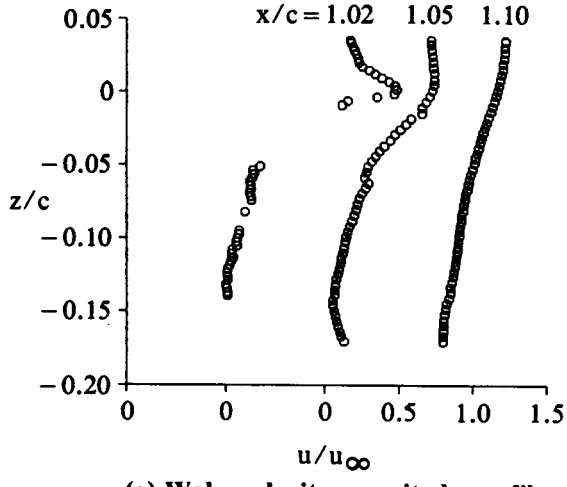

(g) Wake velocity-magnitude profiles

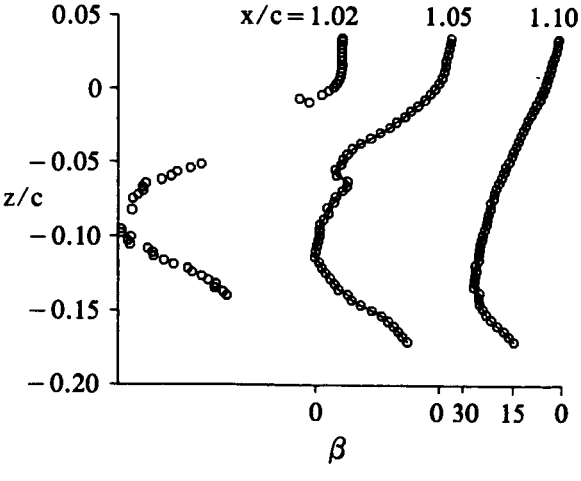

(h) Wake yaw-plane flow-direction profiles

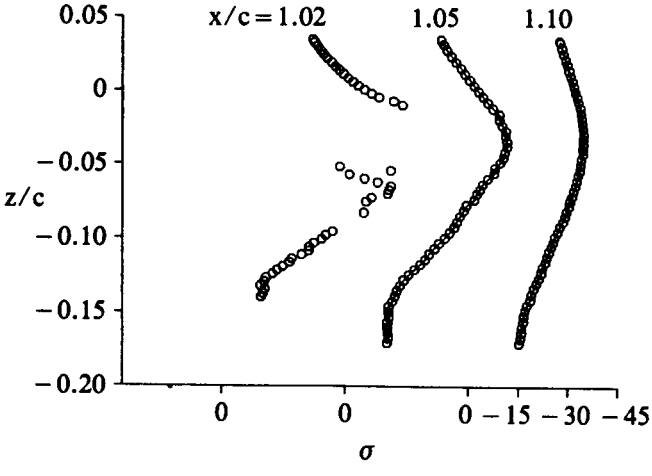

(i) Wake pitch-plane flow-direction profiles

Figure 21. (Cont.) Boundary-layer and wake profiles; $M_\infty = 0.425$, $\alpha = 0°$, $p_j/p_\infty = 1.8$.

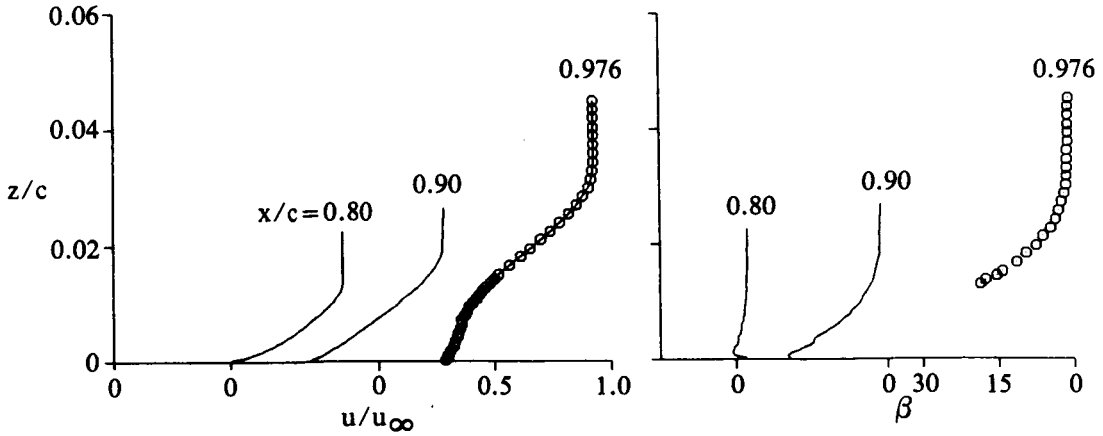

(a) Velocity magnitude profiles, $p_j/p_\infty = 1.2$ (b) Yaw-plane flow-direction profiles, $p_j/p_\infty = 1.2$

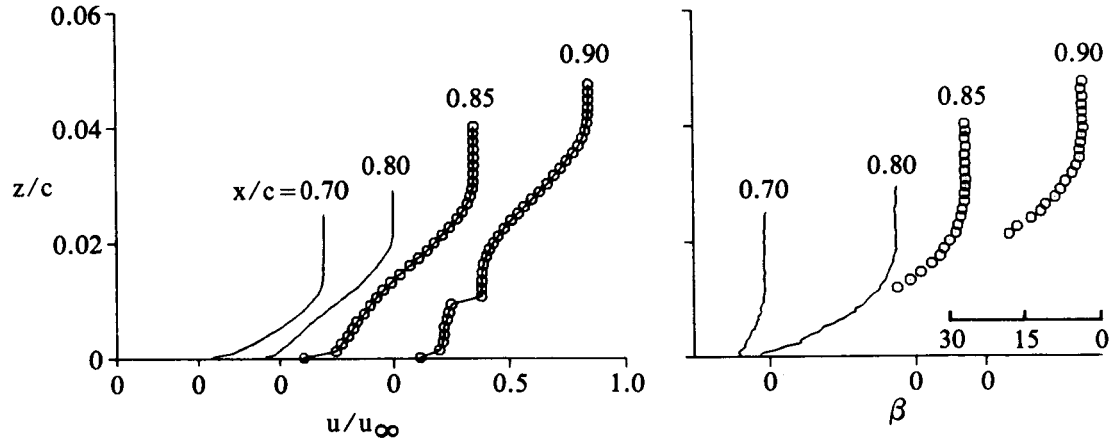

(c) Velocity magnitude profiles, $p_j/p_\infty = 1.6$ (d) Yaw-plane flow direction profiles, $p_j/p_\infty = 1.6$

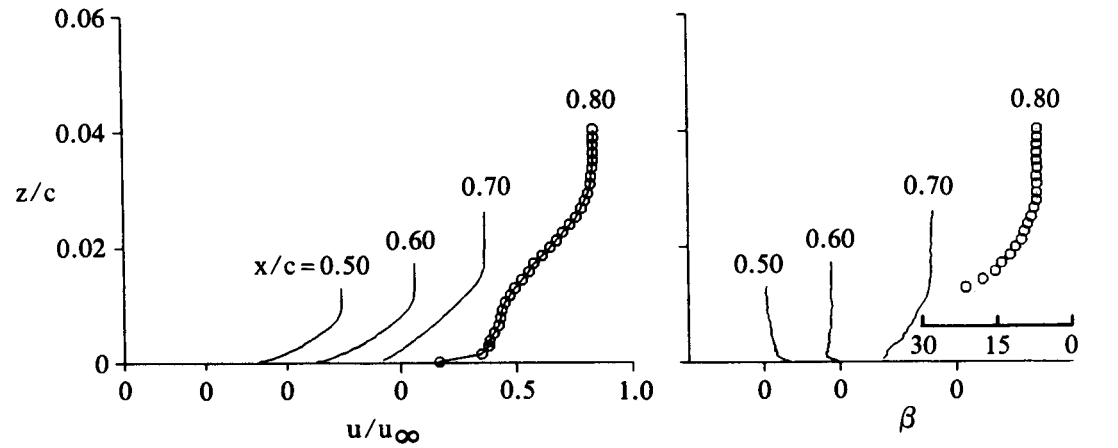

(e) Velocity magnitude profiles, $p_j/p_\infty = 2.2$ (f) Yaw-plane flow-direction profiles, $p_j/p_\infty = 2.2$

Figure 22. Lower-surface boundary-layer profiles; $M_\infty = 0.425$, $\alpha = 0°$.

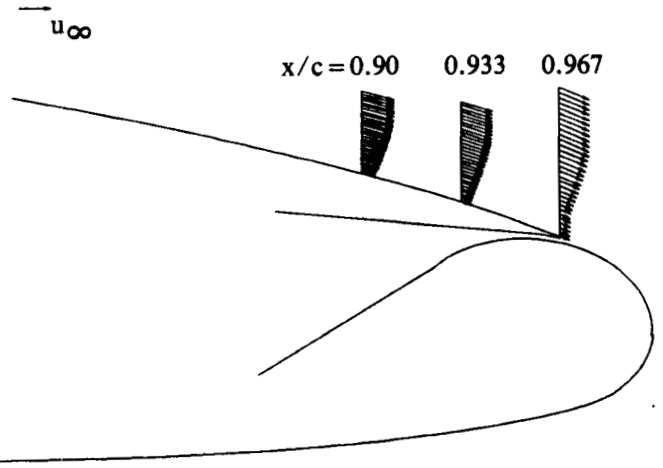

Figure 23. Velocity components in streamwise section plane; $M_\infty = 0.425$, $\alpha = 5°$, no blowing.

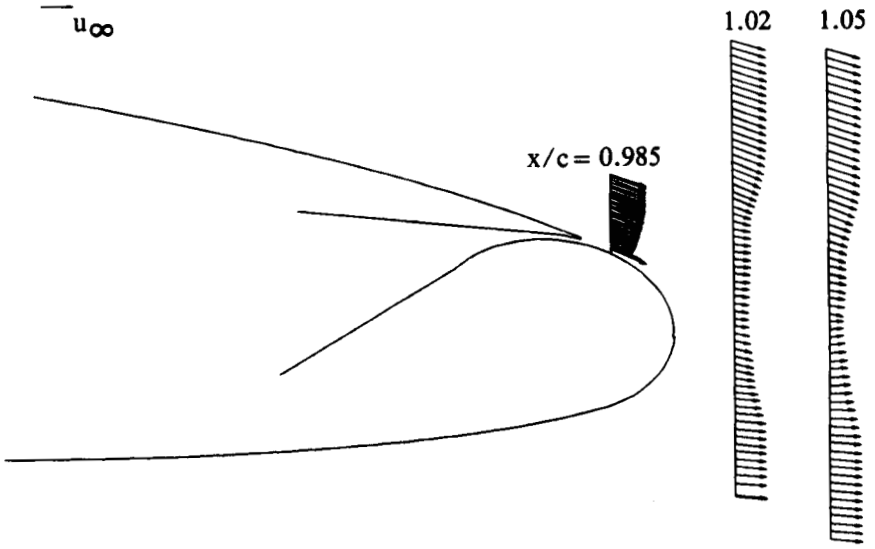

Figure 25. Velocity components in streamwise section plane; $M_\infty = 0.425$, $\alpha = 5°$, $p_j/p_\infty = 1.4$.

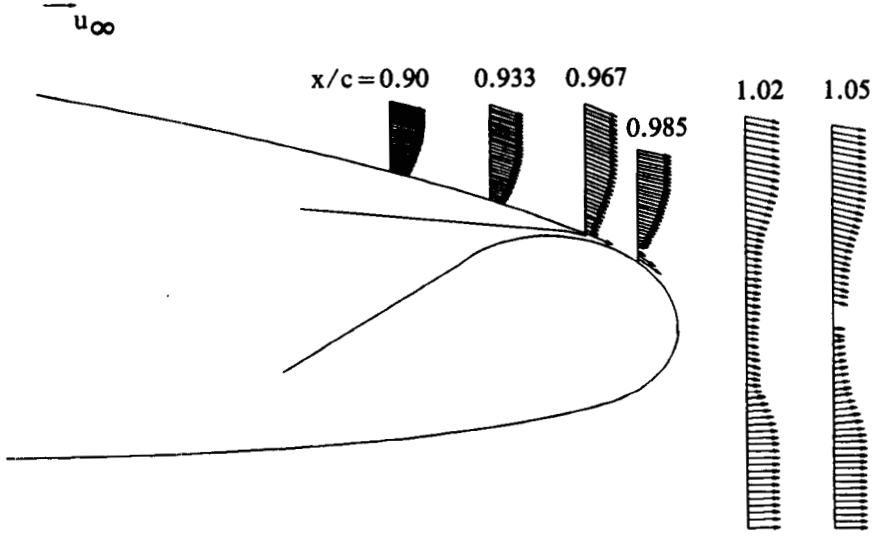

Figure 24. Velocity components in streamwise section plane; $M_\infty = 0.425$, $\alpha = 5°$, $p_j/p_\infty = 1.2$.

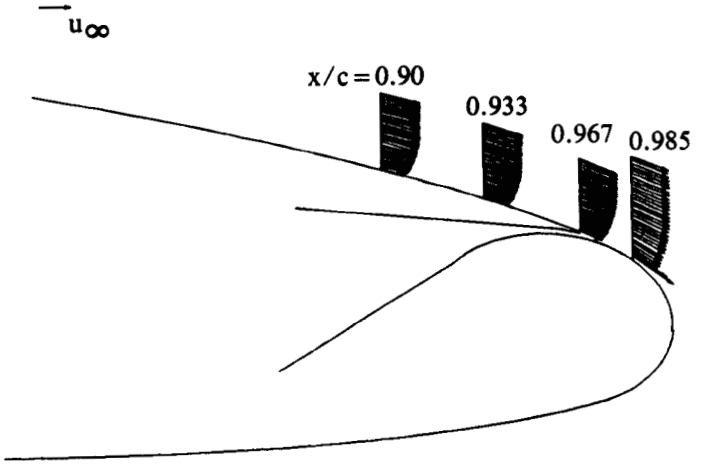

Figure 26. Velocity components in streamwise section plane; $M_\infty = 0.425$, $\alpha = 5°$, $p_j/p_\infty = 1.6$.

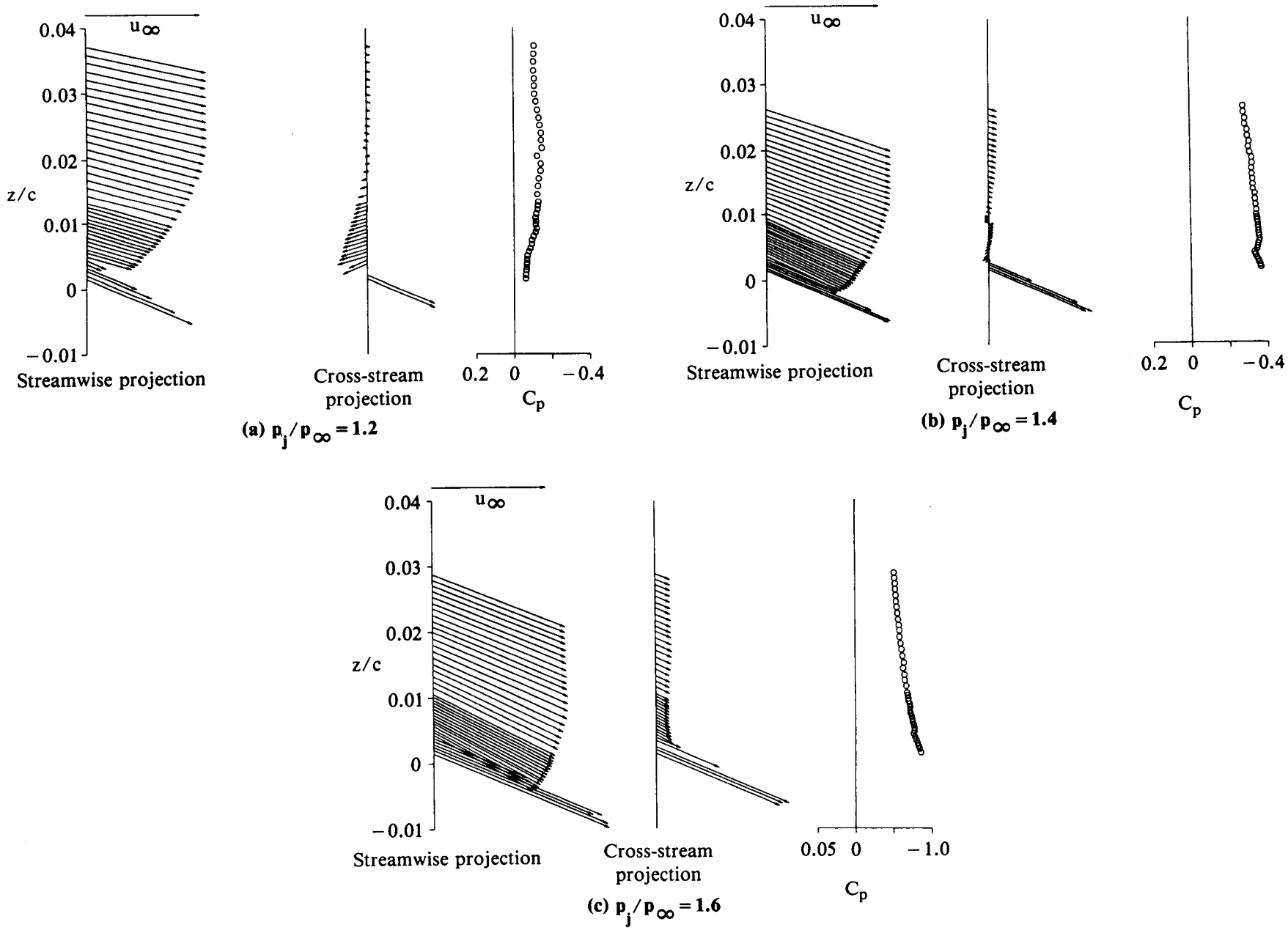

Figure 27. Wall-jet velocity and static-pressure profiles; $M_\infty = 0.425$, $\alpha = 5°$, $x/c = 0.977$.

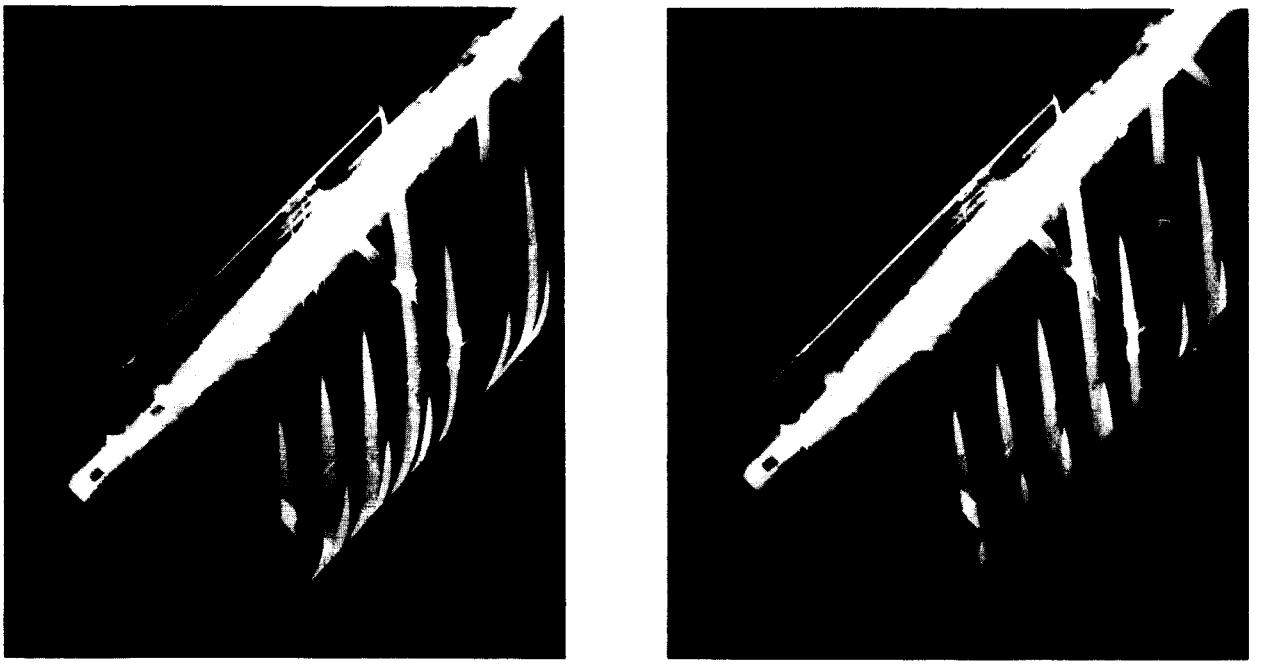

(a) $p_j/p_\infty = 1.2$ (b) $p_j/p_\infty = 1.3$

Figure 28. Fluorescent oil-flow photographs of wing upper surface; $M_\infty = 0.425$, $\alpha = 5°$.

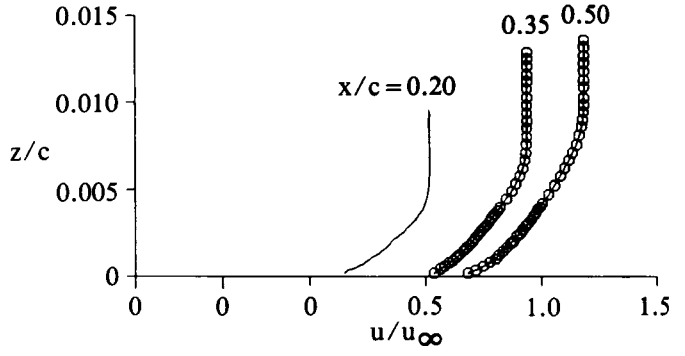

(a) Velocity magnitude profiles, forward locations

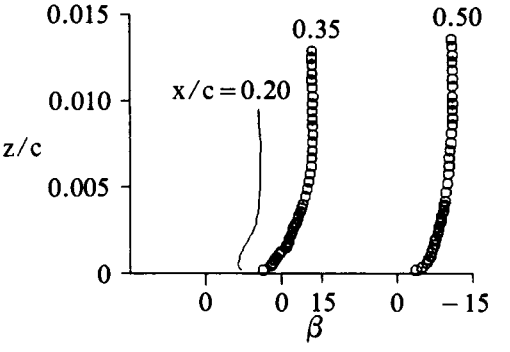

(b) Yaw-plane flow-direction profiles, forward locations

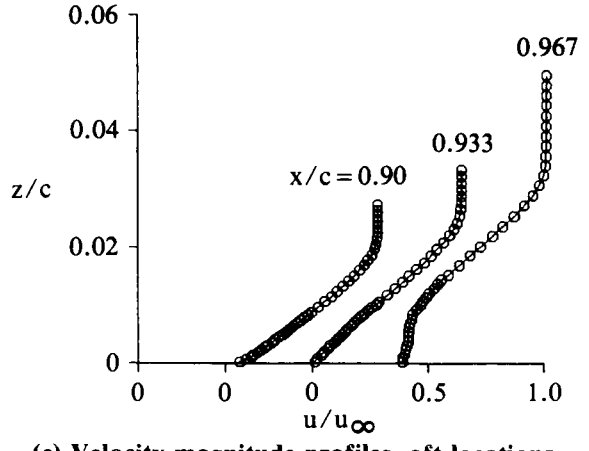

(c) Velocity magnitude profiles, aft locations

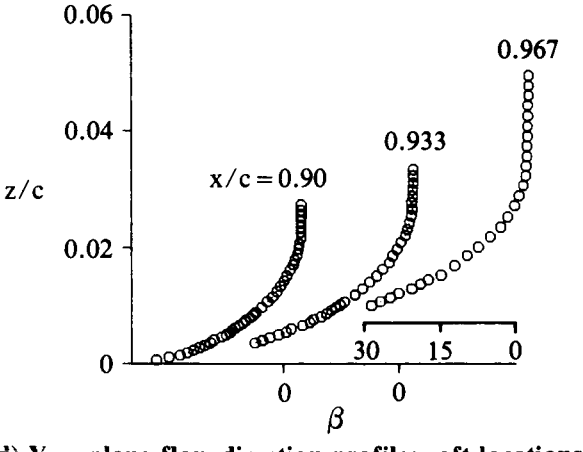

(d) Yaw-plane flow-direction profiles, aft locations

Figure 29. Upper-surface boundary layer profiles; $M_\infty = 0.425$, $\alpha = 5°$, no blowing.

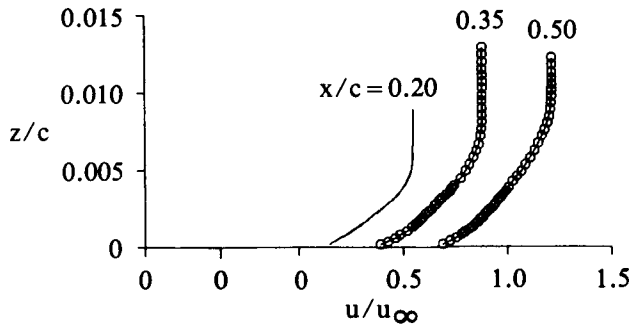

(a) Upper-surface velocity-magnitude profiles, forward locations

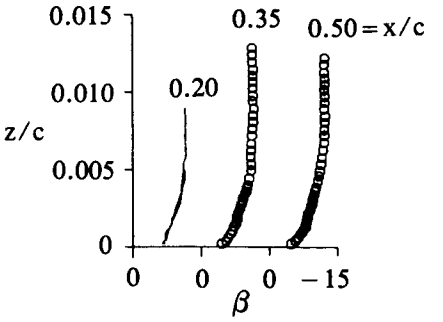

(b) Upper-surface yaw-plane flow-direction profiles, forward locations

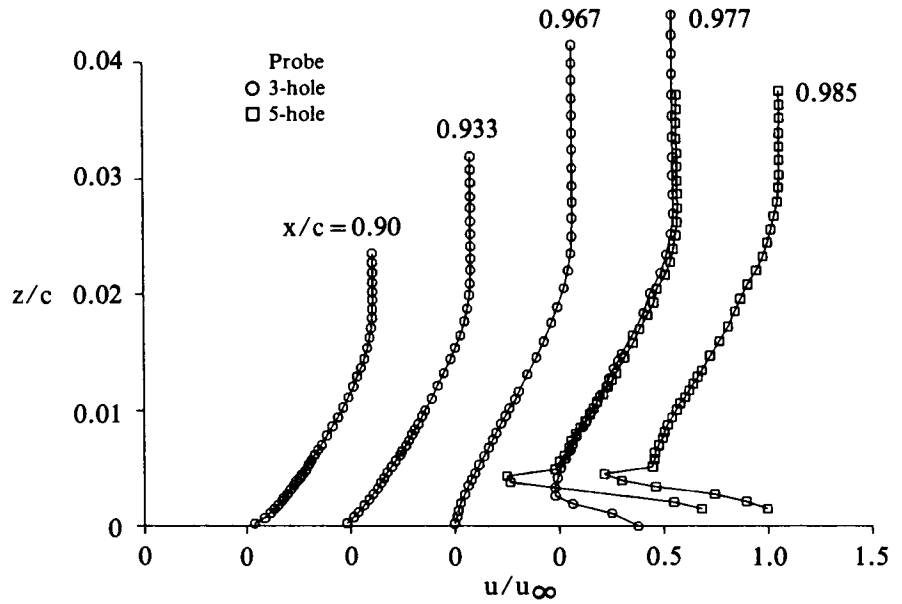

(c) Upper-surface velocity-magnitude profiles, aft locations

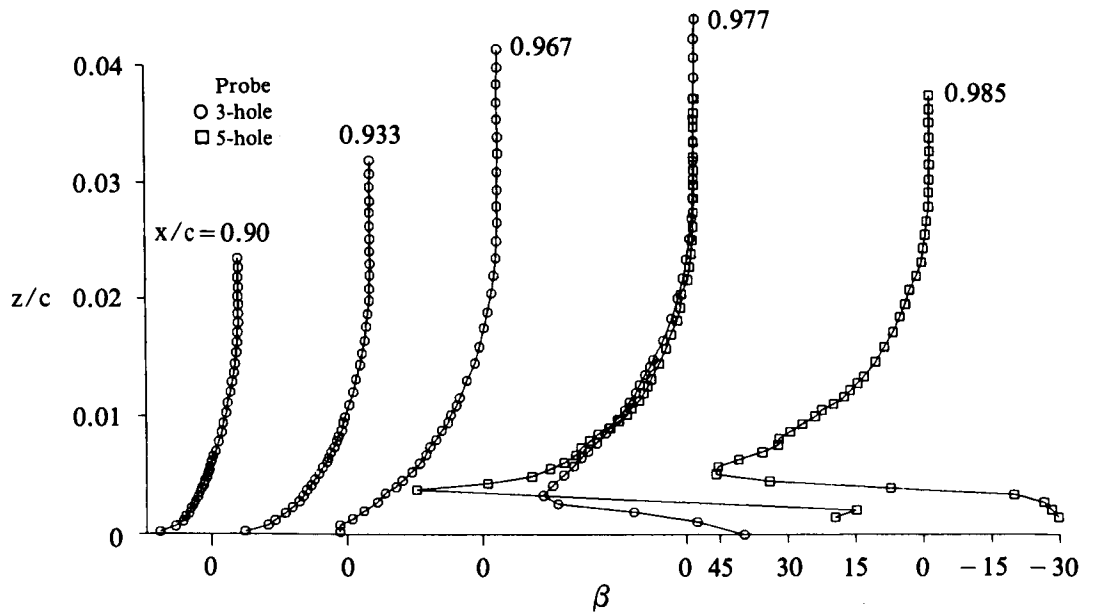

(d) Upper-surface yaw-plane flow-direction profiles, aft locations

Figure 30. Boundary-layer and wake profiles; $M_\infty = 0.425$, $\alpha = 5°$, $p_j/p_\infty = 1.2$.

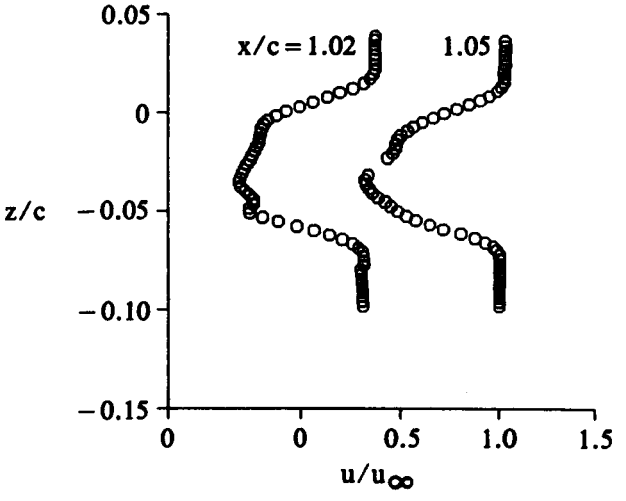

(e) Wake velocity magnitude profiles

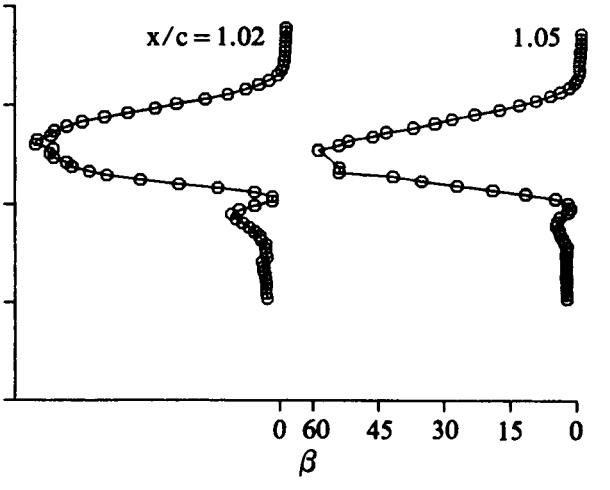

(f) Wake yaw-plane flow-direction profiles

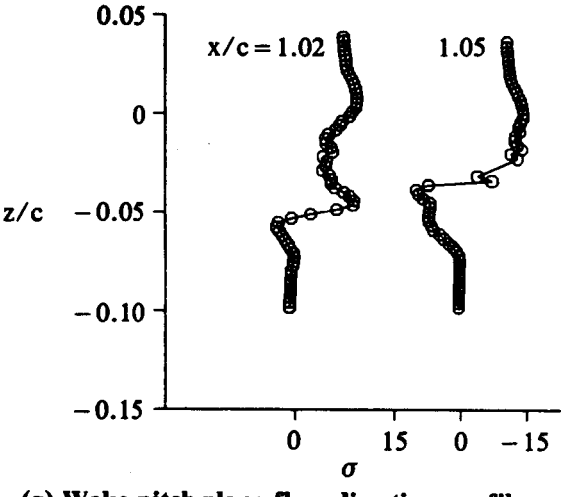

(g) Wake pitch-plane flow-direction profiles

Figure 30. (Cont.) Boundary-layer and wake profiles; $M_\infty = 0.425$, $\alpha = 5°$, $p_j/p_\infty = 1.2$.

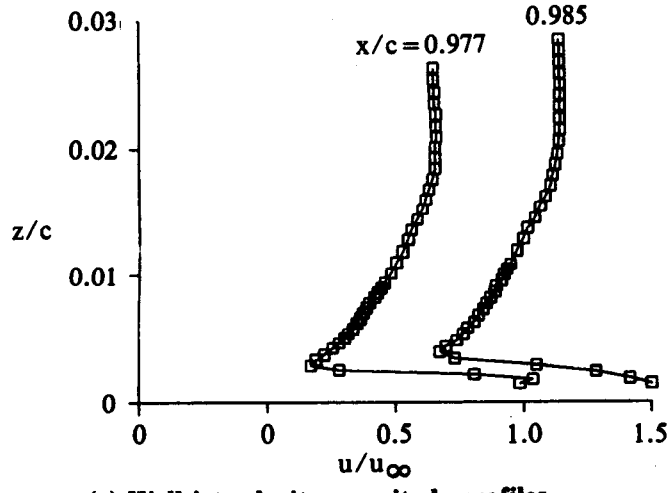

(a) Wall-jet velocity magnitude profiles

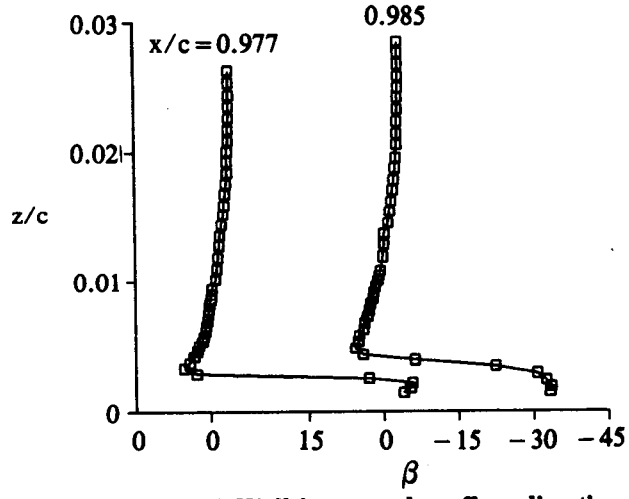

(b) Wall-jet yaw-plane flow direction profiles

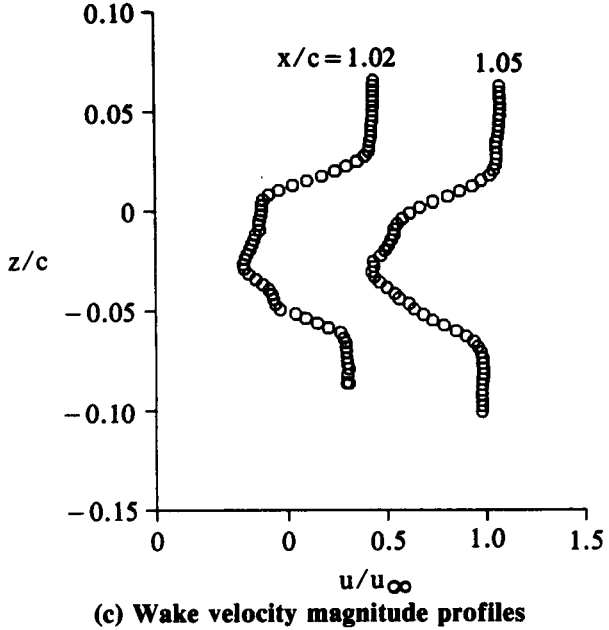

(c) Wake velocity magnitude profiles

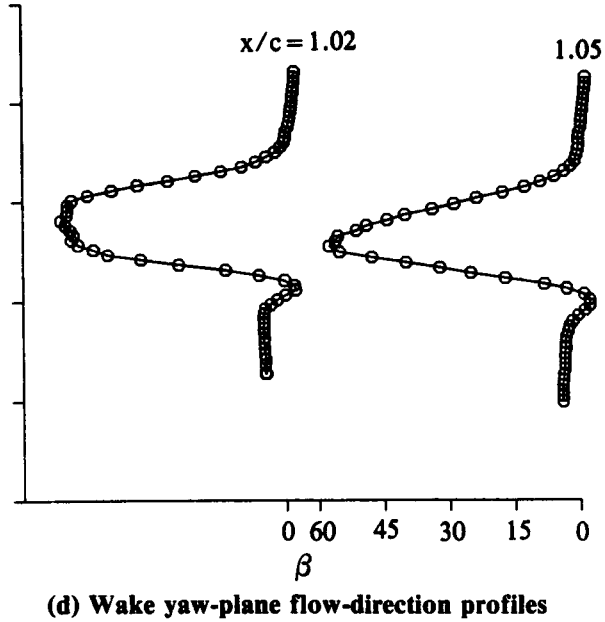

(d) Wake yaw-plane flow-direction profiles

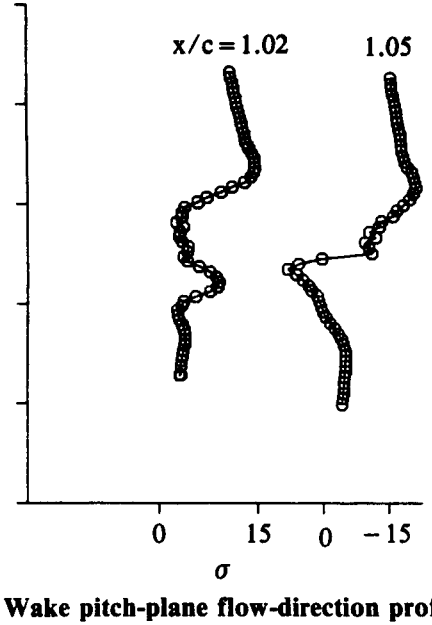

(e) Wake pitch-plane flow-direction profiles

Figure 31. Boundary-layer and wake profiles; $M_\infty = 0.425$, $\alpha = 5°$, $p_j/p_\infty = 1.4$.

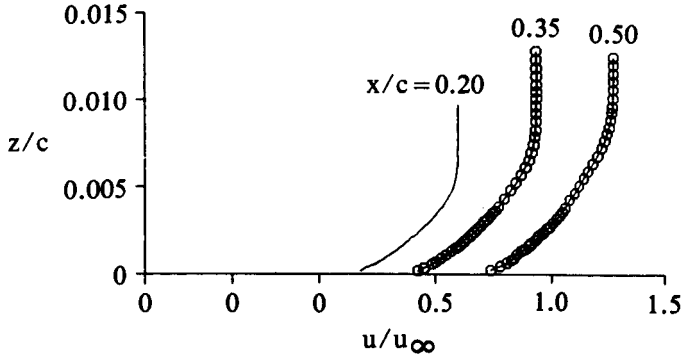

(a) Velocity-magnitude profiles, forward locations

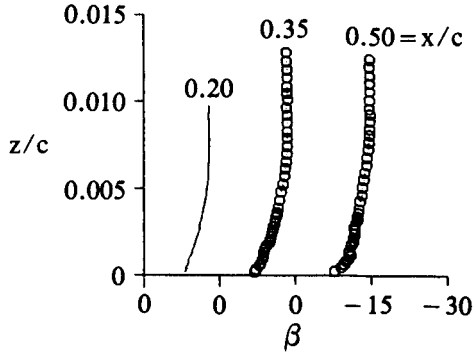

(b) Yaw-plane flow direction profiles, forward locations

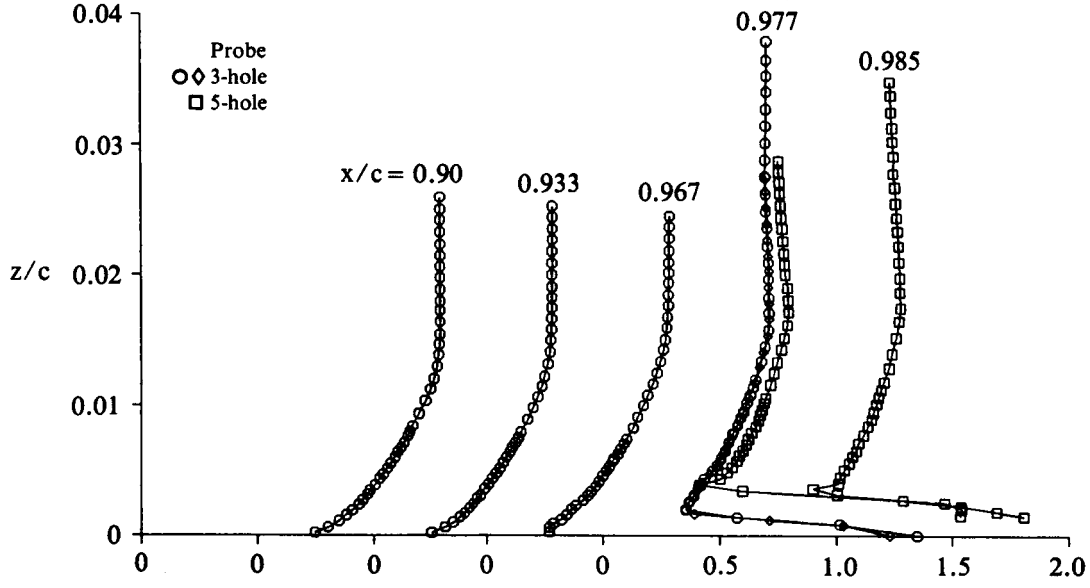

(c) Velocity-magnitude profiles, aft locations

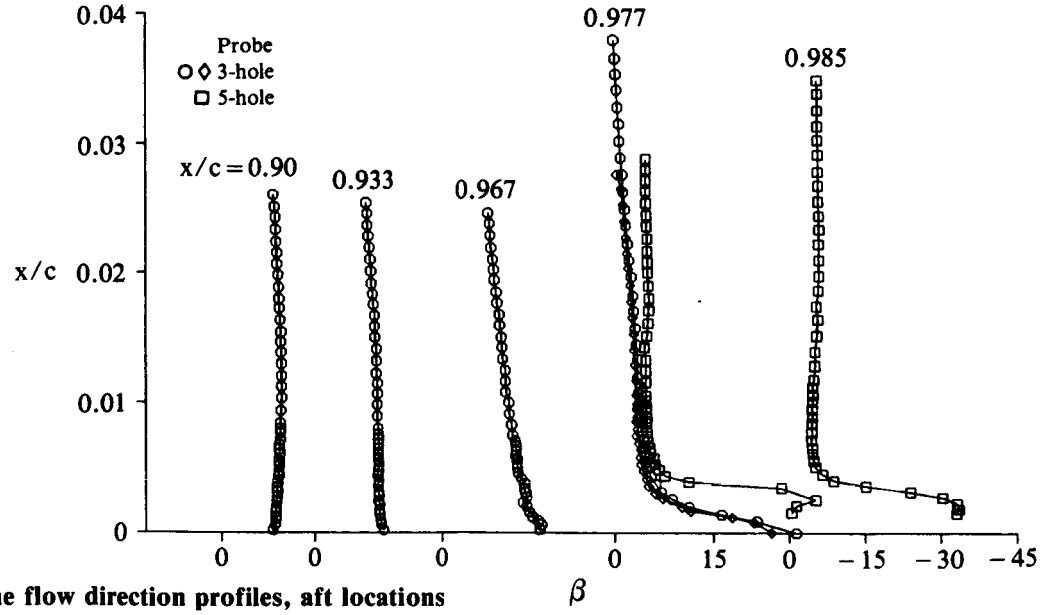

(d) Yaw-plane flow direction profiles, aft locations

Figure 32. Boundary-layer profiles; $M_\infty = 0.425$, $\alpha = 5°$, $p_j/p_\infty = 1.6$.

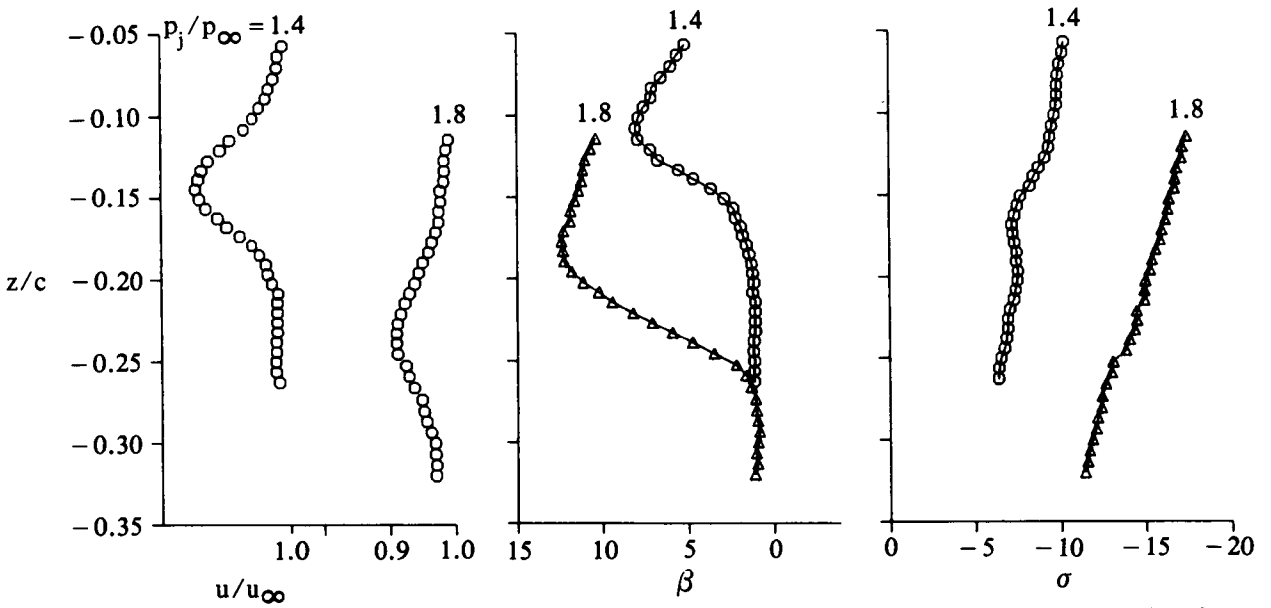

(a) Velocity magnitude profiles **(b) Yaw-plane flow direction profiles** **(c) Pitch-plane flow direction profiles**

Figure 33. Wake profiles; $M_\infty = 0.425$, $\alpha = 5°$, $x/c = 1.3$.

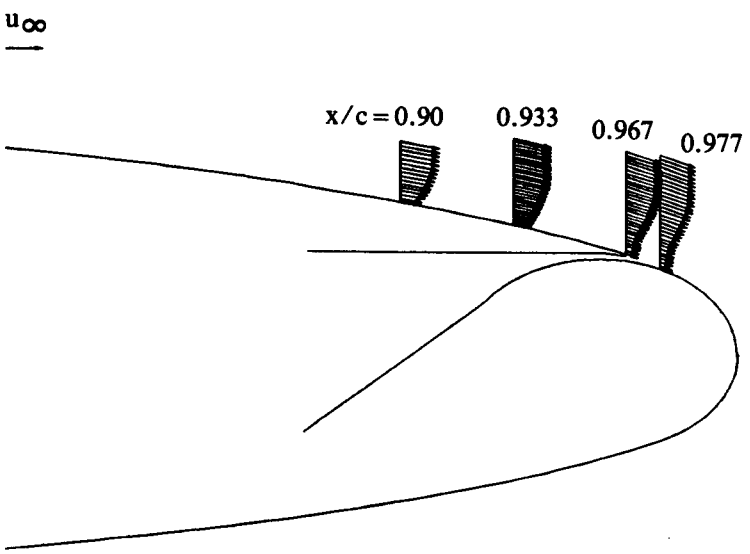

Figure 34. Velocity components in streamwise section plane; $M_\infty = 0.7$, $\alpha = 0°$, no blowing.

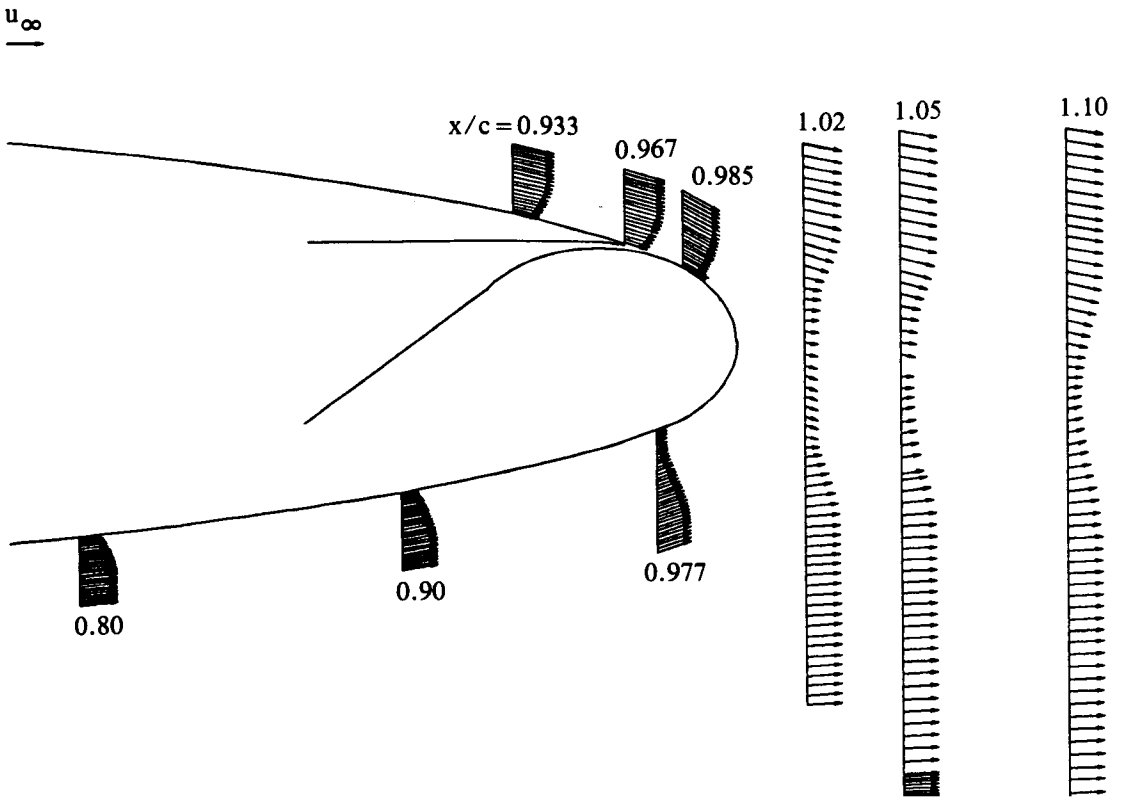

Figure 35. Velocity components in streamwise section plane; $M_\infty = 0.70$, $\alpha = 0°$, $p_j/p_\infty = 1.4$.

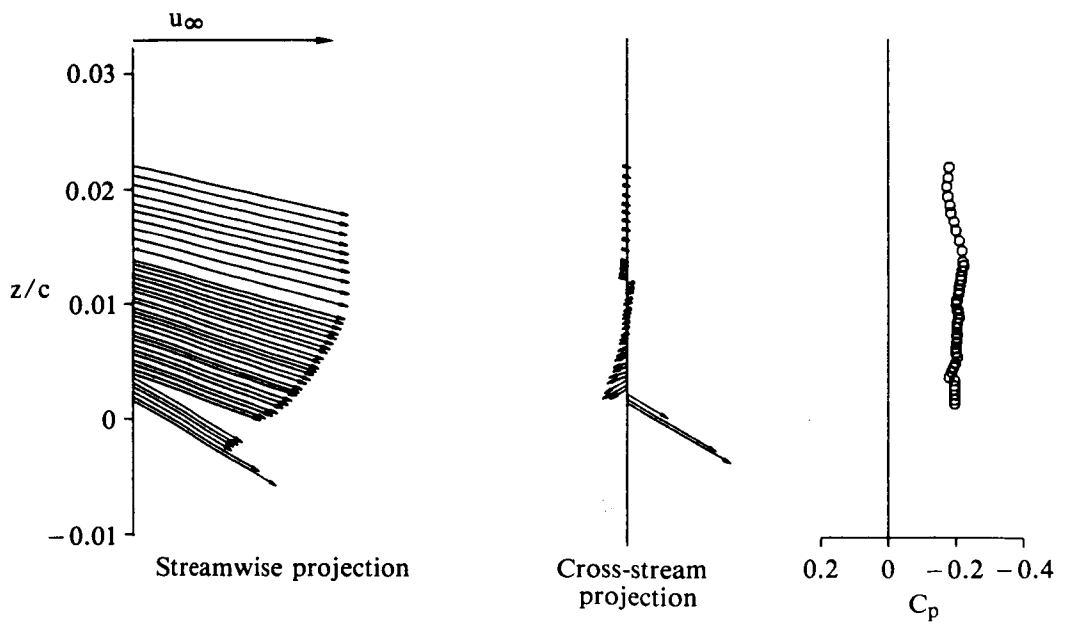

Figure 36. Wall-jet velocity and static-pressure profiles; $M_\infty = 0.70$, $\alpha = 0°$, $p_j/p_\infty = 1.4$, $x/c = 0.985$.

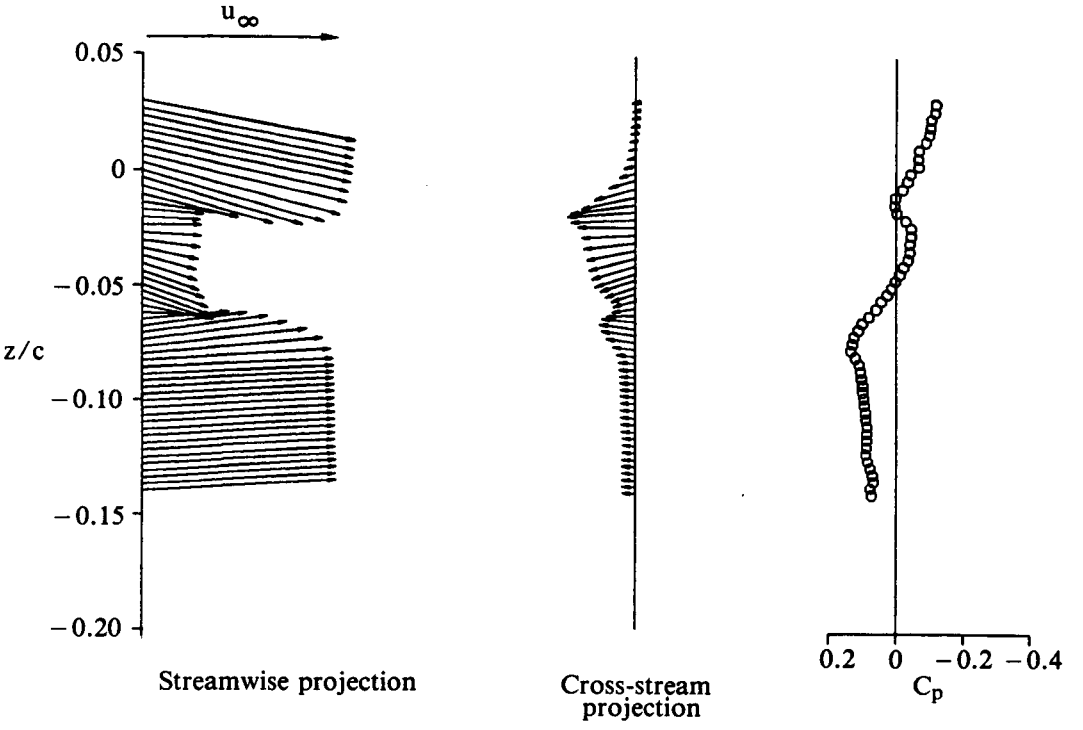

Figure 37. Wake velocity and static-pressure profiles; $M_\infty = 0.70$, $\alpha = 0°$, $p_j/p_\infty = 1.4$, $x/c = 1.02$.

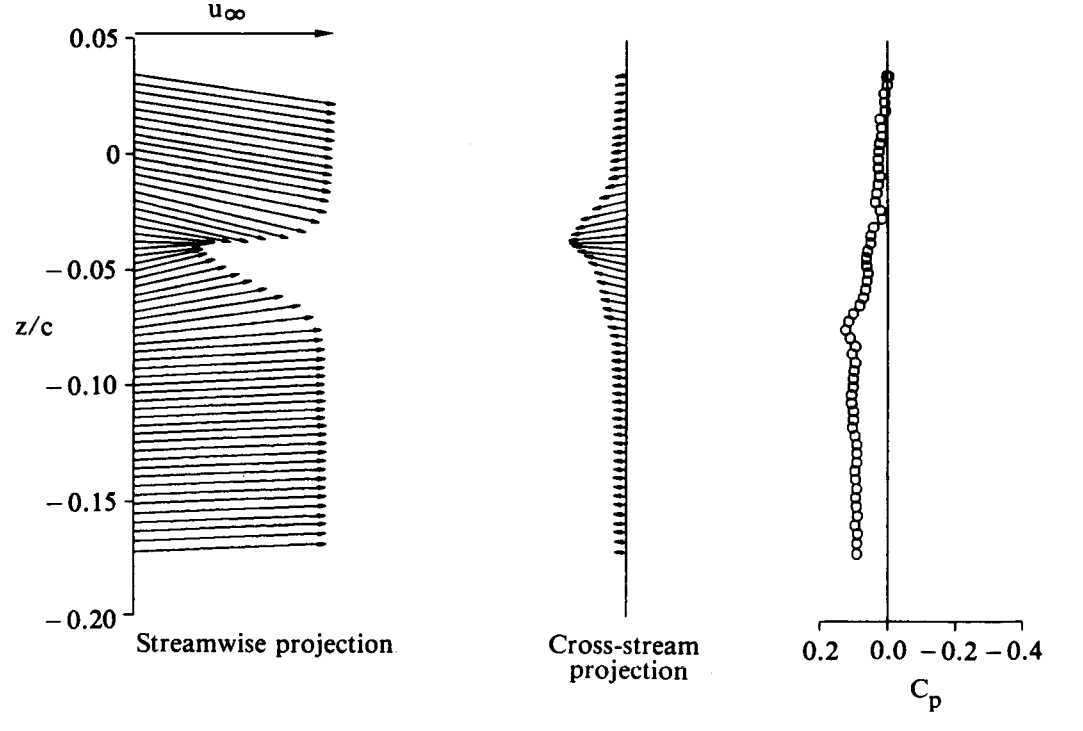

Figure 38. Wake velocity and static-pressure profiles; $M_\infty = 0.70$, $\alpha = 0°$, $p_j/p_\infty = 1.4$, $x/c = 1.1$.

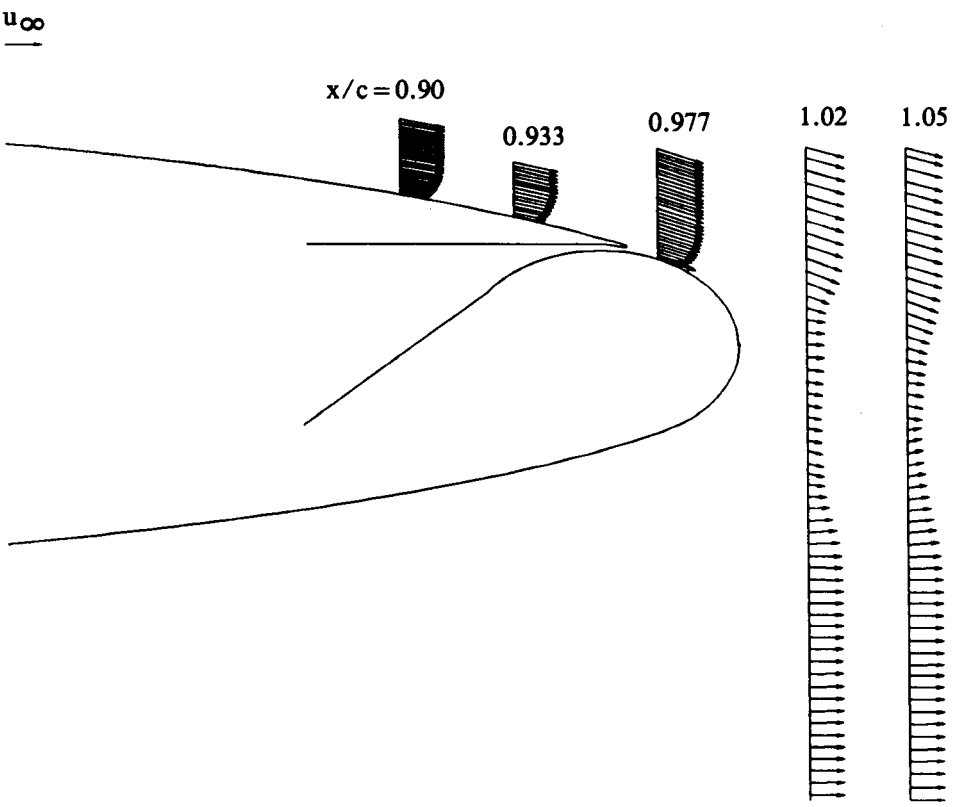

Figure 39. Velocity vectors in streamwise section plane; $M_\infty = 0.70$, $\alpha = 0°$, $p_j/p_\infty = 1.8$.

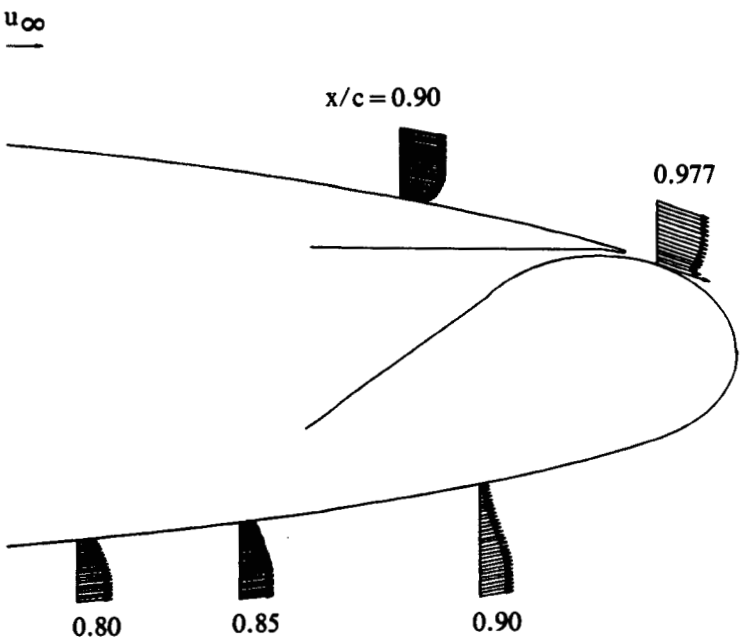

Figure 40. Velocity vectors in streamwise section plane; $M_\infty = 0.70$, $\alpha = 0°$, $p_j/p_\infty = 2.2$.

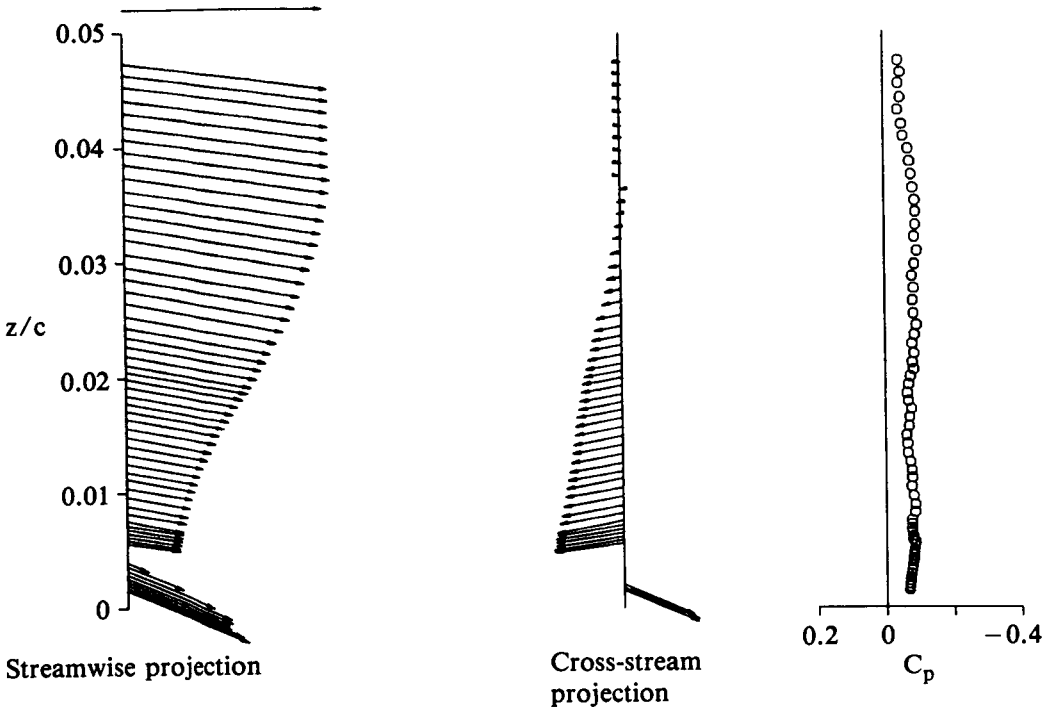

(a) $p_j/p_\infty = 1.2$

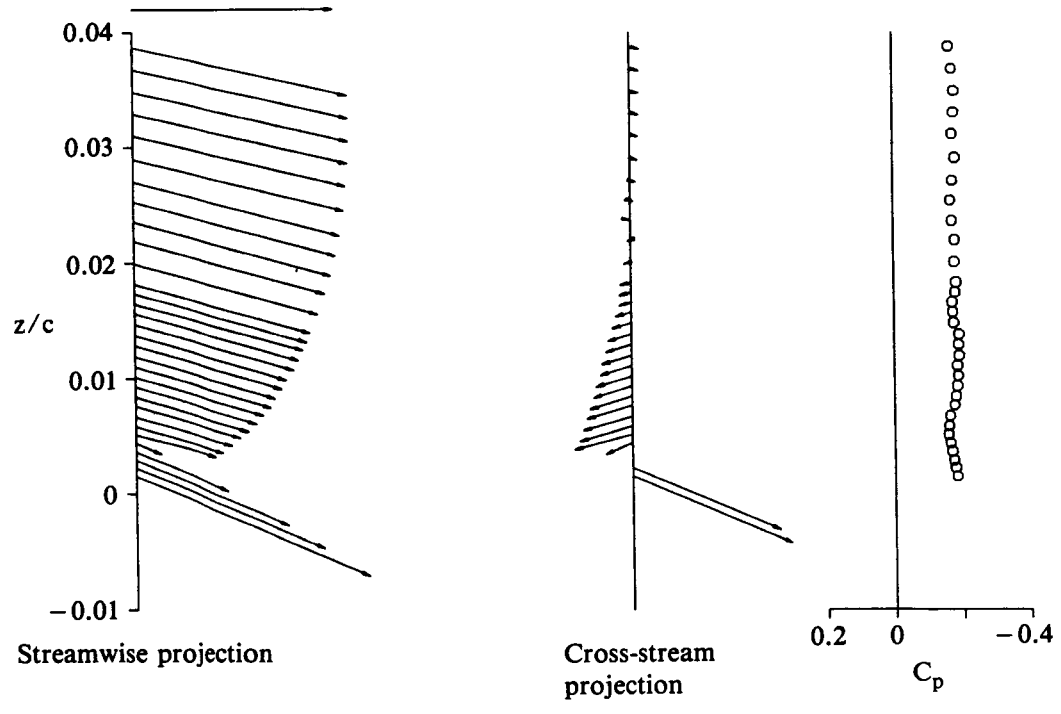

(b) $p_j/p_\infty = 2.2$

Figure 41. Wall-jet velocity and static-pressure profiles; $M_\infty = 0.70$, $\alpha = 5°$, $x/c = 0.977$.

Figure 42. Fluorescent oil-flow photograph; $M_\infty = 0.7$, $\alpha = 5°$, $p_j / p_\infty = 2.0$.

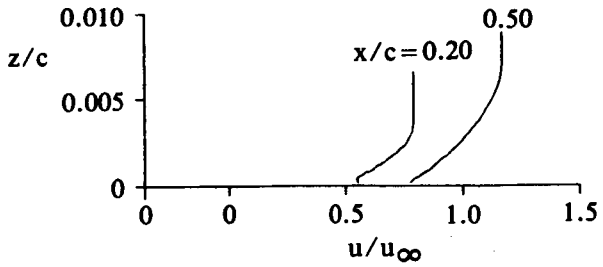

(a) Velocity-magnitude profiles; forward locations

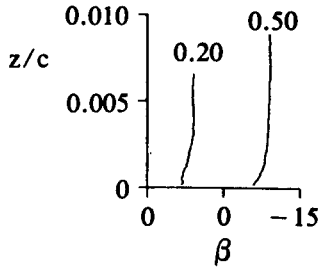

(b) Yaw-plane flow-direction profiles, forward locations

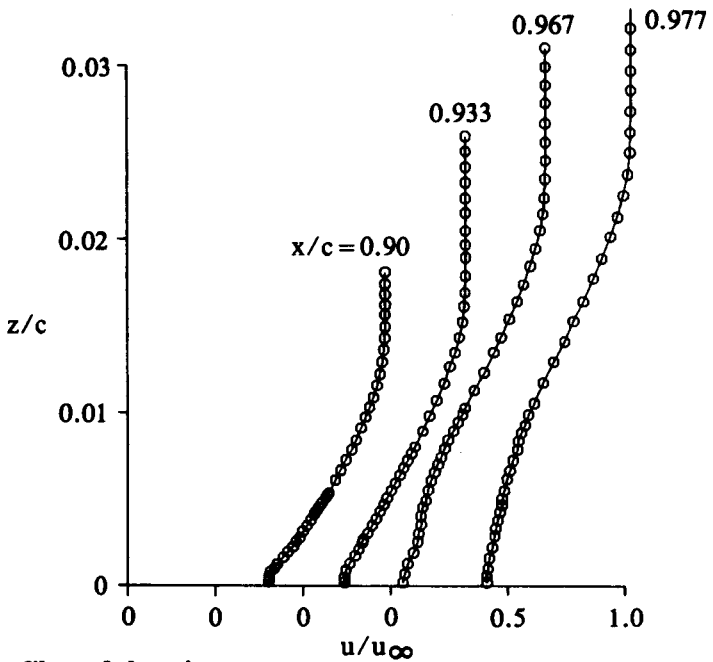

(c) Velocity-magnitude profiles, aft locations

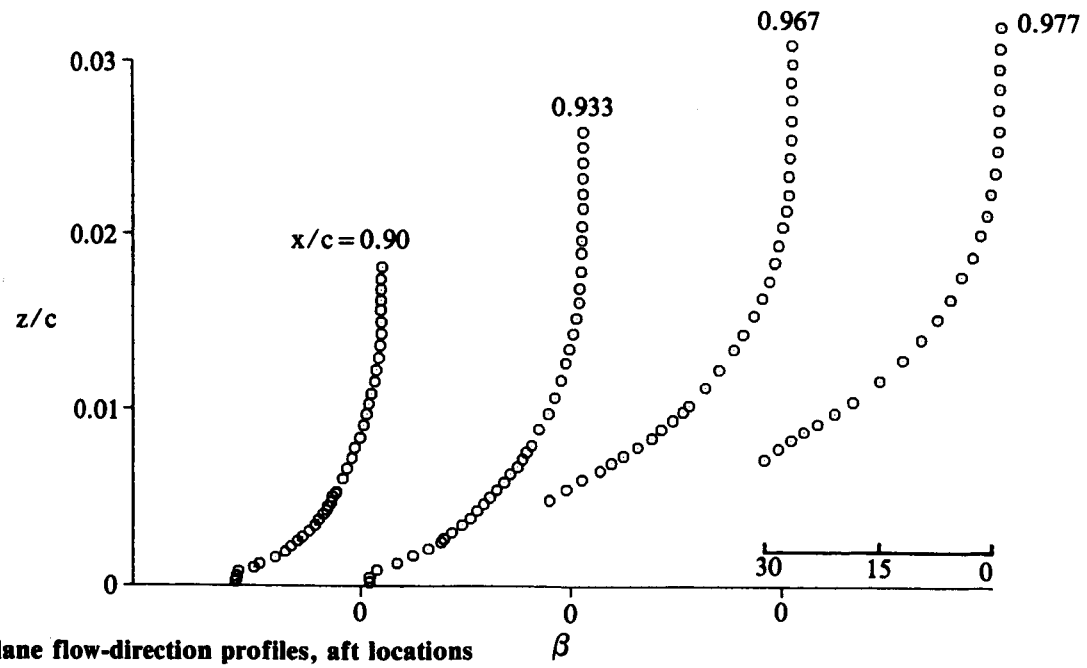

(d) Yaw-plane flow-direction profiles, aft locations

Figure 43. Boundary-layer profiles; $M_\infty = 0.70$, $\alpha = 0°$, no blowing.

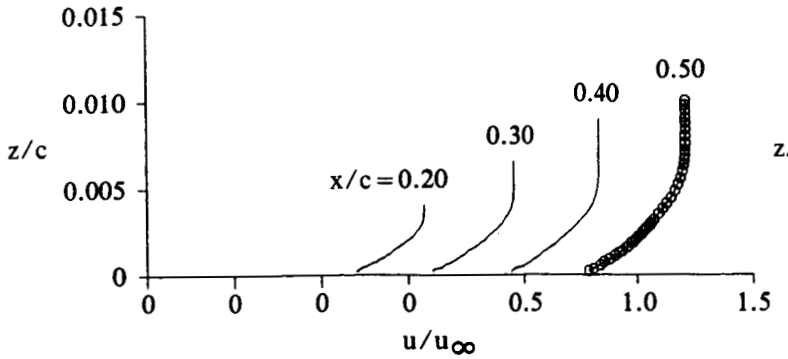

(a) Upper-surface velocity-magnitude profiles, forward locations

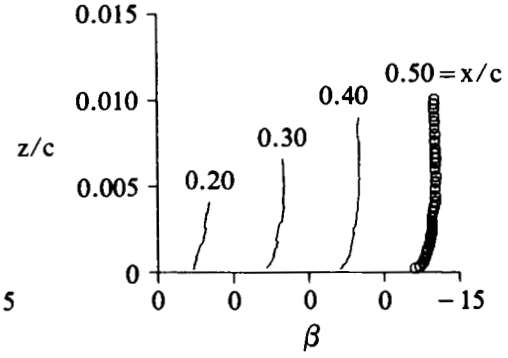

(b) Upper-surface yaw-plane flow-direction profiles, forward locations

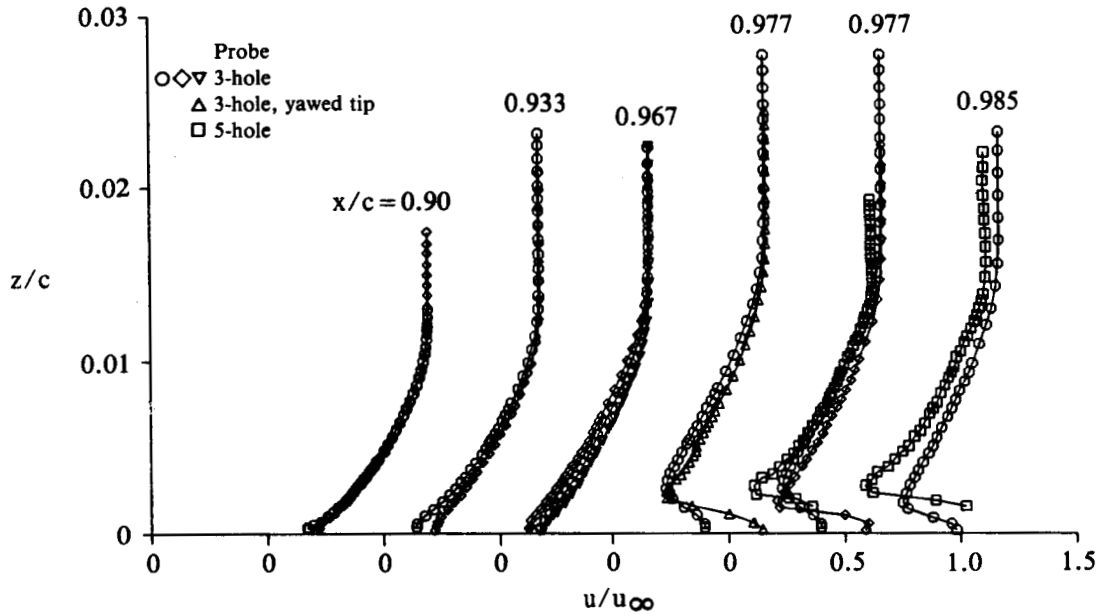

(c) Upper-surface velocity-magnitude profiles, aft locations

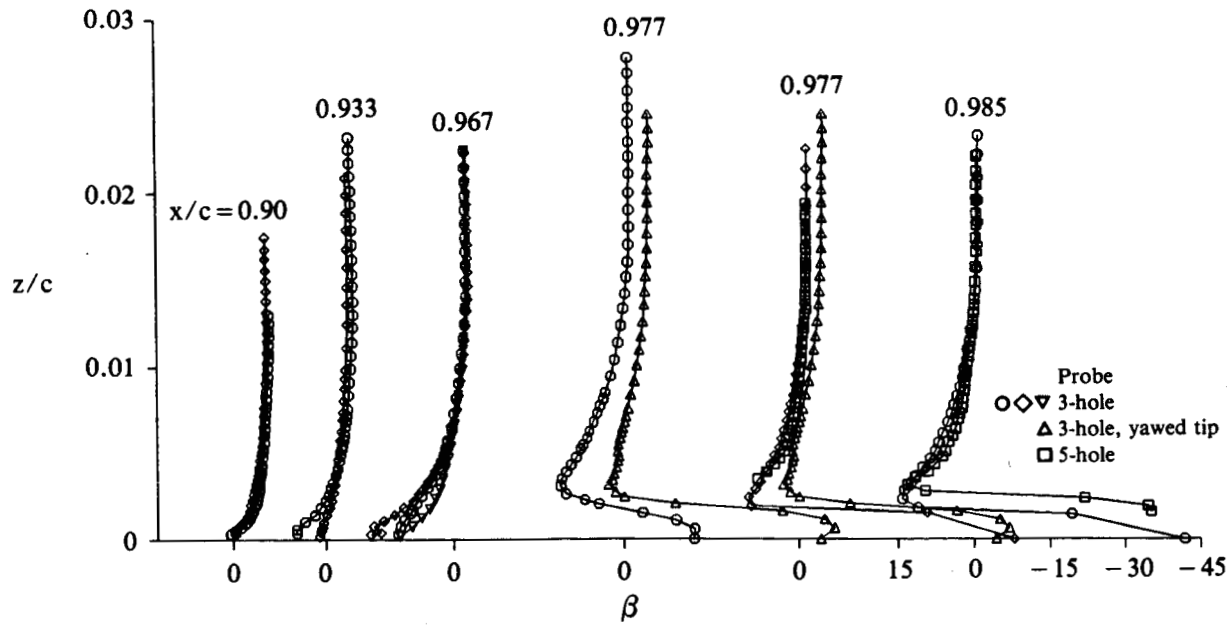

(d) Upper-surface yaw-plane flow-direction profiles, aft locations

Figure 44. Boundary-layer and wake profiles; $M_\infty = 0.70$, $\alpha = 0°$, $p_j/p_\infty = 1.4$.

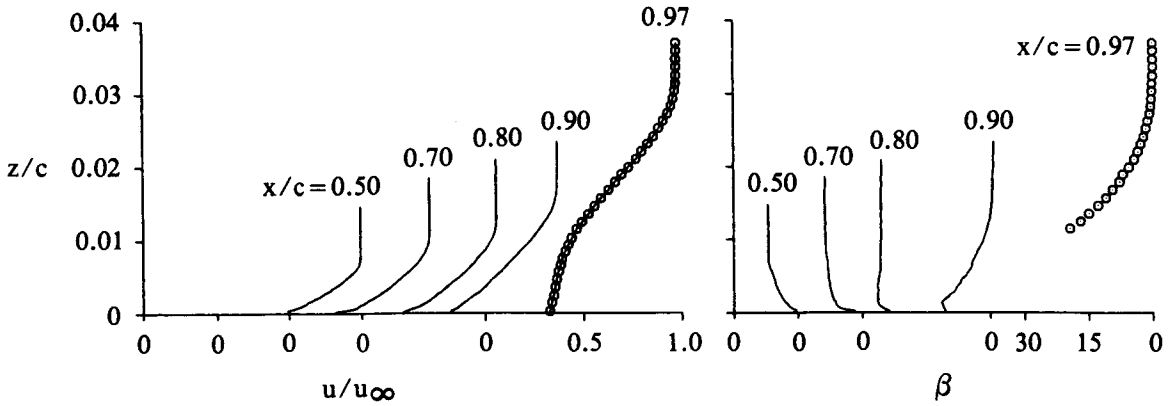

(e) Lower-surface velocity-magnitude profiles

(f) Lower-surface yaw-plane flow-direction profiles

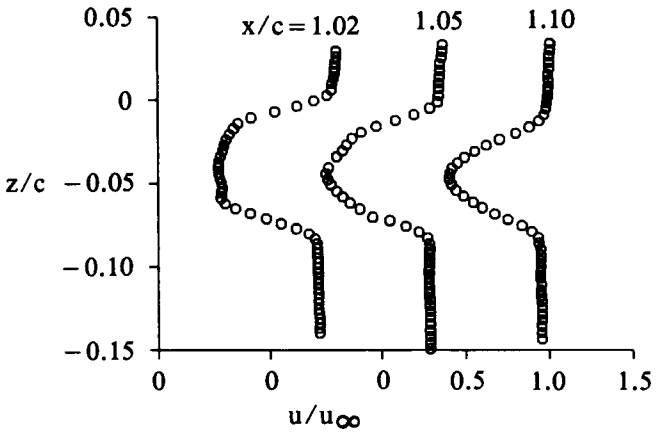

(g) Wake velocity-magnitude profiles

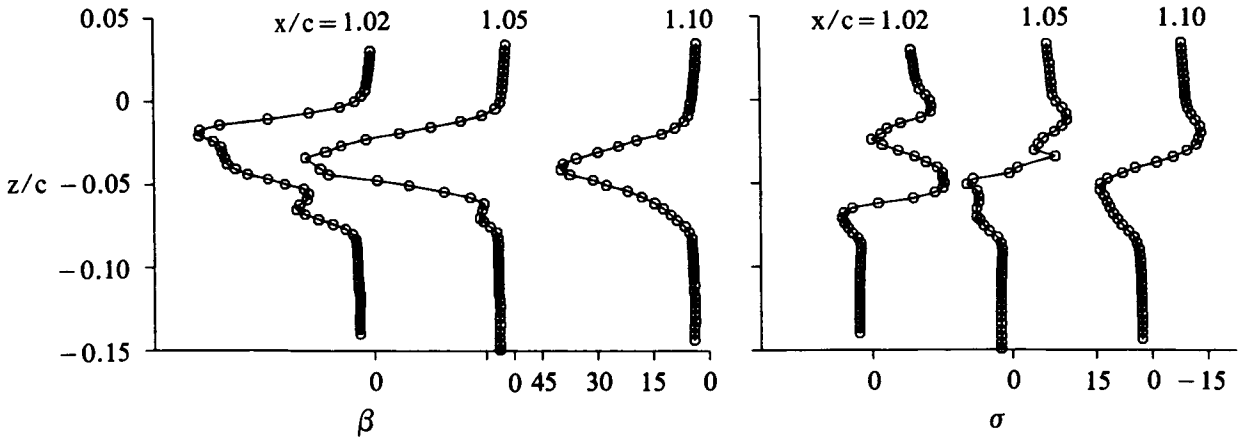

(h) Wake yaw-plane flow-direction profiles

(i) Wake pitch-plane flow-direction profiles

Figure 44. (Cont.) Boundary-layer and wake profiles; $M_\infty = 0.70$, $\alpha = 0°$, $p_j/p_\infty = 1.4$.

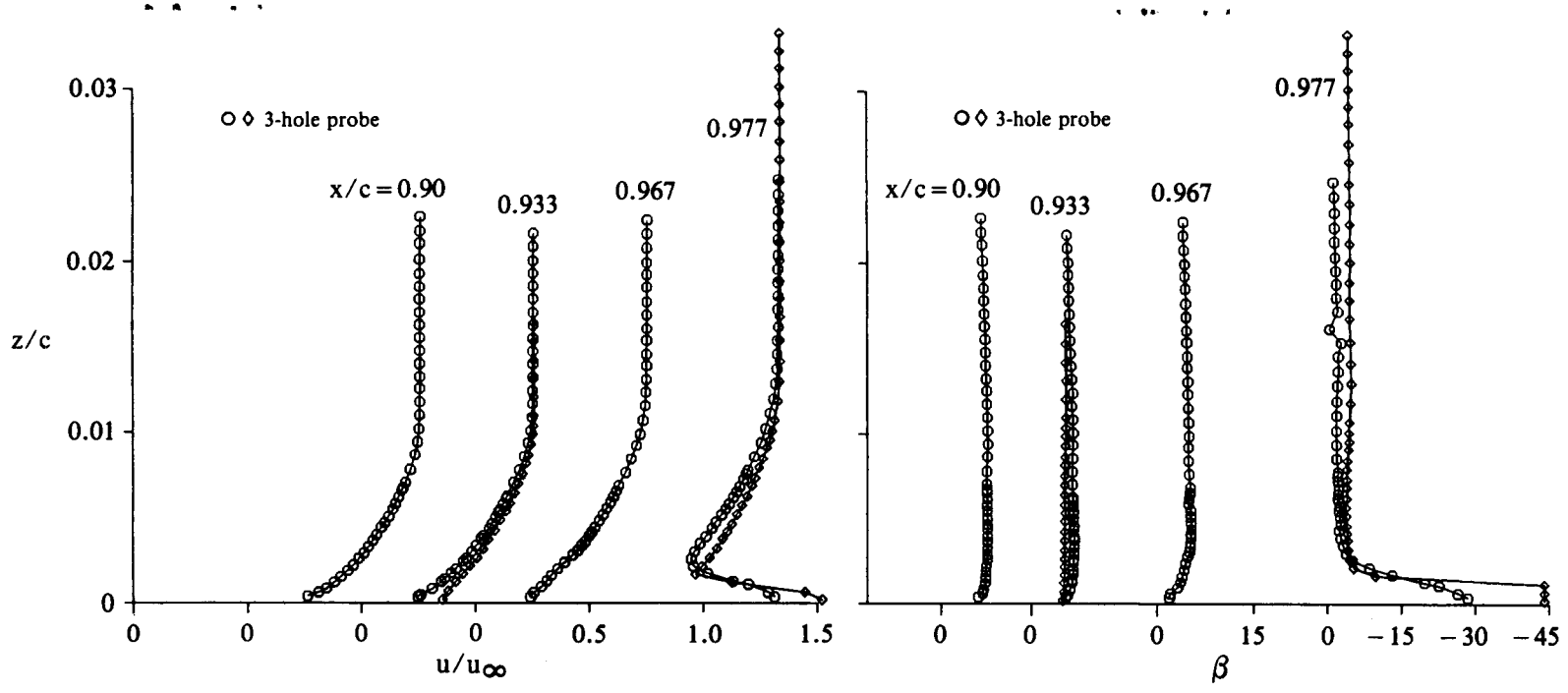

(a) Upper-surface velocity-magnitude profiles

(b) Upper-surface yaw-plane flow-direction profiles

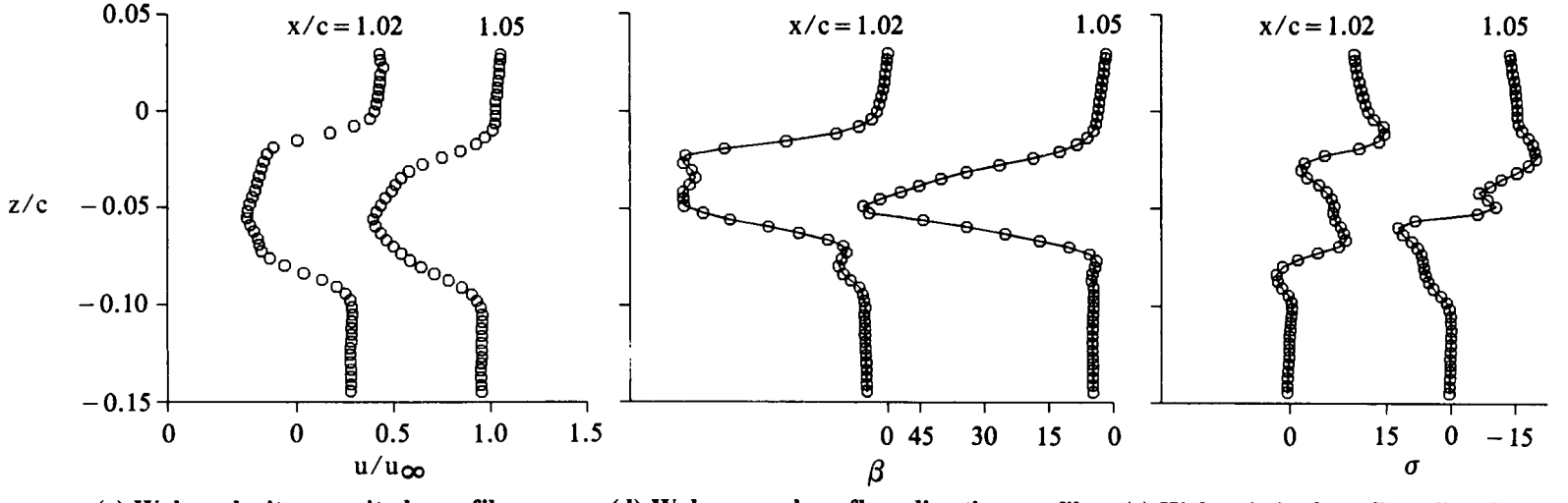

(c) Wake velocity-magnitude profiles

(d) Wake yaw-plane flow-direction profiles

(e) Wake pitch-plane flow-direction profiles

Figure 45. Boundary-layer and wake profiles; $M_\infty = 0.70$, $\alpha = 0°$, $p_j/p_\infty = 1.8$.

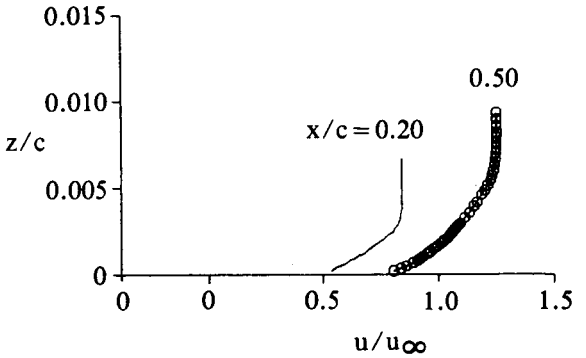

(a) Upper-surface velocity-magnitude profiles, forward locations

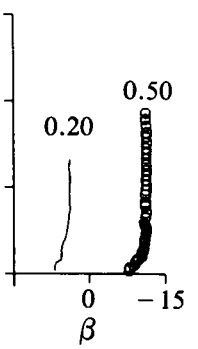

(b) Upper-surface yaw-plane flow-direction profiles, forward locations

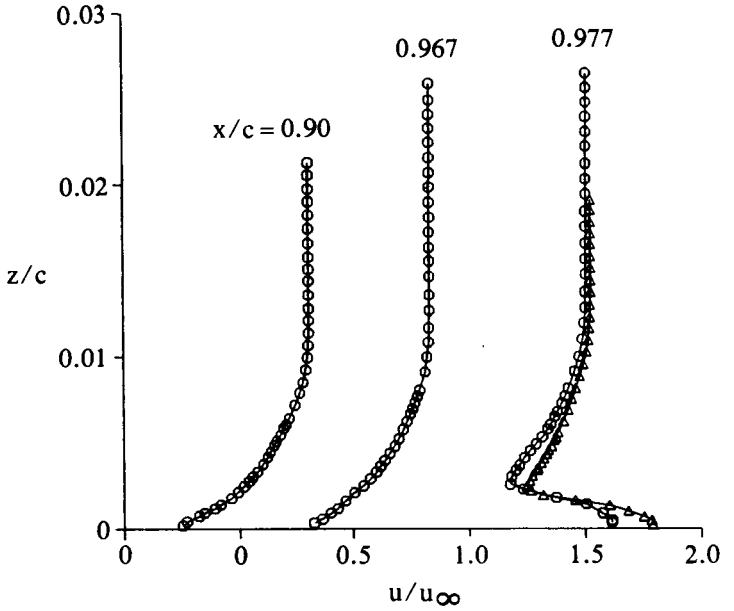

(c) Upper-surface velocity-magnitude profiles, aft locations

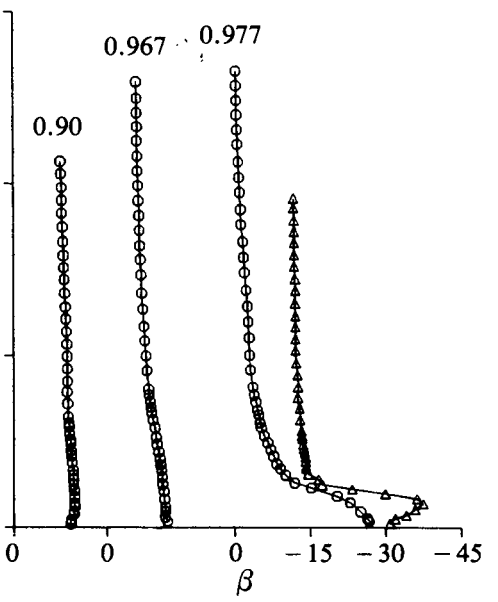

(d) Upper-surface velocity-magnitude profiles, aft locations

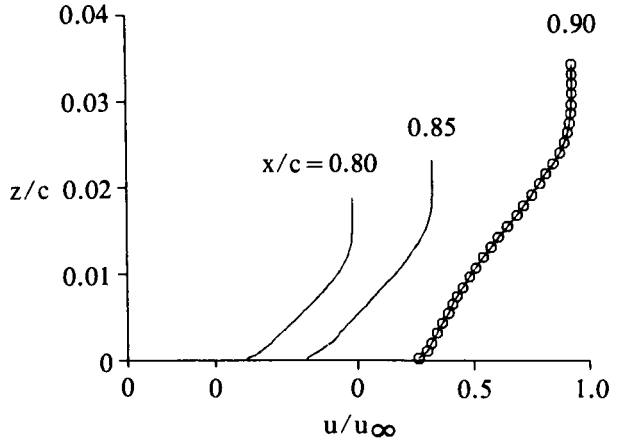

(e) Lower-surface velocity-magnitude profiles

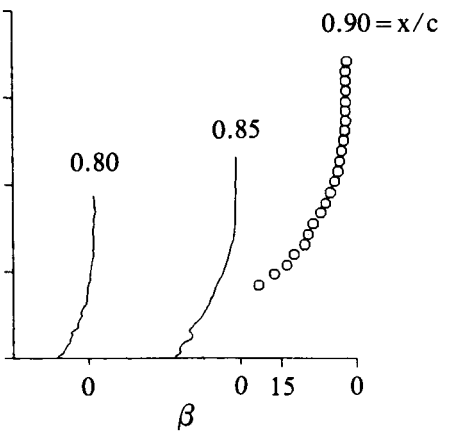

(f) Lower-surface yaw-plane flow-direction profiles

Figure 46. Boundary-layer profiles; $M_\infty = 0.70$, $\alpha = 0°$, $p_j / p_\infty = 2.2$.

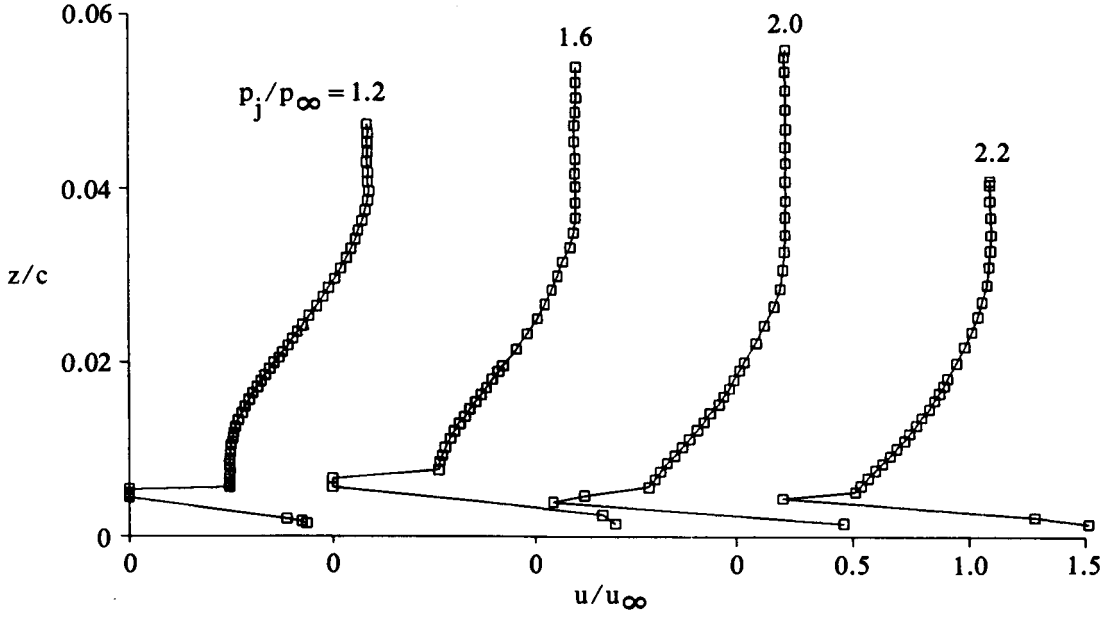

(a) Velocity magnitude profiles

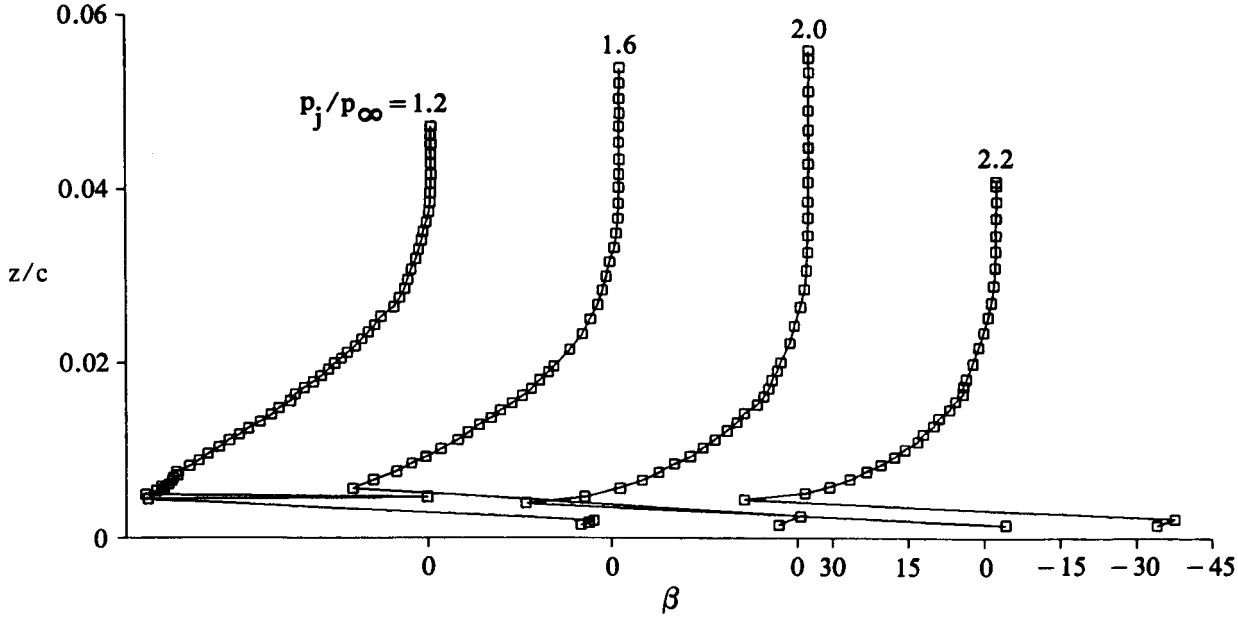

(b) Yaw-plane flow-direction profiles

Figure 47. Wall-jet profiles; $M_\infty = 0.70$, $\alpha = 5°$, $x/c = 0.977$.

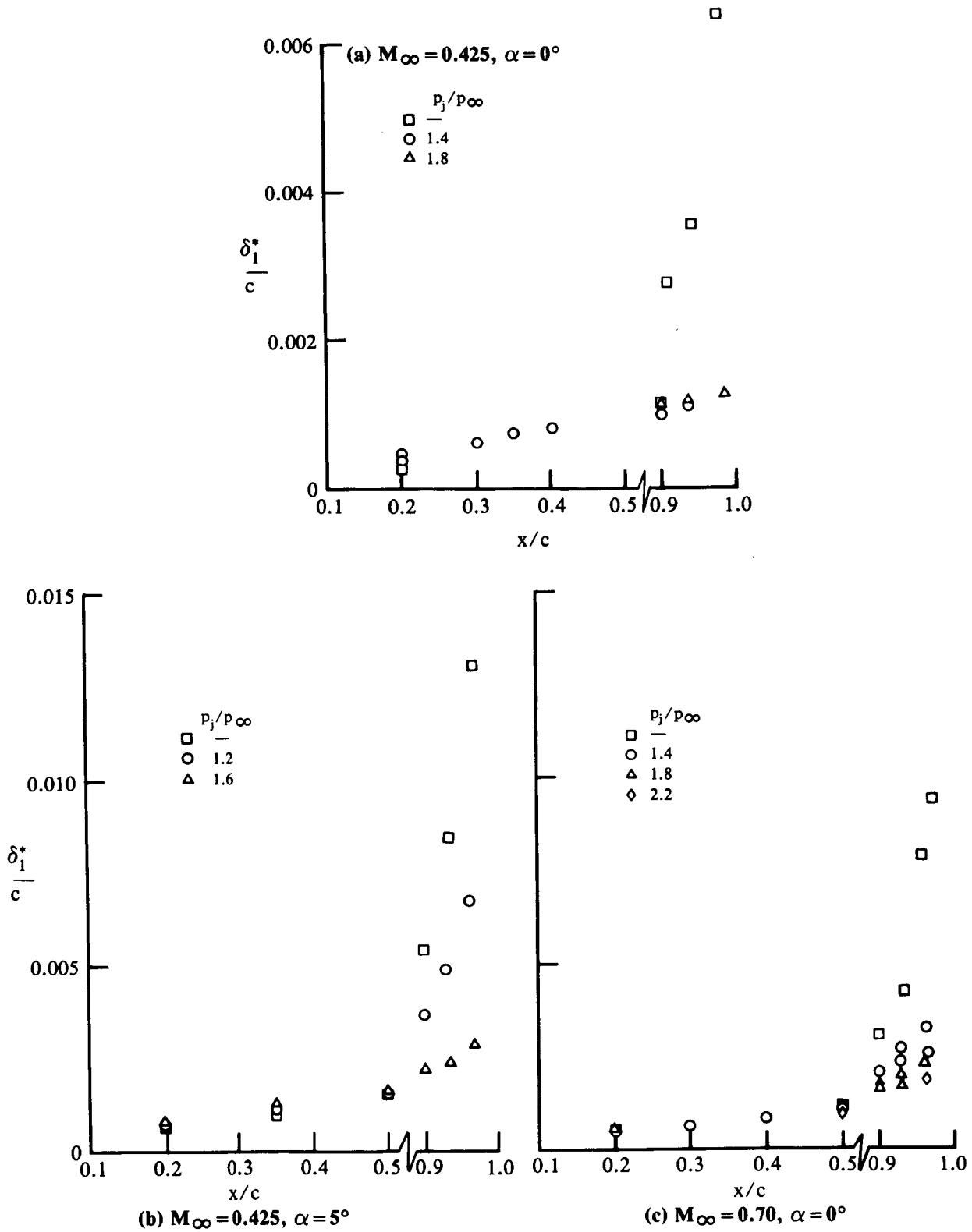

Figure 48. Upper-surface streamwise displacement-thickness distributions.

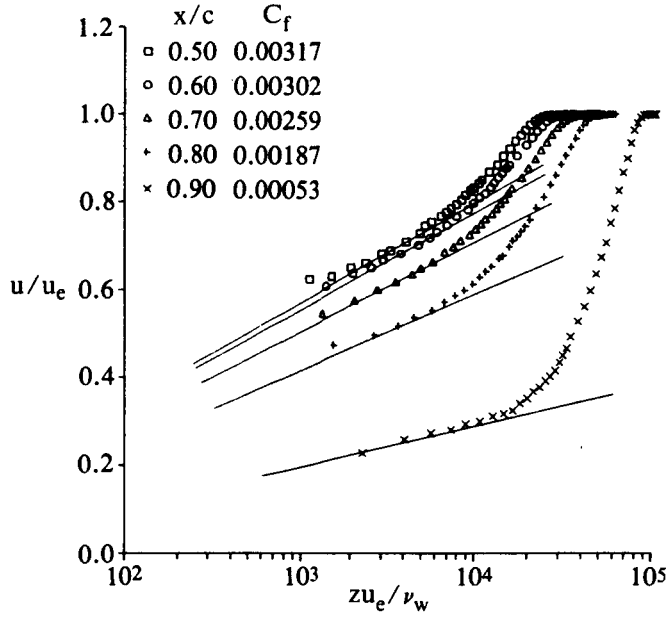

Figure 49. Lower-surface velocity magnitude profiles in semi-log coordinates; $M_\infty = 0.425$, $\alpha = 0°$, $p_j/p_\infty = 1.4$.

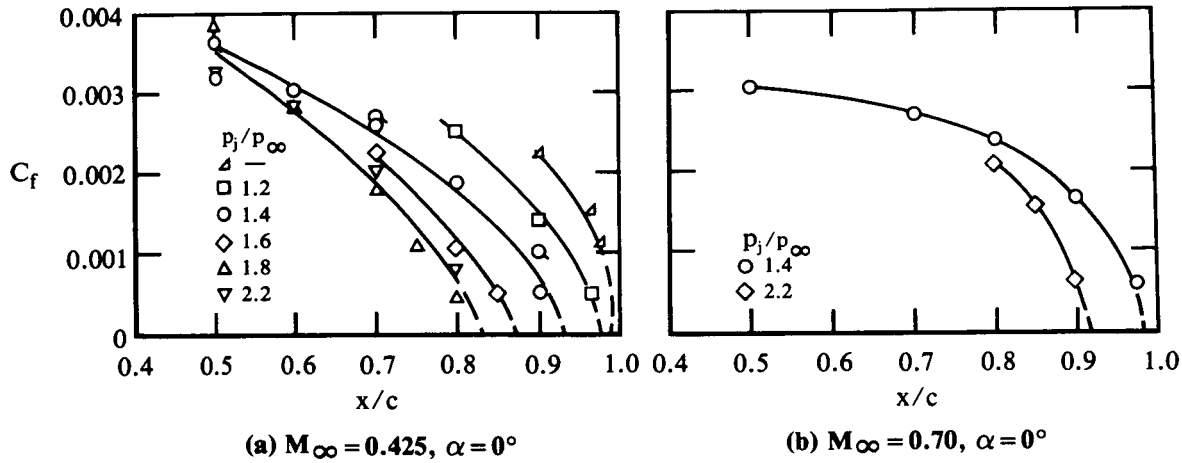

(a) $M_\infty = 0.425$, $\alpha = 0°$ **(b) $M_\infty = 0.70$, $\alpha = 0°$**

Figure 50. Lower-surface skin-friction distributions.

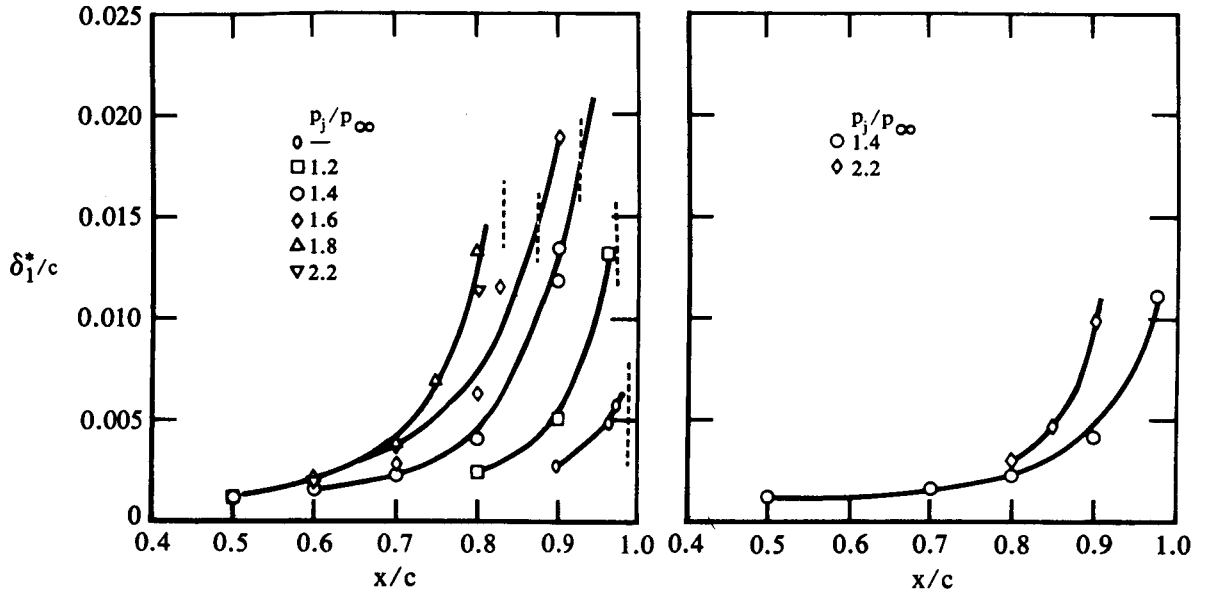

(a) $M_\infty = 0.425$, $\alpha = 0°$ **(b) $M_\infty = 0.70$, $\alpha = 0°$**

Figure 51. Lower-surface streamwise displacement-thickness distributions.

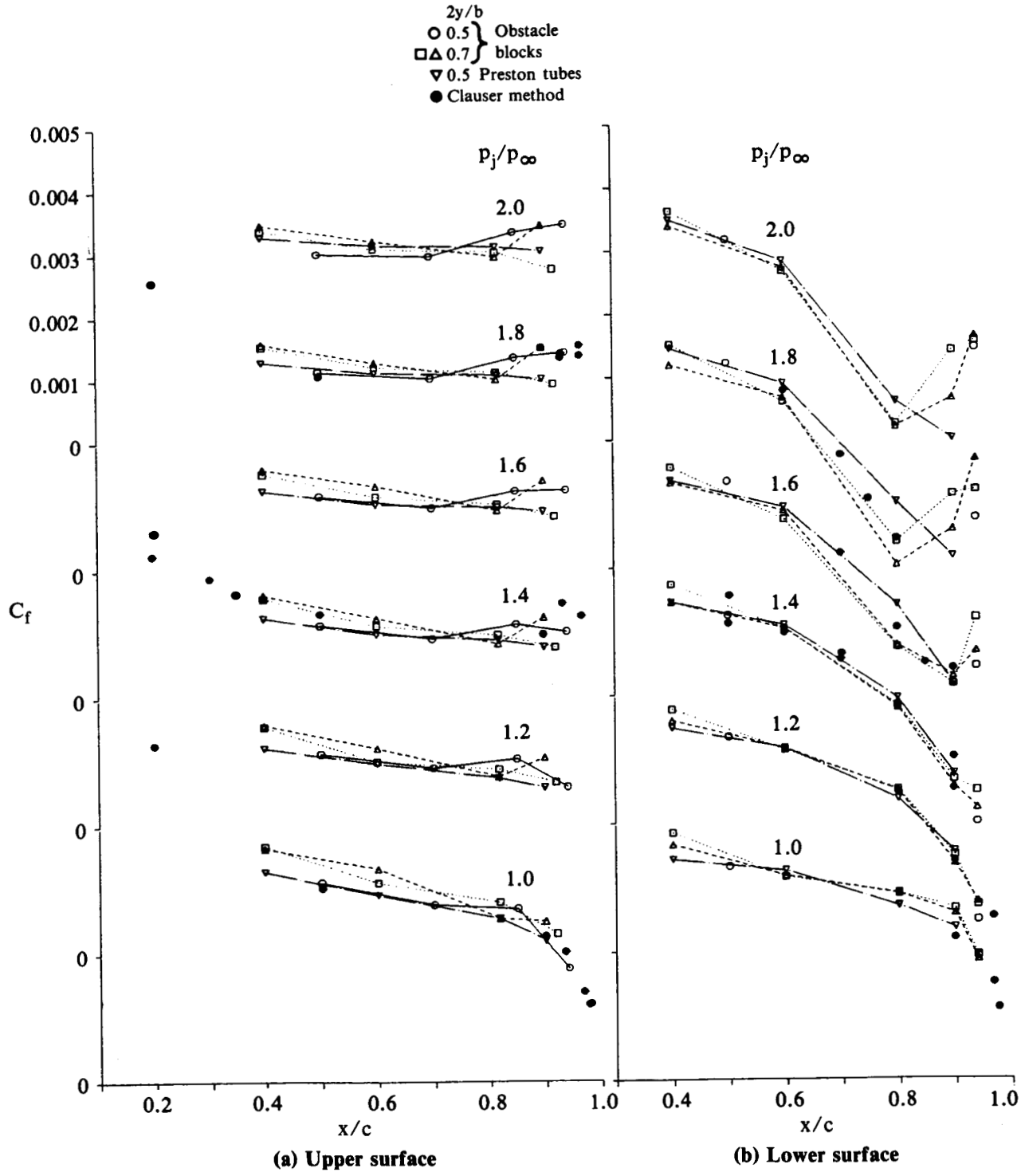

Figure 52. Skin friction distributions; $M_\infty = 0.425$, $\alpha = 0°$, lower blowing rates.

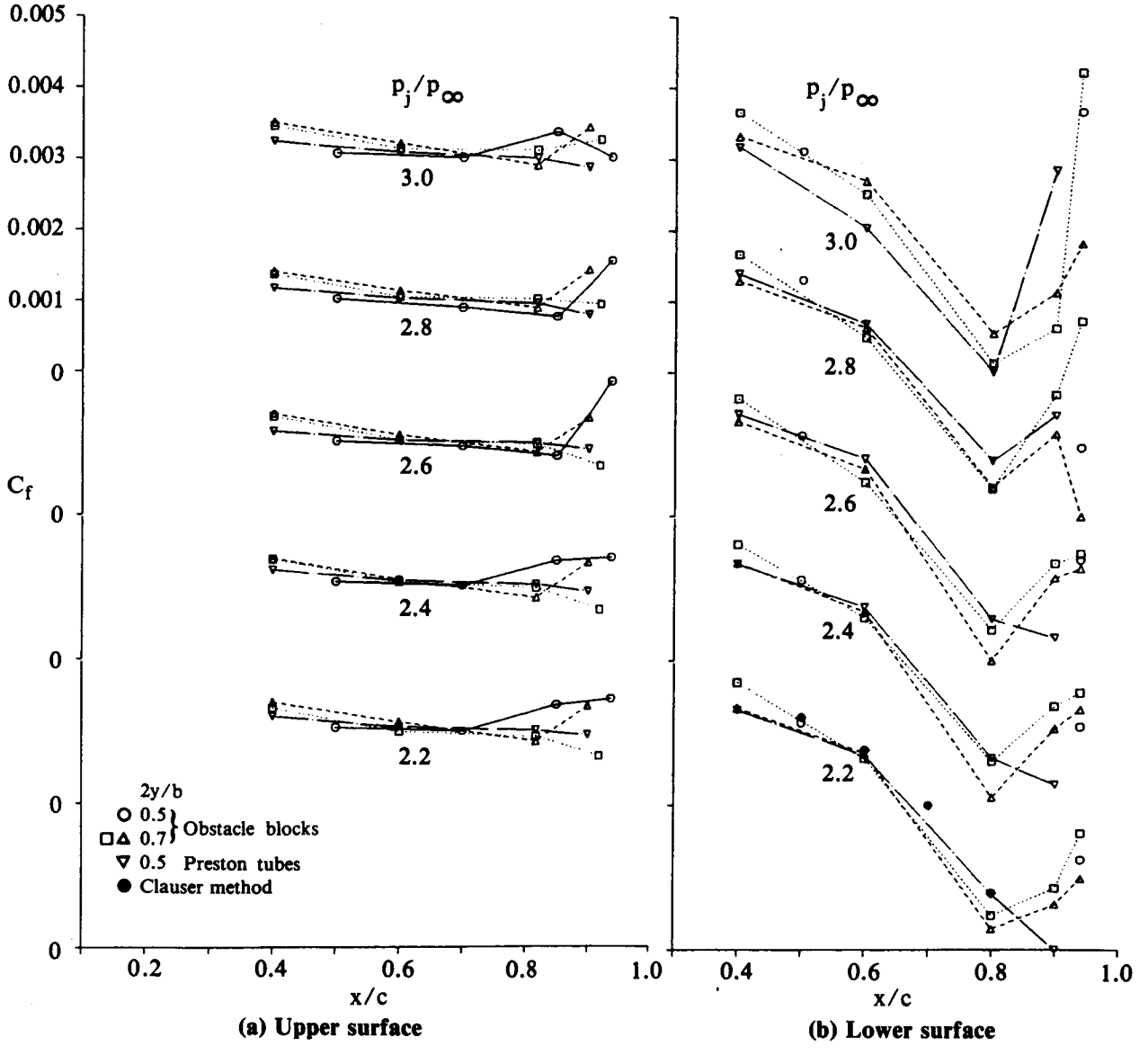

Figure 53. Skin friction distributions; $M_\infty = 0.425$, $\alpha = 0°$, higher blowing rates.

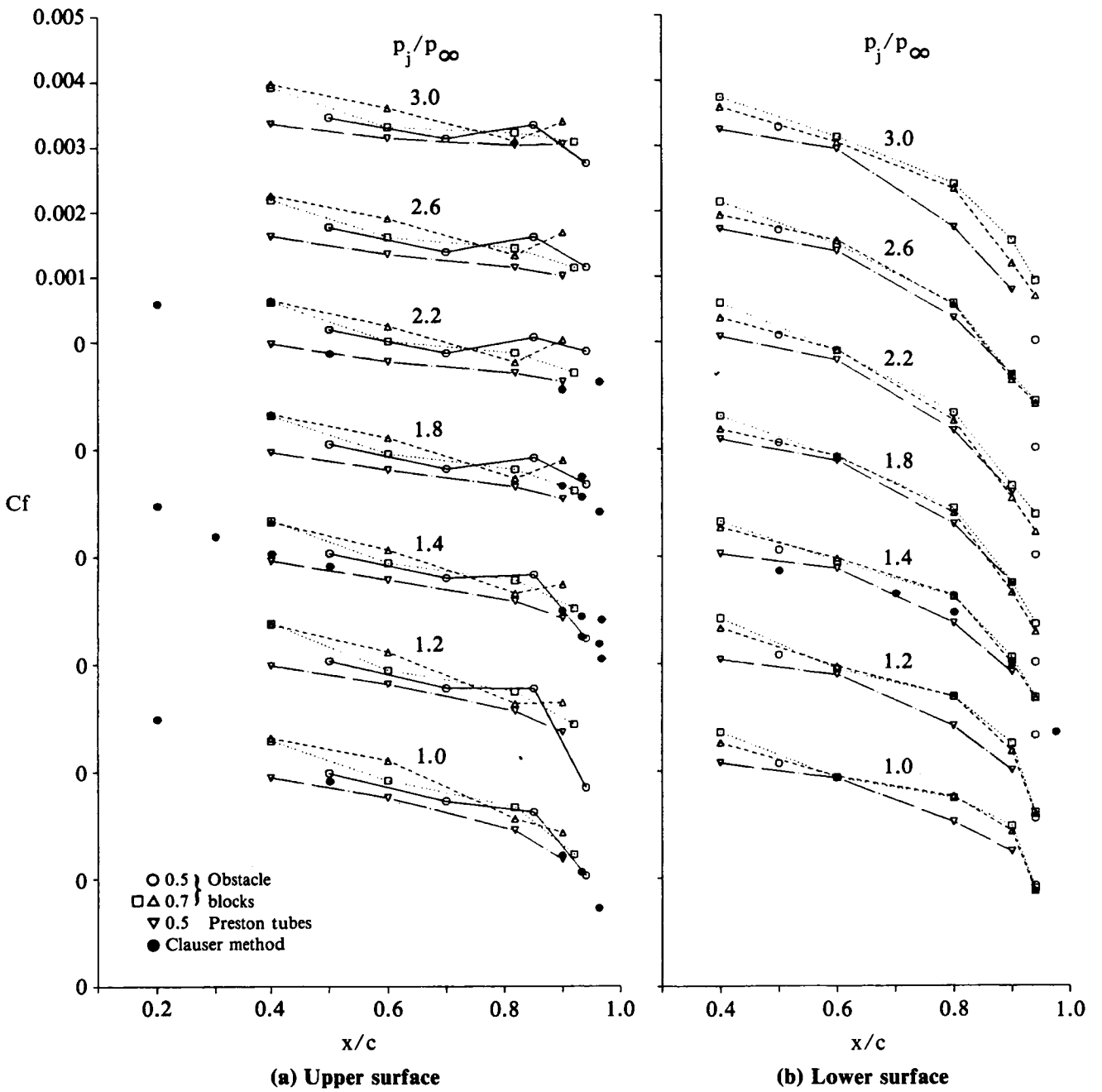

Figure 54. Skin friction distributions; $M_\infty = 0.70$, $\alpha = 0°$.

Table 1. Uncertainty estimates in probe-pressure measurements.

Uncertainties in test-section probe-pressure measurements

Source of uncertainty	Uncertainty estimate (kPa)
p_r	0.048
p_c	0.048
e_m	0.10
e_0	0.069
e_c	0.069
Transducer cal.	0.069
RSS combination	0.17

Uncertainties in probe calibration data scaled to tunnel conditions (kPa)

M_∞ (tunnel)	M_{cal}		
	0.25	**0.70**	**1.0**
0.425	0.11	0.046	0.027
0.70	0.09	0.10	0.060

Table 2. Probe calibration parameters.

Name	Normal form	Modified form*
Yaw-plane pressure difference, three-hole probe	$\frac{p_L - p_R}{p_C - \frac{1}{2}(p_L + p_R)}$	$\frac{p_C - p_R}{p_C - p_S}$
Stagnation pressure correction, three-hole probe	$\frac{p_T - p_C}{p_C - \frac{1}{2}(p_L + p_R)}$	$\frac{p_T - p_C}{p_C - p_S}$
Yaw-plane pressure difference, five-hole probe	$\frac{p_L - p_R}{p_C - \frac{1}{4}(p_L + p_R + p_U + p_D)}$	$\frac{p_L - p_C}{p_C - \frac{1}{2}(p_U + p_D)}$
Pitch-plane pressure difference, five-hole probe	$\frac{p_U - p_D}{p_C - \frac{1}{4}(p_L + p_R + p_U + p_D)}$	$\frac{p_U - p_D}{p_C - \frac{1}{2}(p_U + p_D)}$
Stagnation pressure correction, five-hole probe	$\frac{p_T - p_C}{p_C - \frac{1}{4}(p_L + p_R + p_U + p_D)}$	$\frac{p_T - p_C}{p_C - \frac{1}{2}(p_U + p_D)}$
Static pressure correction, five-hole probe	$\frac{\frac{1}{4}(p_L + p_R + p_U + p_D) - p_S}{p_C - \frac{1}{4}(p_L + p_R + p_U + p_D)}$	$\frac{\frac{1}{2}(p_U + p_D) - p_S}{p_C - \frac{1}{2}(p_U + p_D)}$

Subscripts

T stagnation
S static
L left port
C center port } viewed from above
R right port
U upper port
D lower port

* Version used for three-hole probe with left port data not used, for five-hole probe with right port data not used.

NASA National Aeronautics and Space Administration

Report Documentation Page

1. Report No.	2. Government Accession No.	3. Recipient's Catalog No.
NASA TM-89426		

4. Title and Subtitle
Boundary-Layer and Wake Measurements on a Swept, Circulation-Control Wing

5. Report Date
December 1987

6. Performing Organization Code

7. Author(s)
Frank W. Spaid (McDonnell Douglas Research Labs, St. Louis, Missouri) and Earl R. Keener

8. Performing Organization Report No.
A-87098

10. Work Unit No.
505-61-51

9. Performing Organization Name and Address
Ames Research Center
Moffett Field, CA 94035

11. Contract or Grant No.

13. Type of Report and Period Covered
Technical Memorandum

12. Sponsoring Agency Name and Address
National Aeronautics and Space Administration
Washington, DC 20546-0001

14. Sponsoring Agency Code

15. Supplementary Notes
Point of Contact: Fluid Dynamics Research Branch, Ames Research Center, MS 260-1, Moffett Field, CA 94035, (415) 694-4135 or FTS 464-4135

16. Abstract
Wind-tunnel measurements of boundary-layer and wake velocity profiles, surface static-pressure distributions, and oil-flow photographs are presented for a swept, circulation-control wing. The model is an aspect-ratio-four semispan wing mounted on the tunnel side wall at a sweep angle of 45°. The 25.4-cm constant-chord airfoil is a 20% ellipse, modified with circular leading and trailing edges of 4% radius. This configuration does not represent a specific shape obtained from current vehicle design concepts, which are being developed. A full-span, tangential, rearward-blowing, circulation-control slot is located ahead of the trailing edge on the upper surface. Flow surveys were obtained at mid-semispan at free-stream Mach numbers of 0.425 and 0.70, Reynolds numbers of 2.3×10^6 and 3.2×10^6, based on streamwise chord, angles of attack of 0° and 5°, and jet stagnation to free-stream static-pressure ratios of 1.0 to 2.2.

17. Key Words (Suggested by Author(s))	18. Distribution Statement
Boundary layer, Wind tunnel Wake velocity Pressure distribution Circulation-control wing	Unclassified-Unlimited Subject Category - 02

19. Security Classif. (of this report)	20. Security Classif. (of this page)	21. No. of pages	22. Price
Unclassified	Unclassified	92	A05

NASA FORM 1626 OCT 86

For sale by the National Technical Information Service, Springfield, Virginia 22161